A Thesis for the Degree of Ph.D. in Engineering

Three-Dimensional Morphology Analysis of Vertebral Trabecular Network Architecture Using Multi-Scale Method

September 2013

Graduate School of Science and Technology
Keio University

Khairul Salleh Bin Basaruddin

DISSERTATION

Submitted to the School of Science for Open and Environmental Systems, Keio University, in partial fulfillment of the requirements for the degree of Doctor of Philosophy

For my parents who taught me to work hard and dream big,

and

for my wife, Norhayati Nor Hakimi who made all of this possible through her love, encouragement and sacrifices

Abstract

Assessment of bone quality is essential for determining the fracture risk of osteoporotic bone. Bone quality refers to properties that influence bones' ability to resist fracture but are not explained by bone density. The morphology of a trabecular network plays a key role in determining bone quality. Morphology characteristics are commonly described by morphometric parameters (e.g. mean trabecular thickness, mean trabecular spacing, trabecular number per unit length, etc.) and their correlation with apparent mechanical properties. However, morphometric parameters are described only in terms of the size and quantity of the individual trabecular and are dependent on bone density.

A novel approach to characterizing the morphology of a trabecular network from a truly microarchitectural viewpoint has been developed by examining apparent mechanical properties, microscopic stress distribution, and principal stress vectors based on a multi-scale method. Apparent elastic moduli were quantified to explain the anisotropy of healthy and osteoporotic bones related to their morphological characteristics. A classification method was introduced to investigate the morphology of the trabecular structure, focusing on load-bearing capability. This method was developed by analyzing the response of microscopic stress distribution with respect to orthogonal macroscopic and static loads. The principal stress vector was also used to describe the mechanical role of trabecular microarchitecture. Next, a dynamic-explicit finite element method was used to visualize the percolation of load transfer in the trabecular network. This approach provided a new insight into the investigation of trabecular network morphology.

A new probabilistic simulation model based on a stochastic image-based multi-scale method was then developed to ensure the reliability of the calculated apparent elastic properties, which was used to examine the morphology of trabecular bone. Uncertainties that arise from bone characteristics, experimental works and image-processing were mod-

eled in a systematic manner. Fluctuations in the uncertainty parameters were assumed in normal distribution, and effective properties were obtained using a Gaussian mixture method. Good agreement between the predicted stochastic apparent elastic moduli and the experimental findings of many researchers substantiated the reliability of the present morphology analysis. The developed probabilistic model could be used potentially as an extrapolation technique from a calibrated case to another case without measured data, and it may also be applicable to a variety of heterogeneous engineering materials, especially in microstructure design.

Acknowledgements

In the name of Allah, the Most Gracious and the Most Merciful

I praise and thank to Allah Almighty for making it possible for me to come here at Keio University, Japan three years ago for granting me the good fortune to work on a research problem that I enjoyed and for seeing me through the ups and downs that every Ph.D engenders.

The present work would not have been possible without the help of several persons, to whom I am eternally indebted. First of all, I would like to thank my advisor, Prof. Naoki Takano, for teaching me so much over the past three years and for inspiring me through the examples of his hard work and intensity. The countless stimulating and very interesting discussions shaped my thoughts and founded the basis of the present work. I am very glad to have had such a generous doctoral advisor.

I want to express my deepest gratitude to the committee members, Prof. Kazuyuki Shizawa, Assoc. Prof. Naomichi Ogihara and Assoc. Prof. Kenji Oguni, for their constructive criticism and advice during the defense and private discussions that helped to improve this thesis.

I would also like to thank Prof. Takayoshi Nakano at Osaka University for sharing his past research works and collaborating with me in the present study. In addition, the dedicated help from Dr. Takuya Ishimoto and Dr. Sayaka Miyabe (both at Osaka University) in preparing the micro-CT images for this research is acknowledged with gratitude. I would like to thank Osaka City University Hospital for providing the bone specimen, which was approved for analysis by the Ethics Committee. I also wish to express my heartfelt thanks to the donors family for their generosity in the face of their bereavement.

My gratitude is also extended to Dr. Keizo Ishii (President & CEO) and Dr. Makoto Tsukino (Voxelcon Project Leader) at Quint Corporation, Tokyo, for giving me the opportunity to do an internship at their company and for providing great support and help in the usage of Voxelcon software.

A great source of motivation for me throughout my time as a Ph.D candidate has also come from my circle of Ph.D colleagues—Dr. Mohammad Sofian, Dr. Mohd Rodzimin, Dr. Mohd Faizal, and Dr. Ahmad Isni—with all of whom I spent a great deal of time while in Keio University. I would also like to thank all of my colleagues in the Mechanical Simulation Laboratory (Takano Lab), including Susanto, Zumin, Yoshiwara, Ikegami, Okamoto, Ichimura, Akiyama, Omori, Nagahata, and many others. The atmosphere in our laboratory was inspirational and supportive throughout these years.

My parents have sacrificed a good many years of their lives to make my education possible. My wife, Norhayati Nor Hakimi, always supported me through her encouragement, unconditional love, and understanding during this Ph.D study. As difficult as it was for them, they always understood that the pressures of my research sometimes made it impossible for me to be with them as often as I would have liked. This dissertation is dedicated to my parents, my wife, and my beloved kids—thank you for seeing me through every step of the way, for praying for me during times of trouble, and for rejoicing with me over every little triumph.

From a financial point of view I am thankful to the Keio Global COE program for funding the travel fees for attending academic conferences and to the Keio Leading-edge Laboratory (KLL) for providing my research grant every year. Finally, financial support from the Malaysian Government under the Ministry of Higher Education (MOHE) and Universiti Malaysia Perlis towards my scholarship is gratefully acknowledged.

Contents

List of Figures

List of Tables

Chapter 1

Introduction

1.1 Motivation

The assessment of bone quality is essential in diagnosing osteoporosis, a disease in osteoporotic bone which occurs as a result of a decrease in bone strength (Homminga *et al.*, 2001). Bone quality refers to the influence of factors that affect fracturing, but it does not account for bone quantity or density (Chesnut and Rosen, 2001; Watts, 2002; Hernandez and Keaveny, 2006). Although density is an important determinant of bone strength, there is strong evidence that the morphology of trabecular bone plays a significant role in bone strength and determines its biomechanical properties (Ulrich *et al.*, 1999). Theoretical relationships between the apparent elastic properties and morphological parameters that describe the architecture of trabecular bone explain over 90% of the variations in apparent elastic properties (Turner, 1992). The morphology of a trabecular bone network has been described as a complex and disordered microstructure (Pothuaud *et al.*, 2000) which consists of three-dimensional interconnecting plates and rods. Trabecular morphol-

ogy changes in osteoporotic and ageing patients by thinning and perforating trabecular rods and plates, respectively (Homminga *et al.*, 2001).

Changes in trabecular microarchitecture also occur in healthy bone. The morphology of trabecular bone is related to its internal mechanical loads (Weinans *et al.*, 1992), and the process that regulates this relationship is known as 'bone remodeling'. Trabecular bone morphology adapts in such a way that its principal material axes are oriented along the most common loading directions (Goldstein *et al.*, 1993). The work pattern on the remodeling process, which is related to age changes (Mosekilde, 1988), differs particularly between healthy and osteoporotic bones, due to the load-bearing capability of respective trabecular networks. The capacity of the load-bearing elements of individual trabeculae determines the fragility of trabecular microarchitecture and contributes to mechanical strength (Mosekilde, 1993). Moreover, it is believed that the connectivity of inter-trabecular struts may also affect the mechanical properties of trabecular bone (Kinney and Ladd, 1998); hence, the morphological characterization of healthy and osteoporotic bones and its effect on apparent mechanical properties are still under investigation.

In the context of bone quality, the apparent mechanical properties of trabecular bone involve two main factors: (1) The morphology of trabecular structures and (2) the microscopic properties of solid bone tissue moduli (Hernandez and Keaveny, 2006). Due to the complexity of the microarchitectural structure of trabeculae and the small scale of trabecular struts, discussions on the load-bearing behavior of individual trabeculae remain unclear. The direct measurement of stress and strain on trabecular struts is very difficult technically, due to limits imposed by this small scale; however, with today's advanced tools, numerical methods can replace actual measurement and the complicated trabecular structure can be modeled realistically using a high-resolution micro-computed

tomography (CT) scanner, thus making it possible to investigate load-bearing behavior for each trabecular strut. For this analysis, morphological information from a truly local viewpoint must be included in order to study the mechanical functions of an individual trabecular. Note that, together with local analysis, the importance of global network analysis, i.e. mechanical percolation, is highlighted in the present work.

The morphological characteristics of trabecular bone have been described commonly through morphometric parameters such as bone volume fraction, trabecular stiffness and spacing, the spatial arrangement of individual trabeculae, intertrabecular connectivity, and other aspects (Hildebrand and Ruegsegger, 1997; Liu *et al.*, 2008a). These parameters are correlated to mechanical properties as the effect of trabecular morphology. Although morphometric parameters can characterize microarchitecture, which is one of a number of bone quality factors, these parameters are actually dependent on bone quantity. Consequently, in order to recognize the contribution of morphology as a bone quality factor, we need to examine morphology characteristics supposedly independent of bone quantity.

On the other hand, the microscopic properties of bone tissue moduli are not constant when considering bone remodeling behavior. Other than morphological changes, mineral content (Sansalone *et al.*, 2010) and *c*-axis biological apatite (BAp) crystallite orientation (Nakano *et al.*, 2002) also fluctuate during the remodeling process. Fluctuations in the microscopic properties of bone tissue result in the dispersal of apparent trabecular bone stiffness. Furthermore, the dispersion of any apparent mechanical properties is not only due to uncertainties at the tissue level but also it can occur with regard to inconsistencies at the macroscopic level when assessing trabecular bone properties. For instance, the results obtained from many experimental works show many instances of scattered data (Carter and Hayes, 1977; Linde *et al.*, 1991; Keyak *et al.*, 1994). These results could

be the result of many uncertain factors, such as specimen preparations, machine set-up, or other unknown factors. Furthermore, since the use of high-resolution imaging is essential in order to reconstruct a realistic trabecular microarchitecture, issues may arise during image-processing. Parameters involved in image-based modeling, such as the determination of threshold values for binarization, and appropriate image resolution, are not deterministic and will be different case by case. Therefore, any uncertainties that might possibly arise in estimating the apparent mechanical properties of trabecular bone should be considered, so that reliable results can be obtained.

This study was undertaken to analyze the morphological characteristics of vertebral trabecular bone in a truly three-dimensional microarchitectural view. The morphology of trabecular networks was examined by considering apparent mechanical properties, microscopic stress distribution, and principal stress vectors based on a multi-scale method. Note that eigen vectors of stress tensor in this thesis is called principal stress vector. This approach allows the multi-scale method to be used for the first time, in order to analyze the morphology of a complicated trabecular network in three dimensions. The anisotropic behavior of healthy and osteoporotic bones is related to morphological characteristics in line with apparent elastic moduli. As part of this study, a novel classification method was introduced to improve visualization and to facilitate the characterization of the trabecular network. A dynamic explicit finite element method was then used to initiate stress wave percolation in the trabecular network. The morphology and mechanical role of individual trabeculae were analyzed by viewing the propagation of load transfer with the aid of the proposed classification method. Finally, a new probabilistic model was developed to investigate the reliability of the calculated apparent mechanical properties when describing the anisotropy of the trabecular morphology.

1.2 Organization of thesis

Figure 1.1 illustrates the hierarchical approaches used to achieve the objectives, as well as the respective chapters of the present study. This thesis is organized into seven chapters. Chapter 2 presents an overview of the background information related to the present study, in order to serve as a prelude to the topics covered in later chapters. Materials used in this study, namely micro-CT images and the reconstruction of a vertebral trabecular bone model, are presented in Chapter 3. The procedure employed to extract the region of interest (ROI) is described towards the end of Chapter 3. Chapter 4 discusses the analysis of trabecular morphology by introducing a new classification method based on homogenization theory. Correlations between the calculated apparent elastic moduli and morphology characteristics are also discussed. Chapter 5 explains the analysis of trabecular morphology under dynamic loading, and the approach used to describe morphology, focusing on the mechanical role of trabeculae networks by highlighting the percolation of a stress wave in load-bearing distribution, is discussed. Chapter 6 explains a new stochastic multi-scale method, in order to estimate reliable apparent mechanical properties of trabecular bone by considering fluctuations in parameters that arise due to bone characteristics, experimental works, and image-processing. A comparison between the predicted results and many experimental results is also discussed, in order to check the reliability of the calculation carried out in the morphology analysis. Findings, limitations, and future works related to the present study are described in Chapter 7. Finally, explanation about the key assumptions associated to this study is provided in Appendices A and B, and the list of publications related to the present work is available in Appendix C.

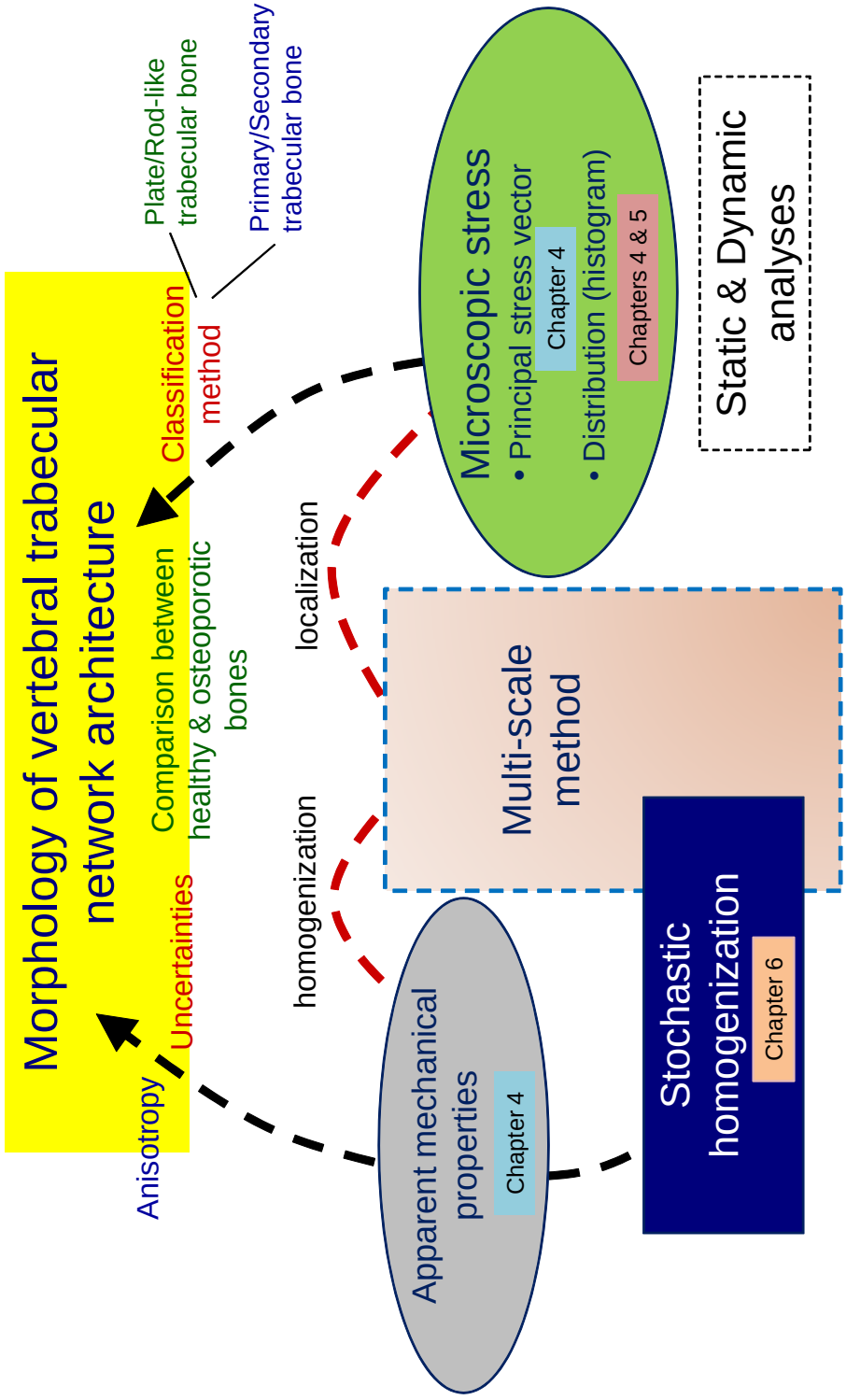

Figure 1.1: Hierarchical approach and respective chapters of the study.

Chapter 2

Background

2.1 Bone composition and structure

Bone, which is often characterized as a highly hierarchical composite because it exhibits structural organization on multiple scales (Rho *et al.*, 1998), is classified into two types: Cortical or compact bone and trabecular or cancellous bone. Cortical bone is made up of very dense, hard tissue with porosity ranging approximately between 5% and 10%. Cortical bone is found primarily in the shaft of long bones and the outer layer around trabecular bones at their proximal and distal ends (Martin and Burr, 1989). The interior of cortical bone is filled with porous (about 75% to 95%) and spongy-looking bones, named 'trabecular bones', which consist of interconnected plate and rod structures known as 'trabeculae'. In general, role of trabecular bone in human body can be classified into mechanical and non-mechanical functions. However, the present study focuses on the role of trabecular bone in terms of mechanical function only. Pore space in the interconnected trabeculae is filled with bone marrow. Lamellae are the basic building blocks of osteons

and trabeculae at the sub-microscopic level. At the ultra-structural level, a combination of mineral crystals and collagen fibrils builds the lamellae.

With regard to composition, bone tissue is described as a three-phase composite consisting of mineral biological apatite (BAp), collagen (Col) fibril, and water. Each phase contributes to the mechanical properties of the tissue. The mineral phase occupies up to 60% of the mass and about 40% of the bone volume, and it is composed mainly of calcium and phosphate with a small fraction of carbonates (Robinson and Elliott, 1957). Approximately 90% of the organic component in bone is type-I collagen and the remainder consists of non-collagenous proteins (Robinson and Elliott, 1957). Although the BAp mineral and Col fibril phases are reviewed separately, they cannot be treated independently, especially in the context of mechanical bone strength. A combination of BAp crystals and orientation Col fibrils contributes to anisotropy in the mechanical properties of bone tissues, such as Young's modulus, hardness, strength, and toughness (Sasaki *et al.*, 1989). The ductility of bone tissue is obtained by flexible collagen fibers, while the *c*-axis of BAp crystallite is distributed along extending Col fibrils in mature hard tissues, except for enamel, as illustrated in Fig. 2.1 (Nakano *et al.*, 2002). According to collagen-based mineralization, BAp crystals are associated preferentially with contiguous gaps in the collagen network. The long axis of the plate-like crystal (*c*-axis BAp crystallite) aligns with the long axis of the Col fibril (Landis *et al.*, 1996).

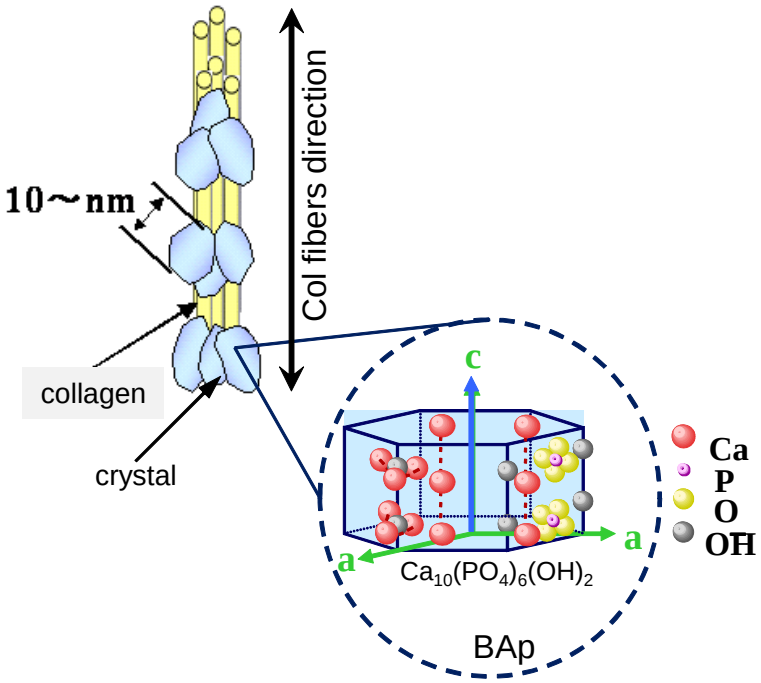

Figure 2.1: Crystal structure of biological apatite (BAp) and the orientation relationship of the *c*-axis in the direction of collagen fibrils.

2.2 Experimental works on biological apatite (BAp) crystallite

The preferential alignment of the *c*-axis of BAp crystallite in calcified tissue has been evaluated mainly by using the wide-angle X-ray diffraction technique, which includes three-dimensional pole figure analysis (Chen and Gundjian, 1974; Sasaki *et al.*, 1989; Nakano *et al.*, 2002). The main orientation of *c*-axis BAp crystallite aligns primarily with the longitudinal axis of a long bone (principal direction), whereas weak poles for the *c*-axes of BAp have been noted in lateral direction. This factor also applies to single trabeculae, where the *c*-axes orientation of BAp is scattered in normal distribution and is aligned mainly with the principal trabecular's direction (Miyabe *et al.*, 2007).

It is known that the direction of collagen fibers is parallel to the main loading direction, not only in long bones but also in mandibles. Recently, Nakano *et al.* (2002) found, through X-ray diffraction measurement, that the *c*-axis direction of BAp is also parallel to collagen fibers and the main loading direction. In their experiment using the long bone of a rabbit (ulna), during the regeneration of bone, the *c*-axis direction was random at the initial stage when the bone mass was recovered. At this stage, the load was not transferred until the bone mass was perfectly recovered. After that, the bone mass was almost constant, whilst the *c*-axis orientation was aligned to the loading direction. Nakano et al.'s experiment suggested that the *c*-axis is preferentially aligned to the main loading direction. It is reasonable to have higher stiffness in the main loading direction. The stiffness was also measured quite recently by nano-indentation.

Note that consensus has not yet been reached to support this theory, but it is believed that the bone is regenerated to support the load optimally. Supposing that a long bone, bending stiffness, EI, is important, we can understand the above experimental result in the following way. At the initial stage, E is not high enough because of random *c*-axis directions, so the bone mass increases to achieve high I. In another experimental result posited by Takano et al. using the mandible from a beagle dog, a decrease in bone mass was observed after a few months.

2.3 Bone remodeling

Bone remodeling is the process whereby old bone tissue is replaced continually with new bone tissue through osteoclasts and osteoblasts. Remodeling, which takes approximately six to nine months to complete, occurs gradually (Frost, 1989). The mechanism involved

in bone remodeling has been described through Wolff's Law for over 100 years. It was hypothesized that a relationship exists between bone microarchitecture and loading conditions. In the growth and adaptation of bone, the trabecular morphology changes and is adapted to external loading direction and magnitude. The overall orientation of trabecular bone is not random but aligned primarily with the principal mechanical loading direction (Turner, 1992). It is believed that the loading is sensed by the bone, and the bone structure is then adapted accordingly. Osteocytes in the bone matrix are able to sense strain, possibly through stretch-activated ion channels, interstitial fluid flow, or electric potentials (Weinans *et al.*, 1992; Turner, 1998).

Osteoblasts are responsible for bone formation or reproducing new bones, while osteoclasts work for bone resorption or breaking down the bone tissue. Figure 2.2 is an illustration of balancing activities between osteoblasts and osteoclasts for healthy and osteoporotic bones. In healthy bone, the balance between an osteoclast and an osteoblast provides the dynamic of bone tissue so that the microarchitecture is constantly reshaped as a response to external loading. However, for osteoporotic bone, the number of osteoblasts tends to decrease, which then unbalances the formation and resorption of bone tissue. In vertebrae, this leads to a decrease in bone density and to the resorption of horizontal trabeculae caused by osteoclasts activity, because the priority of the structure is to support the main load, which is in a vertical direction. This action results in structural changes in the form of longer and thinner trabecular rods.

Furthermore, the distribution of minerals over trabeculae is also affected by the rate of bone remodeling, which is higher in the surface layer than in the middle of an individual trabecular (interstitial) bone (Birkenhäger-Frenkel *et al.*, 1993). Mineralization continues slowly after the remodeling process, in which case mineral content is higher in interstitial

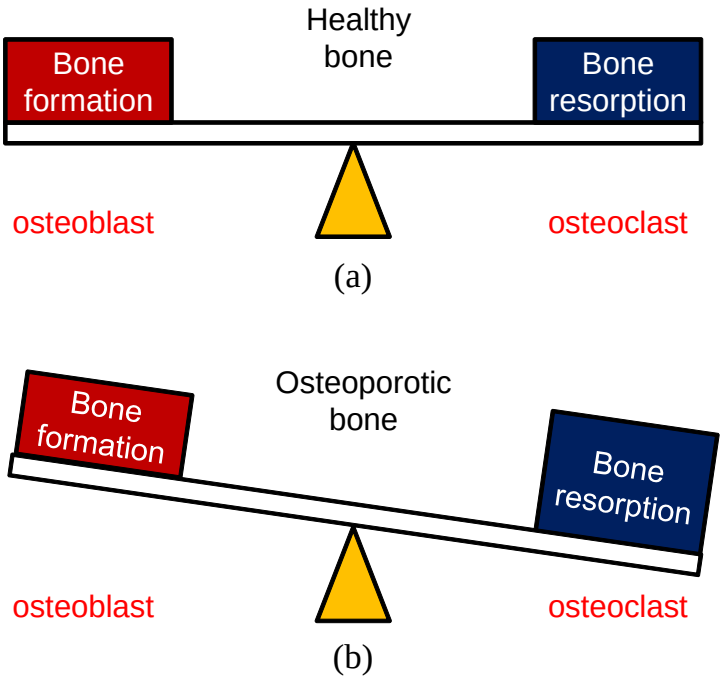

Figure 2.2: Illustration of bone formation and bone resorption activities in healthy and osteoporotic bones.

bone, compared to the surface layer (van der Linden *et al.*, 2001). The stiffness of bone tissue is related exponentially to mineral content (Currey, 1986). Hence, non-uniform mineral distribution over the cross-section of a trabecular results in different mechanical properties between the periphery and the center of the trabecular strut. The highly mineralized trabeculae core is surrounded by a surface layer that is lower in stiffness. Considering all trabecular regions, the degree of anisotropy is increased due to bone remodeling. Therefore, besides changes in the microarchitecture of trabecular networks during the remodeling process, mechanical properties are also affected by differences in mineral distribution.

2.4 Trabecular bone microarchitecture

The microarchitecture of trabecular bone can be observed through morphometric measurement (Feldkamp *et al.*, 1989). Morphometric parameters such as bone volume density (BV/TV), bone surface to bone volume ratio (BS/BV), mean trabecular thickness (Tb.Th), mean trabecular spacing (Tb.Sp.), and trabecular number per unit length (Tb.N) are commonly used to characterize trabecular bone microarchitecture (Hildebrand and Ruegsegger, 1997). BV/TV is bone volume over the total volume of interest. BS/BV characterizes the rate of bone turnover, because bone resorption and formation can only occur on bone surfaces. The marrow space between trabeculae is measured through Tb.Sp. Moreover, the microarchitecture of trabecular bone is also characterized at the local level by measuring the quantity, orientation, and geometry of individual trabeculae plates and rods (Shi *et al.*, 2010). Trabecular bone microarchitecture can vary greatly according to differences in anatomic sites, age and between individuals. Moreover, microarchitecture also varies in different regions at the same anatomic site. For instance, comparing the upper, mid, and lower regions in lumbar vertebrae, plate-like bones are significantly higher in the mid region than in the other regions, whereas most of the rod-like bones are located at the upper and lower regions, near to the intervertebral discs, as shown in Fig. 2.3.

Image analysis is generally used in order to investigate the morphological parameters of trabecular networks. Trabecular microarchitecture can be assessed easily *in vitro* by using micro-computed tomography (micro-CT) (Müller *et al.*, 1994) and in the peripheral region in *vivo* by employing quantitative-computed tomography (QCT) (Kopperdahl *et al.*, 2002) and magnetic resonance imaging (MRI) (Majumdar *et al.*, 1998; van Rietbergen *et al.*, 1998). However, micro-CT imaging is commonly used because its high-

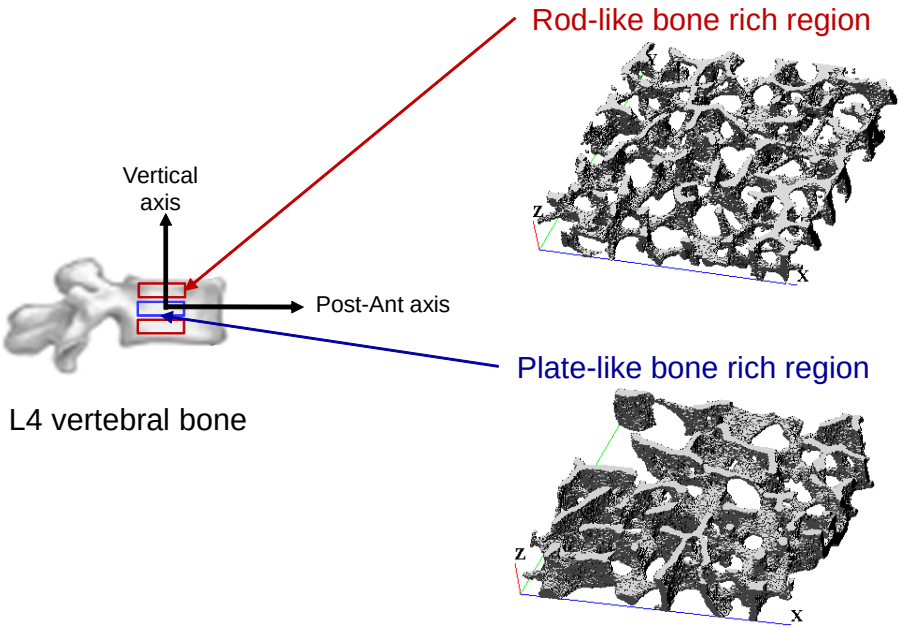

Figure 2.3: Plate-like and rod-like bone-rich regions.

resolution 3D images can capture the internal architecture of trabecular bone in detail; morphometric parameters can be computed directly from the 3D image without underlying model assumptions (Hildebrand and Ruegsegger, 1997). Recently, the evaluation of trabecular morphology has been extended to local individual trabeculae plates and rods. The relative importance of trabecular types (plates and rods) and the mechanical properties of trabecular bone have been studied by developing an image-processing technique for separating individual trabeculae (Pothuaud *et al.*, 2002; Stauber and Müller, 2006; Liu *et al.*, 2008b).

The developed techniques provide additional parameter measures for trabecular bone morphology and allow for investigations on the truly local parameters of a trabecular network. The line skeleton graph analysis (LSGA) method was introduced to compute topological parameters, including the length and volume of single trabeculae (Pothuaud *et al.*, 2000). This method can relate the effect of individual trabecular scales

on mechanical properties. Saha *et al.* (2000) developed digital topological analysis (DTA) for the characterization of trabecular architectures by subdividing trabeculae plates and rods based on a skeletonization technique. They showed that locally determined orientations described the anisotropy of a trabecular network better than the mean intercept length (MIL) parameter. More recently, the trabecular microstructure has been decomposed successfully into its basic elements (plates and rods) volumetrically (Stauber and Müller, 2006; Liu *et al.*, 2008b). Stauber and Müller (2006) showed that Tb.Sp, mean rod slenderness (<Ro.SI>), and the relative bone volume fraction of a rod (Ro.BV/BV) correlated strongly with the elastic modulus of vertebral trabecular bone. Liu *et al.* (2008b) reported that trabecular plates make a far greater contribution than rods to the apparent elastic behavior of trabecular bone. In short, all studies demonstrate trabecular morphology, which is characterized by various morphological parameters influence apparent mechanical properties.

2.5 Mechanical properties of trabecular bone

The mechanical properties of trabecular bone can be divided into two scales: Apparent and tissue levels. 'Apparent' properties are measured at the continuum level of a whole trabecular structure, as opposed to 'tissue' properties that are measured at the level of individual trabeculae. The hierarchical nature of bone implies that the apparent material behavior of trabecular bone is dependent on the mechanical properties of trabecular bone tissue (Fratzl and Weinkamer, 2007). Apparent trabecular bone exhibits approximately linear elasticity initially under both tensile and compressive loading; however, the failure mode is characteristically brittle in tension and more ductile in compression.

The apparent mechanical properties of trabecular bone are correlated strongly with bone density (Odgaard and Linde, 1991; Kopperdahl and Keaveny, 1998). In general, trabecular bone stiffness is related to bone density through a linear or power law relationship (Gibson, 1985; Keller, 1994; Keyak *et al.*, 1994). There is also a weak power relationship between bone stiffness and loading strain rate, which has been proposed to characterize the other influential factor in trabecular bone stiffness (Carter and Hayes, 1977; Linde *et al.*, 1991). Approximately 75% to 85% of the variation in apparent trabecular bone modulus is due to variations in apparent trabecular bone density (Mosekilde, 1993; Goulet *et al.*, 1994). However, numerous studies have been performed to investigate what factors other than bone density affect bone stiffness. All the factors were termed as bone quality, which includes bone morphology, mineralization, microdamage, and the structural organization of minerals and collagen within the bone matrix (Watts, 2002).

The apparent mechanical properties of trabecular bone are generally anisotropic, since the trabecular structure preferentially adapts to support the loads to which it is subjected. The stiffest and strongest loading direction corresponds to the principal material direction (the main direction of trabecular orientation). The mechanical properties of trabecular bone are always referred to with respect to the principal material axis, because this is the direction in which the load is subjected naturally (e.g. self-weight). Since this study is limited to linear elastic analysis, the mechanical behavior of trabecular bone damage over yield strength is not considered.

2.6 Image-based finite element (FE) modeling of trabecular bone

The assessment of the microarchitectural and mechanical properties of trabecular bone has benefited from recent advances in micro-CT and computer tools. These tools provide the ability to reconstruct a realistic trabecular microarchitecture model. Eight-node hexahedral elements are frequently used rather than four-node tetrahedral elements, because the first can be generated directly from micro-CT data. The conversion of bone voxel to a hexahedral element consists of a few basic steps, as follows. The micro-CT image is segmented, to distinguish bone voxels from non-bone (e.g. noise, artifacts, etc.). A global threshold is generally used in the binarization process, following which each bone voxel from the binarized image is converted into an eight-node brick element. Although voxel FE-based meshing is conceptually simple and easy to implement, this approach results in step-like discontinuities ('zig-zag') on the surface. The smoothness of the trabecular structure is reduced and can become worse if a low resolution image is used. However, Guldberg *et al.* (1998), who reported that step-like voxel FE meshes predict average stresses appropriately, though surface elements are subject to fluctuations in their true value, analyzed this approach using cantilever beam simulations. A minimum of four elements through the thickness is recommended, in order to account for bending. Niebur *et al.* (1999) confirmed this guideline by applying it to trabecular bone analysis. Hence, voxel FE-based meshing is acceptable for structural models, but it may be inappropriate when the accurate estimation of stresses and strains on trabecular surfaces is essential. To solve this problem, Takano *et al.* (2003) proposed to using a stress histogram to observe stress distribution in the FEM post-process.

Finite element analysis can be performed by assigning bone tissue properties and appropriate boundary conditions. Tissue properties are commonly assumed as being homogeneous, isotropic, and elastic due to computational cost and less experimental data at the tissue level. For instance, a value of Poisson's ratio ν is typically employed as 0.3 to 0.4, since it is difficult to obtain in experimental conditions. However, Ladd and Kinney (1998) reported that the apparent moduli predicted by FEM models are insensitive to ν—elastic moduli varied by less than 2% for ν in the ranges 0.15 through 0.35. Nevertheless, tissue property is anisotropy, because the heterogeneity of the mineralization and oscillation of BAp crystallite orientation lies within trabeculae, as discussed earlier. The heterogeneity effect has only recently been considered in FEM modeling.

van der Linden *et al.* (2001) found that the introduction of a less mineralized layer on the surface of trabecular struts, in order to model heterogeneity, reduced predicted apparent mechanical properties by up to 8%. The heterogeneity of trabecular bone tissue has also been introduced by scaling the properties of individual elements based on micro-CT attenuation measured at the corresponding voxel (Harrison *et al.*, 2008; Helgason *et al.*, 2008). This approach provides a new insight into a more realistic heterogeneous model of trabecular bone tissue. Nonetheless, the predicted apparent moduli are dependent on the assumption of an attenuation-modulus relationship as bone tissue properties. In all cases, bone tissue modeling as anisotropy results in reduced apparent mechanical properties compared to using the isotropy model.

2.7 Uncertainty quantification

Although morphological and biomechanical properties can be obtained with the aid of advanced imaging and experimental tools, as well as various micro-FE modeling techniques, errors and uncertainties within these methods may still occur when interpreting the results. In finite element modeling, numerical errors may arise due to the effect of the rough discretization of trabecular surfaces on the calculated apparent mechanical properties (Hollister and Riemer, 1993). Errors in finite element calculation also probably occur due to uncertainties in boundary conditions (Keaveny *et al.*, 1997). Since imaging techniques have become an important tool in reconstructing the appropriate trabecular architecture model, uncertainties in image-processing such as thresholding (Hara *et al.*, 2002; Yan *et al.*, 2012), resolution, artifacts, and noise (Rajapakse *et al.*, 2009a) could affect the reliability of any calculated mechanical properties. The systematic handling of uncertainty parameters in computational modeling is required, in order to ensure the credibility of the estimated result. The introduction of the ASME V&V 10-2006 standard (The American Society of Mechanical Engineers, 2006) has improved awareness among analysts about the importance of the appropriate choice of quality of interest and uncertainty quantification in contributing to the trustworthiness of the finite element model.

A consideration of uncertainty quantification is also essential in the evaluation of experimental results when the validation of computational modeling becomes a matter of concern (The American Society of Mechanical Engineers, 2006). Specimen preparation, the testing method, machine set-up, and the method used to interpret the results of experimental work cause uncertainty in the final result. The inconsistency of results materializes often, even though the same repeated experimental set-up is performed. It

becomes even more difficult if the standard procedure used for the experiment has not been established yet, such as in the biomechanics field. Numerous experimental studies on the mechanical properties of trabecular bone from various anatomical sites (Carter and Hayes, 1977; Ashman *et al.*, 1989; Keyak *et al.*, 1994) have been conducted, but the results are significantly scattered for each case. One of the major factors is the variation in bone characteristics due to inter-individual differences—a huge number of experimental works are required in order to propose a general solution caused by variety in age and gender, for instance. Hence, numerical simulation is a valuable tool that can model various types of uncertainty. Uncertainties that possibly arise in the assessment of mechanical properties of trabecular bone should be considered so that reliable results can be predicted.

Chapter 3

Voxel-based FE model of vertebral trabecular bone

3.1 Introduction

Over the last decade, the application of a three-dimensional (3D) graphics computer to reconstruct trabecular bone structure has grown in popularity thanks to improvements in imaging techniques and increased computational resources. In this technique, the complicated trabecular microstructure can be developed realistically by using high resolution images, which can be created by destructive methods, such as serial sectioning and serial milling techniques (Odgaard *et al.*, 1990; Beck *et al.*, 1997), or non-destructive methods (e.g. micro-computed tomography (CT) and micro-magnetic resonance (MR) imaging (Ulrich *et al.*, 1998; Judex *et al.*, 2003)). Micro-CT images have been widely used for creating images of trabecular bone due to their high resolution ($\sim 50\mu$m), rather than peripheral quantitative computed tomography (pQCT) ($\sim 160\mu$m) and MR ($\sim 300\mu$m)

(van Rietbergen *et al.*, 1998). A 3D voxel grid of the original trabecular structure can be rebuilt in the computer by stacking cross-sectional digitized images. Voxel grids representing bone tissue are then converted into equally shaped brick elements in a finite element (FE) model. Hence, in this research, the high resolution capabilities of micro-CT image are used to reconstruct a micro-FE model of vertebral trabecular bone.

3.2 Micro-computed tomography (CT) image

A micro-FE model of trabecular bone was reconstructed using micro-CT images. The fourth lumbar (L4) vertebral trabecular bone was extracted from three cadavers that were donated by Osaka City University Hospital and Osaka University. Based on Dual-energy X-ray Absorptiometry (DXA) analysis, two subjects were reported as healthy (two males, aged 66 and 68 years old) and the other one was osteoporotic (an 86-year-old female). A micro-CT device (SMX-100CT, Shimadzu, Kyoto, Japan), with a voltage of 40 kV and a current of 30 μA, was used to examine the bone specimens. The ethics committee approved the analysis of the bone specimens. The resolutions of the micro-CT images were 31.91 μm and 30.90 μm for the healthy bones and 29.92 μm for the osteoporotic bone. The slice thickness of the micro-CT was chosen to match the in-plane resolution. Figures 3.1 and 3.2 show the micro-CT images of the L4 vertebral trabecular body with standard anatomical axes for healthy and osteoporotic bones, respectively.

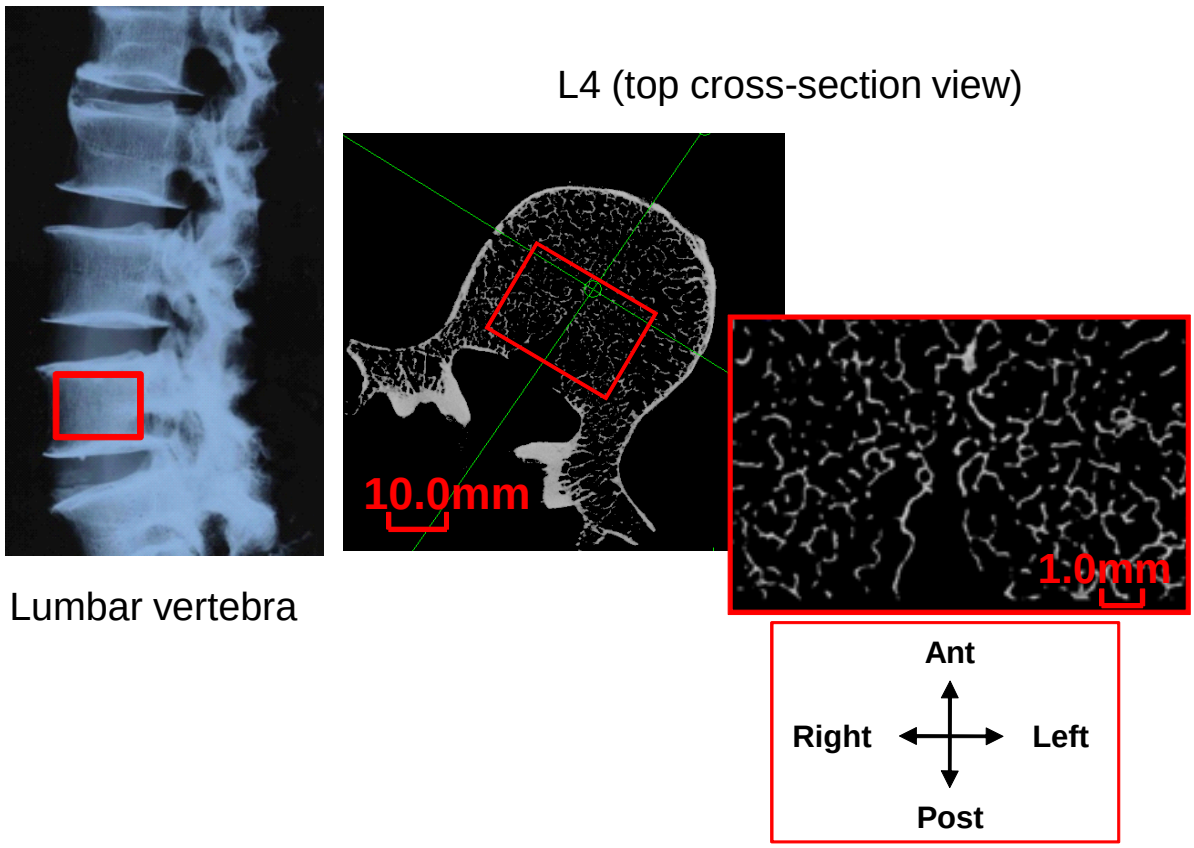

Figure 3.1: Micro-CT image of the lumbar vertebra for healthy trabecular bone.

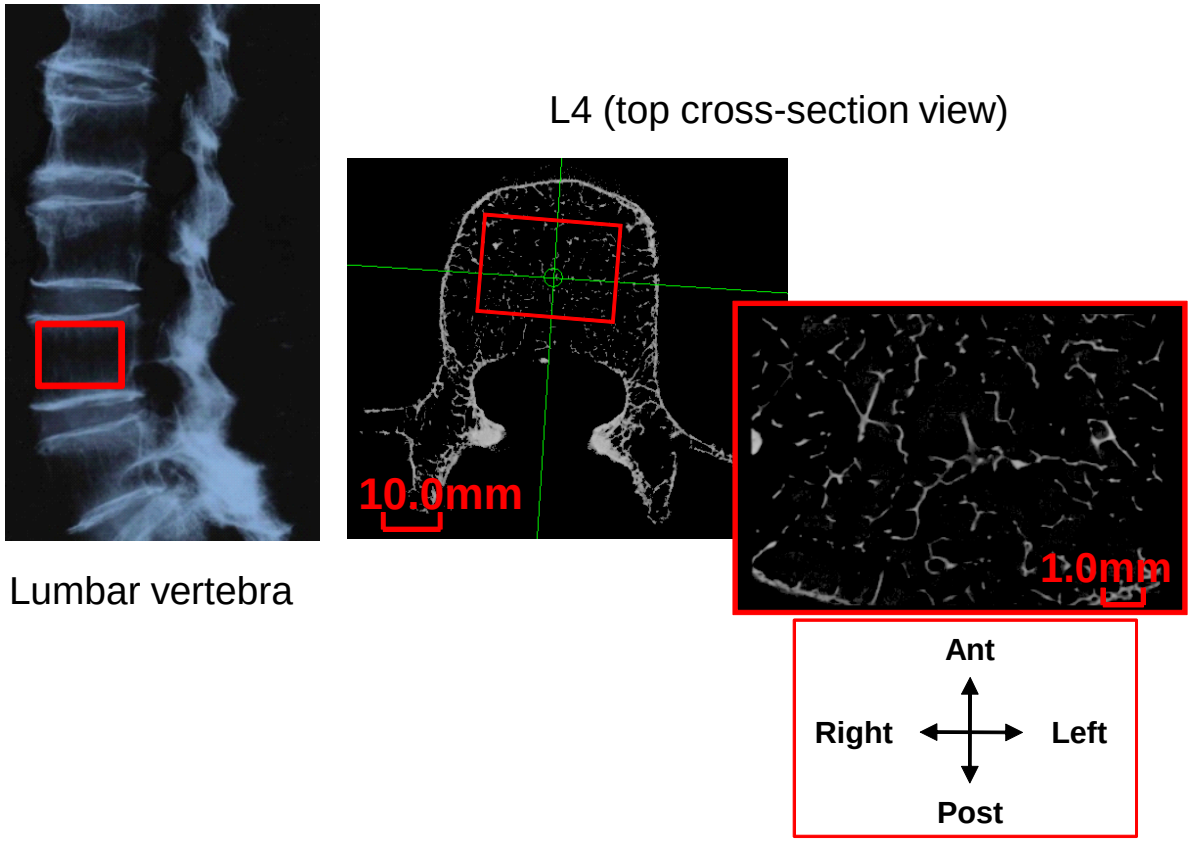

Figure 3.2: Micro-CT image of the lumbar vertebra for osteoporotic trabecular bone.

3.3 Voxel FE model

The 3D trabecular bone model was reconstructed using a sequential cross-section of binarized micro-CT images. The threshold of the segmentation image was determined by comparing the specific portion of the trabecular microstructure image with the cross-section of a real bone slice, to obtain the 3D binary image. An eight-node brick element mesh was generated by converting the trabecular bone voxel images (Hollister and Kikuchi, 1994) using DoctorBQ software (Cybernet Systems Co., Japan). Figure 3.3 (a-c) shows the 3D voxel element of the trabecular bone model for healthy bone No. 1, healthy bone No. 2, and the osteoporotic bone, respectively. The element size for each model was set equal to the micro-CT image resolution, such that voxels in the resulting reconstructions were equally sized in all spatial directions.

3.4 Extracting the region of interest (ROI) procedure

A microstructure model for finite element analysis and homogenization is known as the region of interest (ROI), because it is commonplace in biomechanics and is often used in X-ray measurements. That is equivalent to representative volume element (RVE) or unit cell in the computational mechanics field. The specific ROI was extracted from large reconstructed 3D voxel models (Fig 3.3). In the selection of ROIs, the distribution of areal bone density was carefully investigated, as shown typically in Fig. 3.4. In this thesis, axis-1, axis-2, and axis-3 are defined as axis left-right, post-ant, and vertical, respectively. Areal bone density is calculated by Eq. (3.1). For comparison, the standard

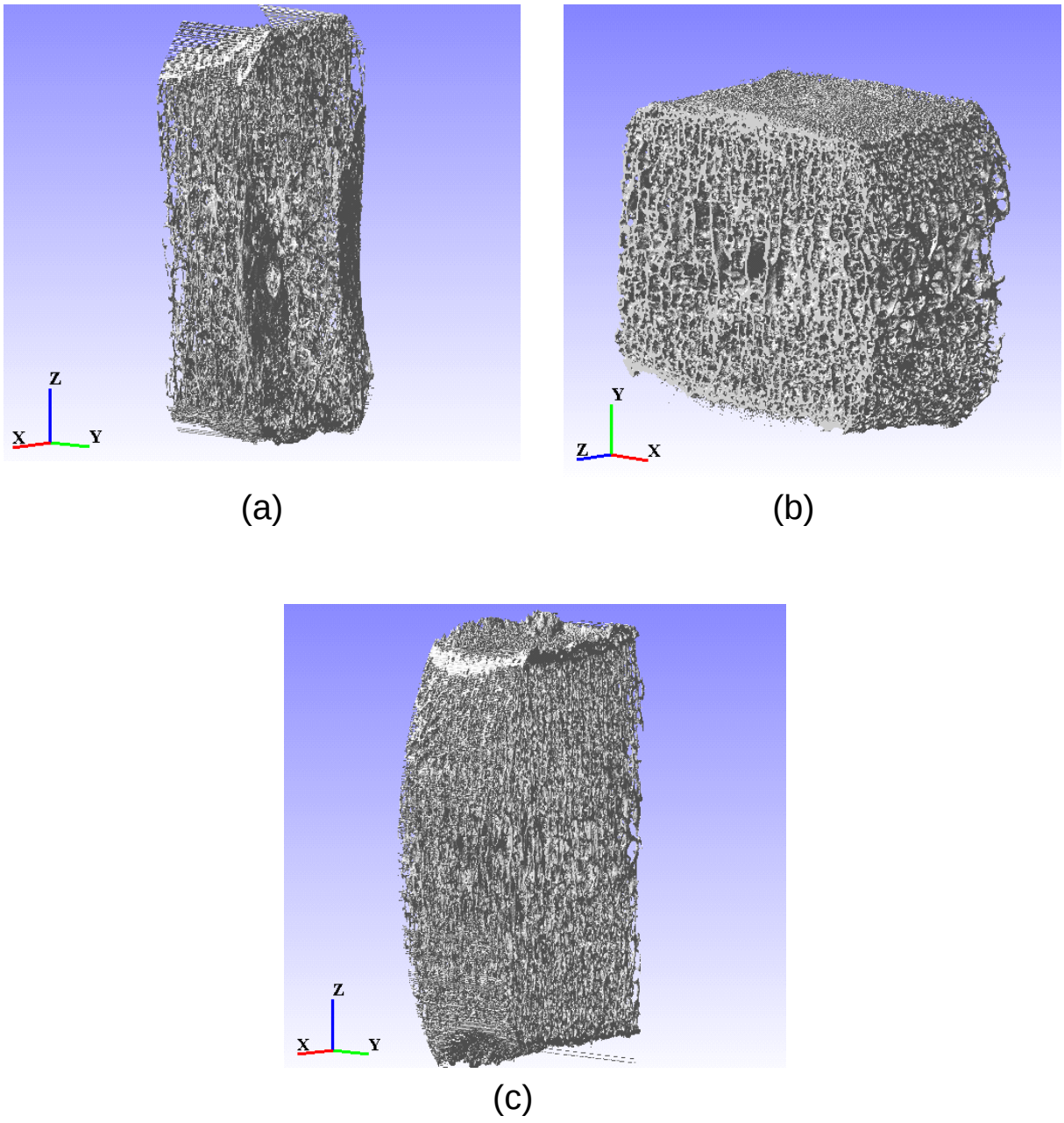

Figure 3.3: Voxel FE model of trabecular bone for (a) healthy bone No. 1, (b) healthy bone No. 2, and (c) osteoporotic bone No. 1.

definition of volumetric bone density (expressed simply as 'bone density') is also shown in Eq. (3.1).

$$\begin{aligned} \text{Areal bone density} &= \frac{1}{\acute{A}} \int \rho d\acute{A} \\ \text{Volumetric bone density} &= \frac{1}{\acute{V}} \int \rho d\acute{V} \end{aligned} \quad \left(\text{where } \rho = \begin{array}{ll} 1 & \text{for trabecular} \\ 0 & \text{for marrow} \end{array} \right) \tag{3.1}$$

where $\acute{A}$ is the cross-sectional area of the selected ROI and $\acute{V}$ is its volume. The green line displays the volumetric bone density of the ROI. In other words, the green line is the theoretical average of oscillating areal bone density. As shown in Fig. 3.4, this holds reasonably for this ROI; otherwise, the theory of homogenization, which will be used in further studies, fails. Besides, areal bone density at both boundaries must be almost the same, to assure the periodicity condition in the homogenization analysis. This is always necessary, in order to avoid numerical errors by assuming a periodicity condition. The slight difference in ROI location will affect the numerical result significantly. Consequently, Fig. 3.4 is very helpful for extracting an appropriate ROI for the homogenization method. The left-hand side figures showing the cross-section correspond to the red-marked location in the areal bone density graph. For the ROIs that were extracted from the osteoporotic bone, the distribution of areal bone density was examined in the same way. A reasonable definition of the average and the conditions necessary to assure periodicity were confirmed.

The apparent property of the whole trabecular region is a matter of concern in this study. Since the microstructure was random, as large ROIs as possible were analyzed. The periodic boundary conditions were placed on them in the homogenization analysis because it provides us with the most accurate and reliable solution, although periodicity

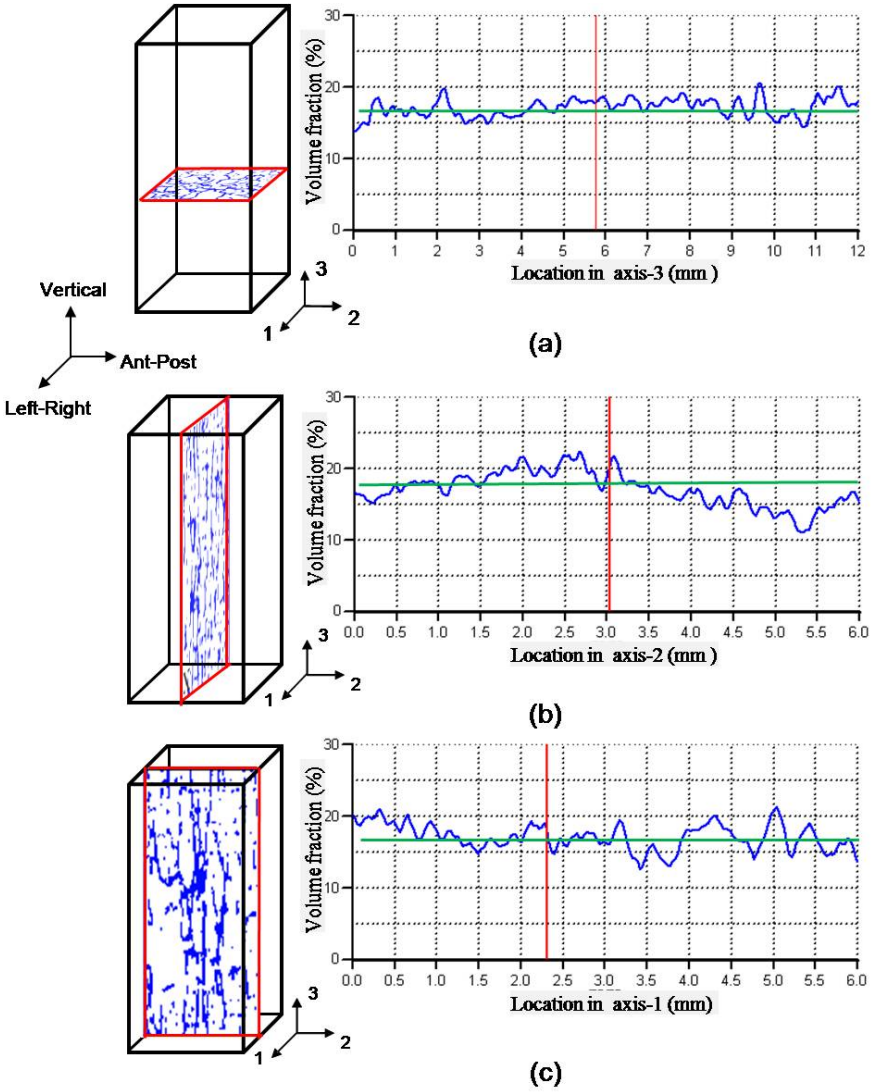

Figure 3.4: Areal bone density distribution for ROI No. 1. (a) Along the vertical axis. (b) Along the anterior-posterior axis. (c) Along the left-right axis.

is a hypothetical condition (refer to Appendix A2.2 for the micro-macro setting).

3.5 Selection of ROIs

Thirteen ROIs were selected from three lumbar vertebra bone specimens. Figure 3.5 shows the location of five ROIs from healthy bone No. 1. ROI No. 1 was selected as large as possible from the micro-CT images at 12 mm in height and covering almost the entire trabecular region in one lumbar vertebra. ROI No. 2, with a smaller cubic size of 4.0 mm×4.0 mm×4.0 mm, was selected from the middle side of lumbar, whilst ROIs No. 3 and No. 4 were extracted from the upper and lower sides near to intervertebral discs. The size satisfied the requirements of at least five intertrabecular lengths (Harrigan *et al.*, 1987). ROI H1 is located at the central part of the lumbar vertebra. Figure 3.6 shows the voxel FE model of all ROIs for healthy bone No. 1. ROIs No. 2 through No. 4 are local models representing plate-like and rod-like trabecular bone-rich regions, respectively. Large ROI No.1 represents the overall characteristics best, and it also contains the load paths in the trabecular bone studied later rather than small ROIs. Comparisons are made between large and small ROIs in this thesis. In the same manner, two ROIs—No. 5 and H2—were selected from healthy bone No. 2 with the same size and location as ROIs No. 1 and H1 of healthy bone No. 1, respectively, as shown in Figs. 3.7 and 3.8.

For the osteoporotic bone, six ROIs were chosen from the L4 body, as shown in Figs. 3.9 and 3.10. ROI No. 6 was selected with the size almost the same as the largest ROI for the healthy bone. ROIs No. 7 through No. 10 are the local models of ROI No. 6 with a variety of sizes and morphologies. ROI No. 8 was chosen so that a plate-like trabecular bone existed in the top region with a high number of rod-like trabecular

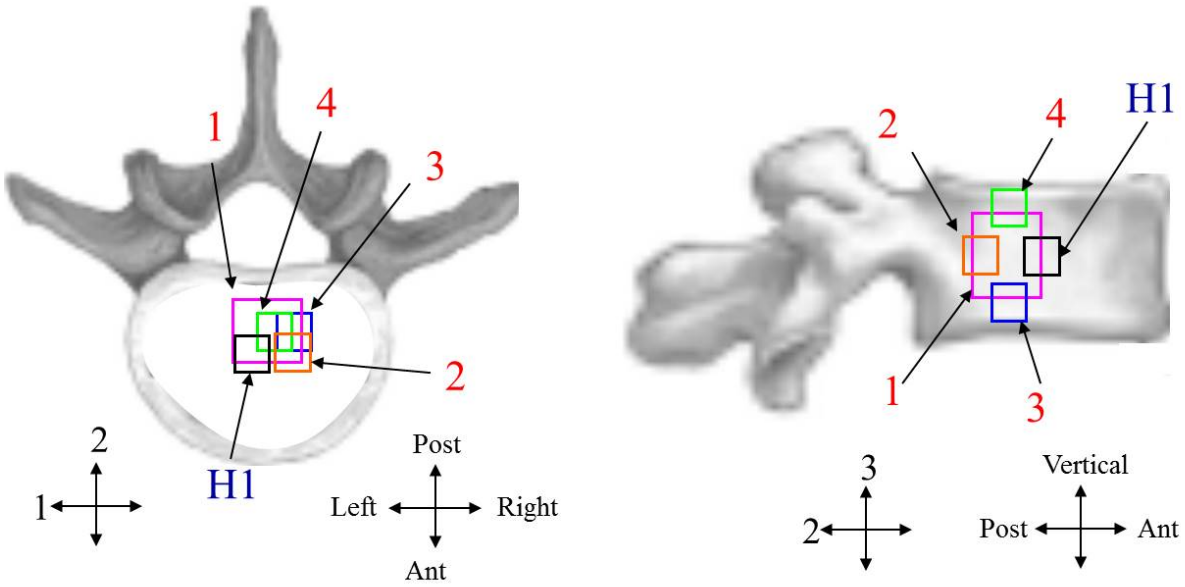

Figure 3.5: Location of ROIs for healthy bone No. 1.

bone elements, while ROI No. 10 was harvested with a hidden plate-like trabecular bone on the low side and one trabecular not connected to the bottom part. Detail in the trabecular microarchitecture was observed during the selection of the ROIs, in order to understand the effect of morphological characteristics on load-bearing distribution. ROI O1 was selected at the central part, in the same manner as the selection of ROIs H1 and H2. The specifications for each selected ROI are shown in Table 3.1.

Two types of material axes set up on the ROI were used in this thesis. The first setup was applied for deterministic homogenization analysis (including dynamic analysis) and the other one for stochastic homogenization analysis. The details of both setups are described in sections A2 and A3 in Appendix A. ROIs H1, H2, and O1 used the setup for stochastic homogenization analysis, whereas the rest of the ROIs used the setup for deterministic homogenization analysis.

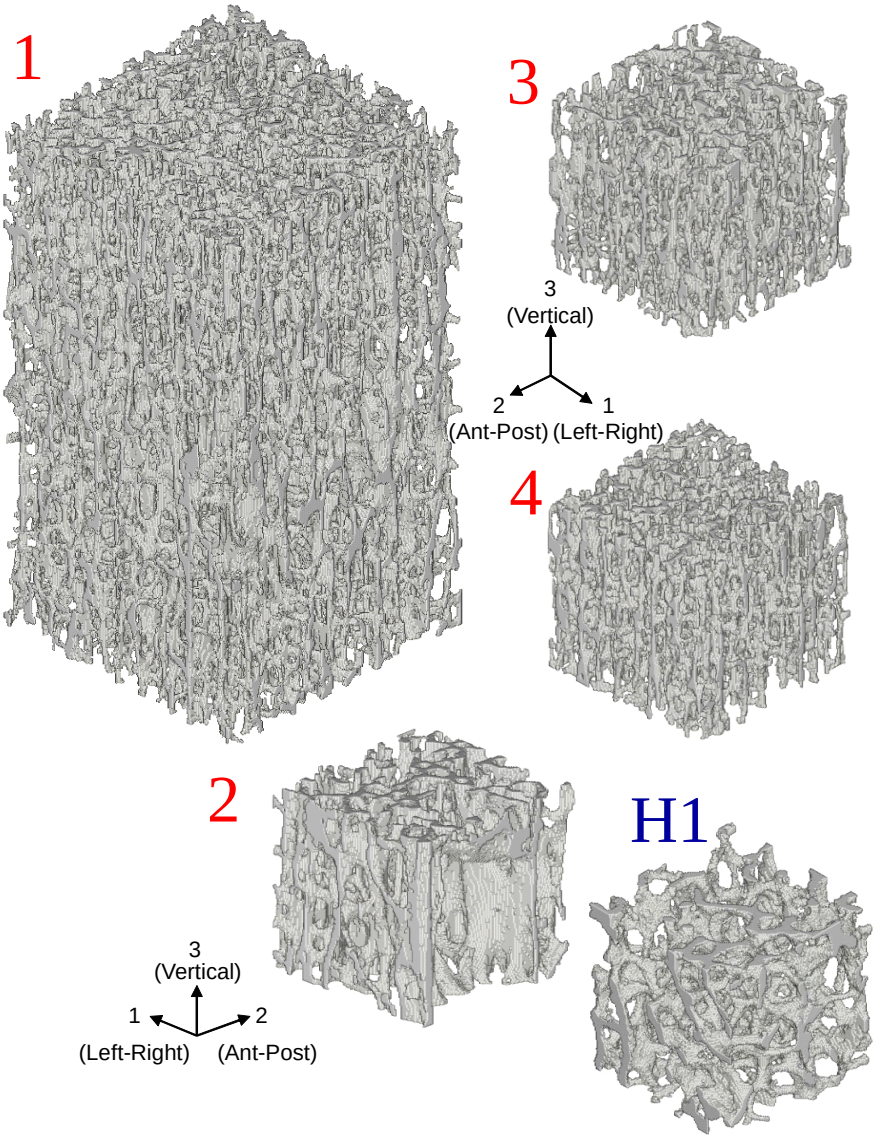

Figure 3.6: Voxel FE model of ROIs for healthy bone No. 1.

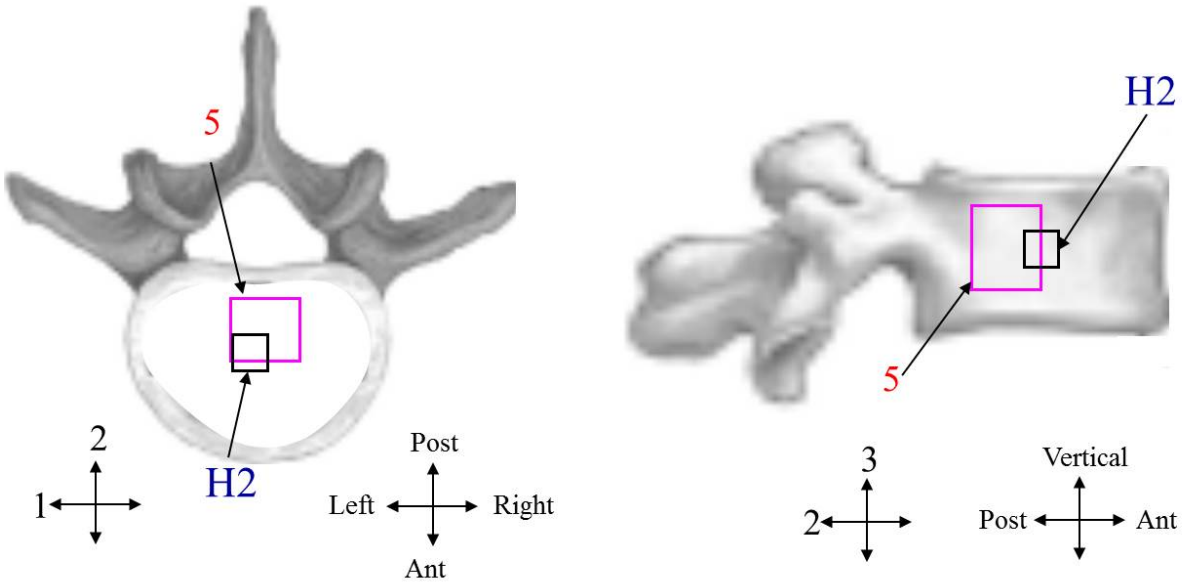

Figure 3.7: Location of ROIs for healthy bone No. 2.

Table 3.1: Specification of ROIs

Bone specimen	ROI No.	ROI size (mm^3)	Bone density (g/cm^3)	No. of voxels
Healthy No. 1	1	$6 \times 6 \times 12$	0.172	2,781,416
	2	$4 \times 4 \times 4$	0.177	353,122
	3	$4 \times 4 \times 4$	0.159	382,521
	4	$4 \times 4 \times 4$	0.169	406,477
	H1	$4 \times 4 \times 4$	0.162	455,531
Healthy No. 2	5	$6 \times 6 \times 12$	0.256	3,809,687
	H2	$4 \times 4 \times 4$	0.215	798,523
Osteoporotic No. 1	6	$5 \times 6.6 \times 12$	0.06	877,277
	7	$5 \times 5 \times 8.4$	0.064	502,103
	8	$2.7 \times 2.7 \times 8.4$	0.056	146,953
	9	$2.7 \times 2.7 \times 6$	0.063	92.484
	10	$2.1 \times 2.1 \times 4$	0.079	53,091
	O1	$4 \times 4 \times 4$	0.075	274,697

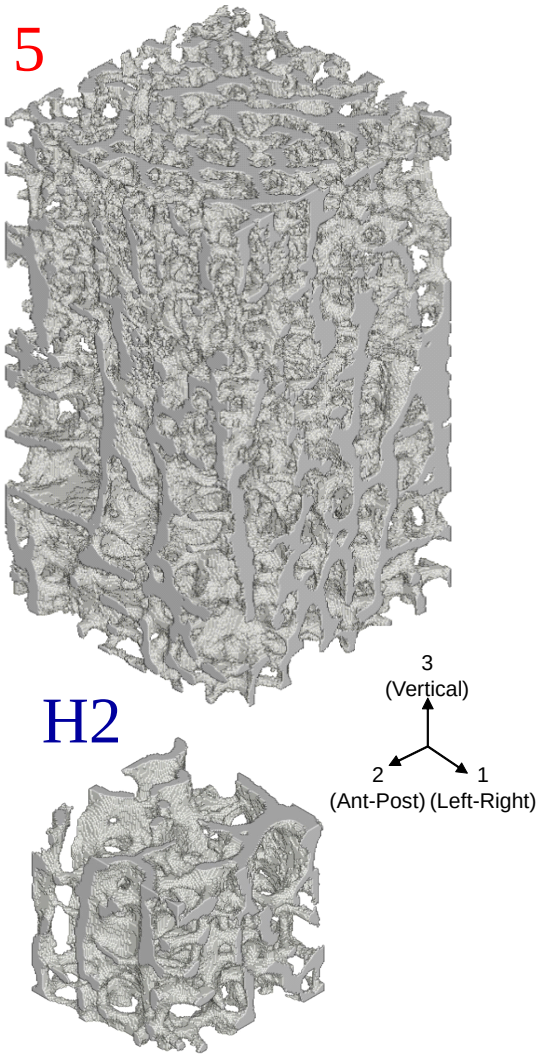

Figure 3.8: Voxel FE model of ROIs for healthy bone No. 2.

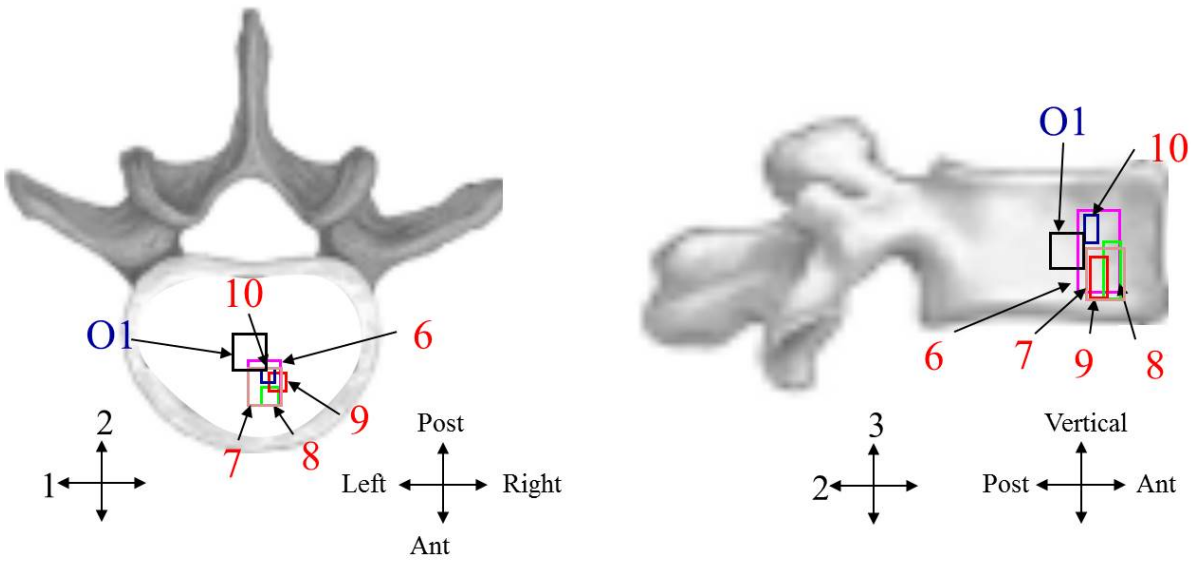

Figure 3.9: Location of ROIs for osteoporotic bone No. 1

Two small-sized ROIs (No. 8 and No. 10) and two large ROIs (No. 1 and No. 6) were chosen for morphology analysis under dynamic loading. The size of the ROI is crucial in dynamic analysis because if the ROI contains a large number of elements, the computational cost can be enormous. Hence, large enough ROIs with reasonable numbers of voxel elements were selected.

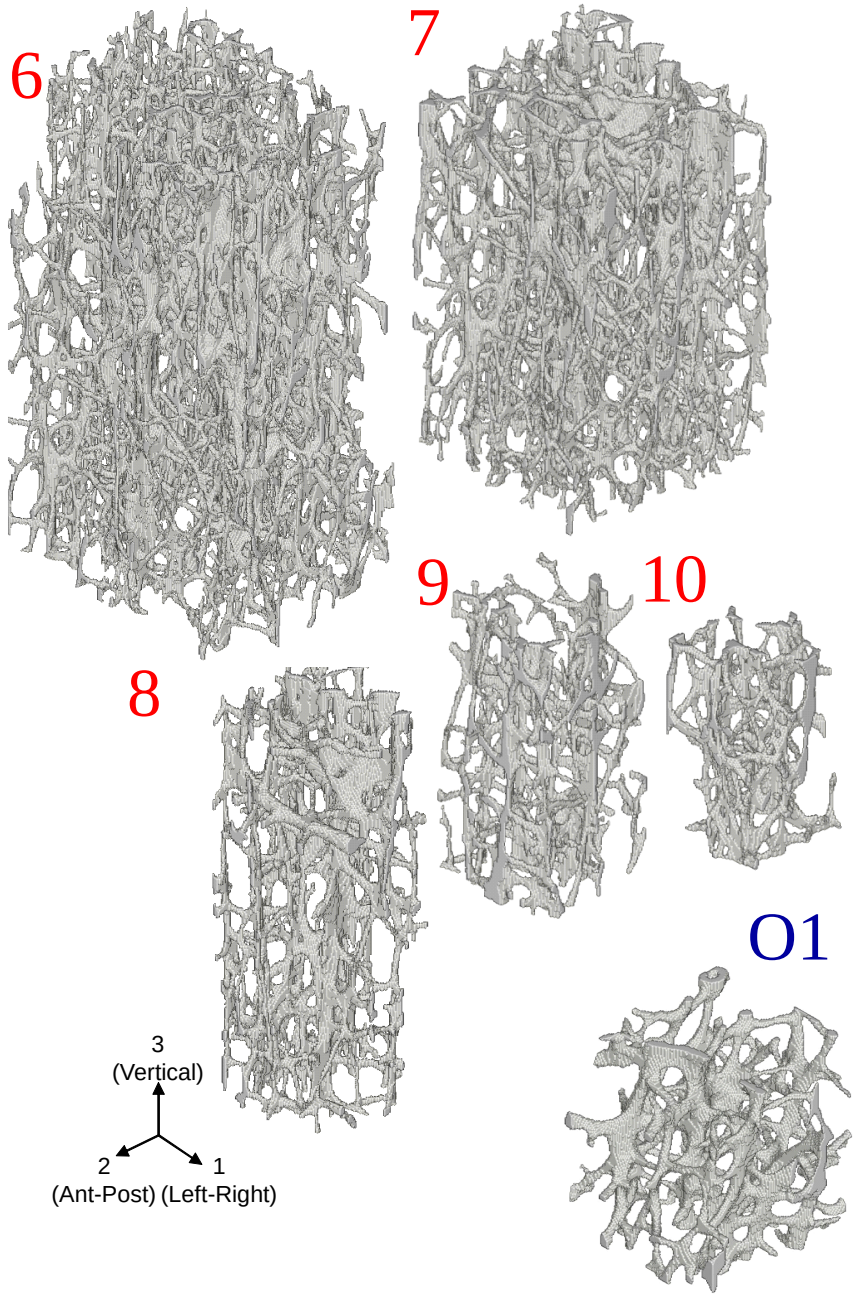

Figure 3.10: Voxel FE model of ROIs for osteoporotic bone No. 1.

Chapter 4

Morphology analysis based on the homogenization method

4.1 Introduction

The complexity of trabecular bone morphology is attractive to many researchers because bone architecture appears to play a key role in determining bone quality (Judex *et al.*, 2003; Dalle Carbonare *et al.*, 2005). Trabecular bone supports mechanical stress and reacts to it by changing its microarchitecture. The microarchitecture of trabeculae contributes to load distribution capacity, particularly to the optimal stiffness and strength per trabecular bone mass (Gefen, 2009). Many morphological parameters have been used to characterize the microarchitecture of trabecular bone, among them apparent bone density, trabecular thickness and spacing, the spatial arrangement of individual trabeculae, intertrabecular connectivity, and others (Shi *et al.*, 2009; Syahrom *et al.*, 2011). However, little is known about the mechanical role of trabecular morphology in the context

of load-bearing behavior. To study this role, the trabecular network should be observed from a local point of view. Since it is difficult to observe the complex trabecular microarchitecture, the decomposition of trabeculae into classified groups or types is necessary, to evaluate the role of the individual trabecular segment.

With the aid of advanced tools available nowadays, trabecular bone microstructure can be captured easily. Three-dimensional imaging of trabecular bone (Müller *et al.*, 1994; Majumdar *et al.*, 1998) has become commonplace since the advent of high-resolution scanners. However, not many computational schemes are available to decompose trabecular volume so that the morphology of the trabecular bone can be visualized in selected portions. Stauber and Müller (2006) were the first to introduce a method for the volumetric spatial decomposition of trabecular bone into individual rods and plates by using a skeletonization approach. This technique enables the computation of morphological parameters for each element within the trabecular bone structure, allowing for the first time an investigation of the truly local morphometric parameters of rods and plates in the trabecular bone network separately. Liu *et al.* (2006) developed a similar procedure, based on a digital topological analysis-preserving skeletonization technique, to fully decompose trabecular bone microstructure into individual rods and plates. This approach provides a better characterization of the morphology and orientation of trabecular bone. Both methods were developed based on advances in image-processing techniques. Since the morphology of living human bone relates to the effects of its internal mechanical loads Weinans *et al.* (1992) on bone remodeling processes (Liu *et al.*, 2008a; Kameo *et al.*, 2011), it would be a better approach if the mechanical load was considered during trabecular bone decomposition procedures.

Analyzing the mechanical stress on a trabecular bone volume requires a multi-scale

method, in order to ensure that the selected volume represents an infinite number of cells. The use of multi-scale theory, which bridges micro-meso-macroscopic relationships in bone tissue, has been well established in the past two decades (Hollister *et al.*, 1991, 1994; Parnell *et al.*, 2006; Kosturski and Margenov, 2010). Hollister *et al.* (1991) applied asymptotic homogenization theory to the study of trabecular bone mechanics by combining the microstructural analysis of porous structures with standard continuum finite element analysis. Parnell *et al.* (2006) used an asymptotic homogenization method to determine the local effective elastic properties of cortical bone by developing a mathematical model that can solve the cell problem. The homogenization theory can predict both macroscopic properties based on microstructural and microscopic responses under macroscopic boundary conditions.

Therefore, in this chapter, we use the homogenization method, in order to calculate the apparent elastic moduli of vertebral trabecular bones with various bone densities and morphologies. Since the relations between bone density and Young's modulus have been described by many research works, such as Keyak *et al.* (1994), Keller (1994), or Carter and Hayes (1977), as a result of experiments, the calculated apparent Young's modulus is compared with Keyak et al.'s experimental result, which was frequently referred to for validation. Next, by virtue of the particular characteristic of homogenization theory, a new classification method is proposed to study the morphology and mechanical role of the trabecular network under macroscopic (apparent) loading conditions. With regards to the observation on the differences in trabecular bone microarchitectures, the effect of morphology on the apparent Young's moduli and shear moduli is also investigated.

4.2 Homogenization theory

Since trabecular bone is regarded as a heterogeneous cellular medium (Gibson and Ashby, 1997), the asymptotic homogenization method of multi-scale theory and the finite element method were used to solve the derived partial differential equations (refer also to Appendix A2.2 for the micro-macro setting). Although the homogenization theory was initially formulated for periodic microstructure (Sanchez-Palencia, 1980; Guedes and Kikuchi, 1990), its accuracy has also been proved in the literatures (Takano *et al.*, 2003, 2010), even for materials with random microstructures. Consider trabecular bone from the fourth lumbar vertebra formed by the spatial repetition of ROI Y at microscopic scale y that is very small and of order λ compared with the dimensions of structural body Ω at macroscopic scale x. Note again, ROI is often used in measurements especially in biomechanics field. That is equivalent to representative volume element (RVE) or unit cell in the computational mechanics field. The relationship between the microscopic and macroscopic scales is then written as follows:

$$y = \frac{x}{\lambda} \tag{4.1}$$

Due to the periodic nature of the microstructure, the dependence of microscopic variable y is also periodic, specifically Y-periodic. Hence, the total microstructural displacement should consider both the microscopic and macroscopic levels. Total microstructural displacement is assumed to be expressed as an asymptotic expansion with respect to parameter λ (the ratio of macroscopic to microscopic scales), as in the following:

$$u_i = u_i(x, y) = u_i^0(x) + \lambda u_i^1(x, y) \tag{4.2}$$

where the second and higher order terms are neglected, u_i^0 is a displacement at the macroscopic or apparent level, and u_i^1 denotes a perturbed displacement term as a result of the microstructure. Total strain e_{ij} is then expressed by

$$\begin{aligned} e_{ij} &= e_{ij}^0 + e_{ij}^1 \\ &= \frac{1}{2}\left(\frac{\partial u_i^0}{\partial x_j} + \frac{\partial u_j^0}{\partial x_i}\right) + \frac{1}{2}\left(\frac{\partial u_i^1}{\partial y_j} + \frac{\partial u_j^1}{\partial y_i}\right) \end{aligned} \tag{4.3}$$

where e_{ij}^0 is strain at the apparent level and e_{ij}^1 denotes microscopic strain. Neglecting body force and assuming traction force t_i is applied only to the continuum smooth boundary Γ_t, the weak form of the equilibrium equation can be written as follows:

$$\int_\Omega D_{ijkl}^\lambda \frac{\partial u_k^\lambda}{\partial x_l}\frac{\partial v_i^0}{\partial x_j} d\Omega = \int_\Gamma t_i v_i^\lambda d\Gamma \tag{4.4}$$

where v_i is the virtual displacement and D_{ijkl} is an elastic tensor modeled as transversely isotropic by considering the c-axis BAp crystallite orientation.

For a Y-periodic function $\Psi(y)$, by taking the limit of $\lambda \to 0$, the integral in Eq. (4.4) can be separated into microscopic and apparent levels by using the averaging principal, as expressed in the following:

$$\lim_{\lambda\to 0}\int_\Omega \Psi^\lambda\left(\frac{x}{\lambda}\right) d\Omega = \int_\Omega \frac{1}{|Y|}\int_Y \Psi(y) dY d\Omega \tag{4.5}$$

where $|Y|$ is the volume of ROI. Introducing the asymptotic expansion of Eq. (4.2) in Eq. (4.4) and neglecting the traction force at the microscopic level yields

$$\int_\Omega D_{ijkl}^\lambda \left(\frac{\partial u_k^0}{\partial x_l} + \frac{\partial u_k^1}{\partial y_l}\right)\left(\frac{\partial v_i^0}{\partial x_j} + \frac{\partial v_i^1}{\partial y_j}\right) d\Omega = \int_{\Gamma_t} t_i v_i^0 d\Gamma \tag{4.6}$$

Based on the averaging function obtained in Eq. (4.5), Eq. (4.6) is then rewritten as follows:

$$\int_{\Omega} \frac{1}{|Y|} \int_{Y} D_{ijkl} \left(\frac{\partial u_k^0}{\partial x_l} + \frac{\partial u_k^1}{\partial y_l} \right) \left(\frac{\partial v_i^0}{\partial x_j} + \frac{\partial v_i^1}{\partial y_j} \right) dY d\Omega = \int_{\Gamma_t} t_i v_i^0 d\Gamma \tag{4.7}$$

Since no traction force is applied on the microscopic level, Eq. (4.7) can be separated into microscopic and macroscopic equations as written in Eq. (4.8) and Eq. (4.9), respectively.

$$\int_{\Omega} \frac{1}{|Y|} \int_{Y} D_{ijkl} \left(\frac{\partial u_k^0}{\partial x_l} + \frac{\partial u_k^1}{\partial y_l} \right) \frac{\partial v_i^1}{\partial y_j} dY d\Omega = 0 \tag{4.8}$$

$$\int_{\Omega} \frac{1}{|Y|} \int_{Y} D_{ijkl} \left(\frac{\partial u_k^0}{\partial x_l} + \frac{\partial u_k^1}{\partial y_l} \right) \frac{\partial v_i^0}{\partial x_j} dY d\Omega = \int_{\Gamma_t} t_i v_i^0 d\Gamma \tag{4.9}$$

Microscopic displacement depends on macroscopic boundary conditions and macroscopic deformation. Hence, the unique solution for microscopic displacement can be expressed as follows:

$$u_i^1 = -\chi_i^{kl}(y) \frac{\partial u_k^0(x)}{\partial x_l} \tag{4.10}$$

where χ^{kl} is characteristic displacement, which is a periodic function of y. The characteristic displacement has six modes of microstructure displacement, which reflects the mismatch between the mechanical properties and the geometrical configuration of the element. Substituting Eq. (4.10) into Eq. (4.8) yields

$$\int_{\Omega} \frac{1}{|Y|} \left\{ \int_{Y} \left(D_{ijkl} - D_{ijmn} \frac{\partial \chi_m^{kl}}{\partial y_n} \right) \frac{\partial v_i^1}{\partial y_j} dY \right\} \frac{\partial u_k^0}{\partial y_l} d\Omega = 0 \tag{4.11}$$

Considering only the microscopic part of Eq. (4.11), the microscopic equation is obtained as follows:

$$\int_{Y} \left(D_{ijkl} - D_{ijmn} \frac{\partial \chi_m^{kl}}{\partial y_n} \right) \frac{\partial v_i^1}{\partial y_j} dY = 0 \tag{4.12}$$

where χ^{kl} is the solution for Eq. (4.12) using the periodic boundary condition. Using the same approach, substituting Eq. (4.10) into Eq. (4.9) gives the following equation.

$$\int_\Omega \frac{1}{|Y|} \int_Y \left(D_{ijkl} - D_{ijmn} \frac{\partial \chi_m^{kl}}{\partial y_n} dY \right\} \frac{\partial u_k^0}{\partial x_l} \frac{\partial v_i^0}{\partial x_j} d\Omega = \int_{\Gamma_t} t_i v_i^0 d\Gamma \tag{4.13}$$

Since Eq. (4.13) can represent the apparent level problem, the interior integral part is then the apparent stiffness of ROI Y, also known as the homogenized elastic tensor D_{ijkl}^H, which can be calculated by solving Eq. (4.12) and is expressed as below.

$$D_{ijkl}^H \equiv \frac{1}{|Y|} \int_Y \left(D_{ijkl} - D_{ijmn} \frac{\partial \chi_m^{kl}}{\partial y_n} \right) dY \tag{4.14}$$

Note here that, in solving the microscopic equation, Eq. (4.12), for osteoporotic trabecular bone with very low bone density, the periodic boundary condition is barely assigned. In such an ill-conditioned problem, we used a wrapping element layer (Takano *et al.*, 2008) for the microstructure model, in order to obtain an accurate solution. The Young's modulus of the wrapping element was set 10^{-5} times smaller than that of bone tissue. In this analysis, most of the computational time was spent on solving microscopic equations. One of the reasons is that the number of voxel finite elements was large and the element-by-element scaled conjugate gradient (SCG) method, which is an iterative equation solver, was used. Especially when the anisotropy of the bone tissue is considered, the convergence of the SCG solver becomes extremely slow.

4.3 Apparent elastic moduli

By considering the existence of *c*-axis BAp crystallite, the Young's moduli of bone tissue was set as an orthotropic model. Young's modulus in the *c*-axis was $E_c = 10$ GPa and other orthogonal axes are $E_a = E_b = 5$ GPa, whereas the Poisson's ratio was determined as $\nu_{ca} = \nu_{cb} = \nu_{ab} = \nu_{ba}$ =0.4 and $\nu_{ac} = \nu_{bc}$ =0.2, to hold the symmetry of the elastic tensor. A Young's modulus of 10 GPa, as the trabecular bone tissue property, has been commonly used (van Rietbergen *et al.*, 1995; van Ruijven *et al.*, 2007; Bevill and Keaveny, 2009; Mc Donnell *et al.*, 2009) and experimentally obtained (Rho *et al.*, 1993; Nicholson *et al.*, 1997; Hou *et al.*, 1998) in many research works. The shear moduli of bone tissue were assumed as isotropic, with $G_{bc} = G_{ca} = G_{ab}$ =1.8 GPa. The orthotropic material model was applied reasonably, without any rotation of the axes for all ROIs. Details regarding the anisotropy setup for trabecular bone tissue are available in Appendix A.

Figures 4.1 and 4.2 show the comparison between healthy and osteoporotic bones based on the averages of the calculated apparent Young's moduli and the ratio of Young's moduli in the lateral to the vertical axis, respectively. The error bar indicates the maximum and minimum calculated results for the selected ROIs. For healthy bone (ROIs No. 1 through No. 4), apparent Young's moduli are found as transverse-isotropic at axis-1 (right-left) and axis-2 (posterior-anterior). Meanwhile, the apparent Young's moduli for osteoporotic bone (ROIs No. 6 through No. 9) show anisotropy. In the same manner, a comparison between healthy and osteoporotic bones on the calculated shear moduli is presented in Figs. 4.3 and 4.4. The apparent shear moduli with respect to the vertical direction for healthy bones are two times higher than in the lateral direction. The transverse-isotropic characteristic is also found in the calculated apparent shear moduli

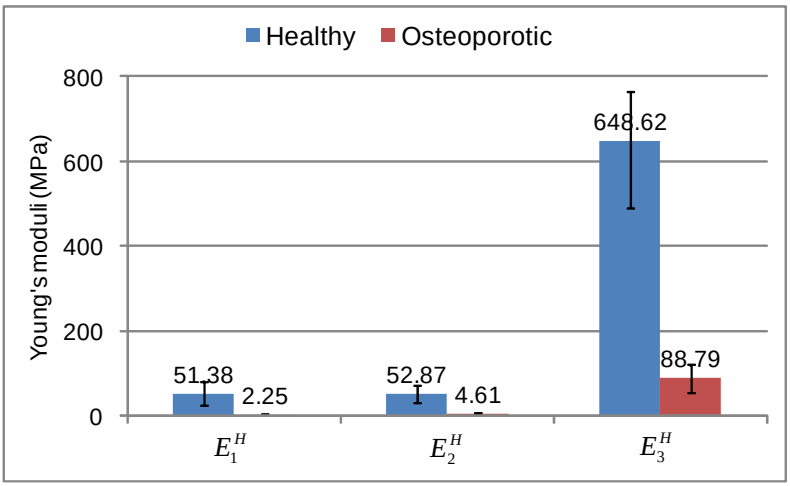

Figure 4.1: Comparison of Young's moduli between healthy and osteoporotic bones. Error bar indicates the maximum and minimum values.

of the healthy case. Moreover, the apparent shear modulus in the lateral directions (G_{31}^H and G_{23}^H) is higher than G_{12}^H, and the ratio to G_{12}^H is larger for the osteoporotic bone than the healthy bone. This means that the degree of anisotropy increases for osteoporotic bone. In other words, the decrease in stiffness in the left-right and post-ant directions is greater than the decrease in stiffness in the axial direction. The calculated apparent Young's moduli and apparent shear moduli for all ROIs are listed in Tables 4.1 and 4.2, respectively.

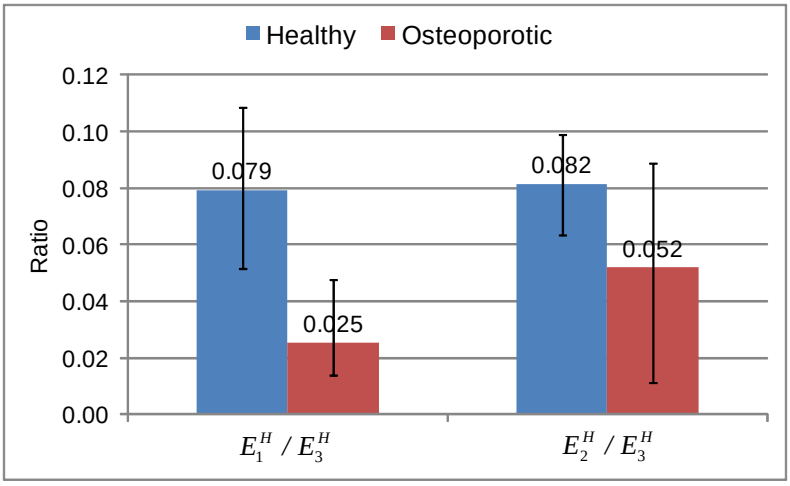

Figure 4.2: Comparison of the ratio of Young's moduli in the lateral to the vertical axis between healthy and osteoporotic bones.

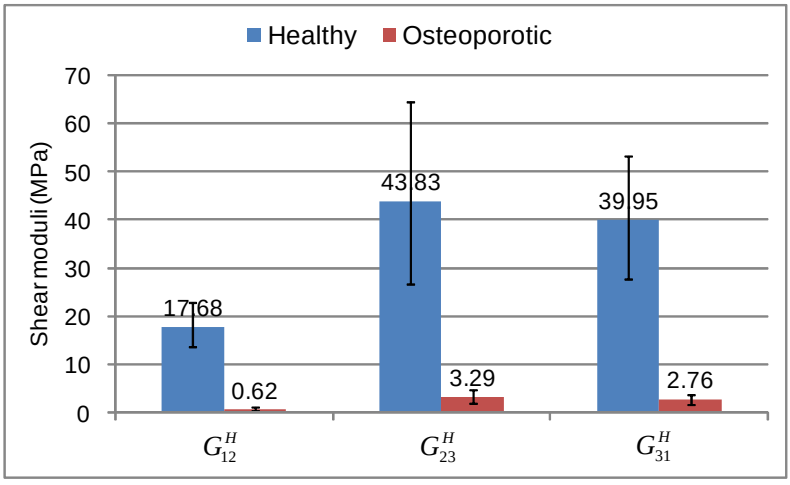

Figure 4.3: Comparison of shear moduli between healthy and osteoporotic bones.

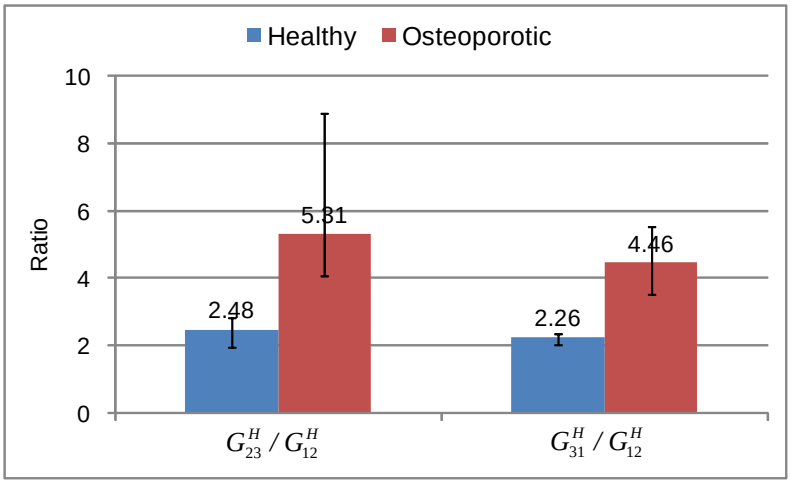

Figure 4.4: Comparison of the ratio of shear moduli in the lateral to the vertical axis between healthy and osteoporotic bones.

Table 4.1: Apparent Young's moduli

Bone specimen	ROI No.	E_1^H (MPa)	E_2^H (MPa)	E_3^H (MPa)	E_1^H/E_3^H	E_2^H/E_3^H
Healthy No. 1	1	58.5	67.2	765.0	0.077	0.088
	2	80.9	73.7	746.3	0.108	0.099
	3	25.4	33.0	490.5	0.052	0.067
	4	40.7	37.6	592.7	0.069	0.063
Healthy No. 2	5	274.8	271.2	1001.2	0.274	0.271
Osteoporotic No. 1	6	1.21	6.51	87.9	0.014	0.074
	7	1.69	9.57	107.6	0.016	0.089
	8	5.80	1.39	121.2	0.048	0.011
	9	0.78	1.01	56.1	0.014	0.018
	10	1.75	4.57	71.2	0.025	0.064

Table 4.2: Apparent shear moduli

Bone specimen	ROI No.	G_{12}^H (MPa)	G_{23}^H (MPa)	G_{31}^H (MPa)	G_{23}^H/G_{12}^H	G_{31}^H/G_{12}^H
Healthy No. 1	1	20.2	51.6	46.2	2.552	2.284
	2	22.9	64.5	53.2	2.813	2.318
	3	13.7	26.7	27.8	1.947	2.026
	4	13.9	32.5	32.7	2.349	2.363
Healthy No. 2	5	98.7	121.5	115.0	1.231	1.165
Osteoporotic No. 1	6	0.46	4.08	2.55	8.870	5.543
	7	1.05	4.68	3.68	4.479	3.519
	8	0.58	2.37	3.19	4.079	5.491
	9	0.393	2.023	1.637	5.148	4.165
	10	0.307	1.647	8.39	5.365	27.329

The calculated apparent Young's modulus in the vertical axis for all ROIs was then plotted along with the experimental results performed by Keyak *et al.* (1994), with respect to bone density, as shown in Fig. 4.5. The numbers in the plot represent the ROI Nos. Keyak's result was obtained using thirty six trabecular bone specimens that were extracted from the proximal portion of two pairs of tibiae from a 45-year-old man and a 40-year-old woman. Although Keyak *et al.* (1994) obtained a regression equation for the Young's modulus in the vertical direction as $E = 33,900\rho^{2.2}$, the original experimental results show surprisingly widespread scattering. The regression line is almost the average of the experimental results' dispersion. Good agreement with this line proves the reliability of our calculation. The result also suggests that the setup of material axes in two different methods (as described in section 3.5) is not significant as far as the apparent Young's modulus in the vertical axis is concerned, because the predicted properties of ROI H1, H2, and O1 coincide with the numerical results of other ROIs.

On the other hand, Fig. 4.5 implies that the apparent Young's modulus is not dependent on bone density only. For instance, some ROIs with high bone density (ROI No. 2) give a lower apparent Young's modulus than those with lower bone density (ROI No. 1). This fact proves the influence of other factors in contributing to bone strength. Obviously, trabecular bone morphology could be a major factor in this case, because connectivity and network architecture influence load-bearing capability. A further investigation into the uncertainty factor will be described in Chapter 6, in which the contribution of trabecular morphology to the load path will be investigated from a local viewpoint by using the proposed classification method.

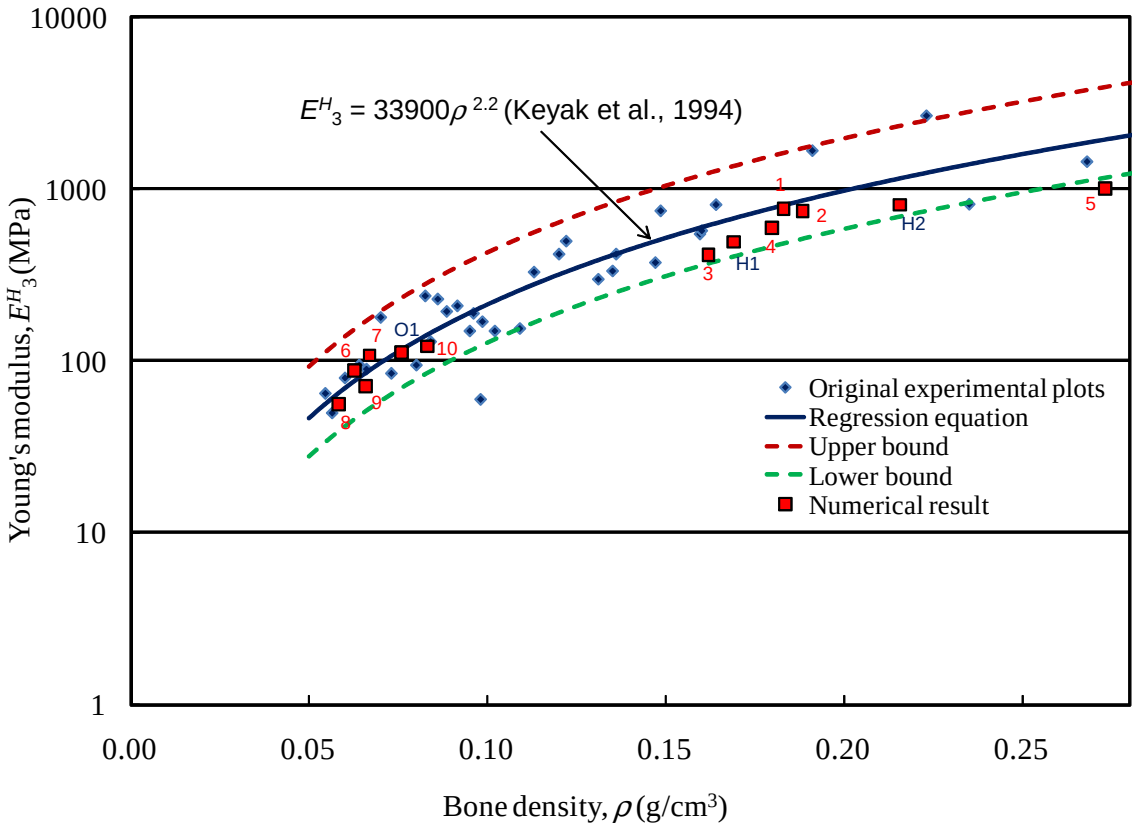

Figure 4.5: Apparent Young's modulus in the vertical axis and a comparison with Keyak et al.'s experimental result.

4.4 Classification method

A classification method is proposed to reduce the model size of the complicated trabecular microarchitecture, in order to improve visibility so that the morphology of the trabecular bone can be described in line with network architecture. This method is developed by means of homogenization theory, the merit of which lies in its ability to determine microscopic stress. Substituting the expression of apparent stiffness in Eq. (4.14) into Eq. (4.13), the macroscopic equation holds:

$$\int_{\Omega} D^H_{ijkl} \frac{\partial u^0_k}{\partial x_l} \frac{\partial v^0_i}{\partial x_j} d\Omega = \int_{\Gamma_t} t_i v^0_i d\Gamma \tag{4.15}$$

The microscopic stress σ_{ij} can be obtained through Eq. (4.16).

$$\begin{aligned} \sigma_{ij} &= \left(D_{ijkl} - D_{ijmn} \frac{\partial \chi^{kl}_m}{\partial y_n} \right) \Psi_{kl} \\ &= \left(D_{ijkl} - D_{ijmn} \frac{\partial \chi^{kl}_m}{\partial y_n} \right) \left(D^H_{klpq} \right)^{-1} \Sigma_{pq} \end{aligned} \tag{4.16}$$

where Ψ_{kl} denotes macroscopic strain and Σ_{pq} is macroscopic stress. Once the microscopic equation is solved, the microscopic stress in Eq. (4.16) can be calculated very easily for a variety of macroscopic stress conditions.

Based on Eq. (4.16), the generalization of this theory can be written in Eq. (4.17), which assures consistency between the microscopic and macroscopic behaviors of the trabecular bone model.

$$\boldsymbol{\Sigma} = < \boldsymbol{\sigma} > = < \boldsymbol{D} >< \boldsymbol{e} > = \boldsymbol{D^H \Psi} \tag{4.17}$$

where <> indicates the volumetric averaging operator.

4.4.1 Macroscopic load conditions

In homogenization theory, the RVE or unit cell (called as ROI in this study) represents an infinite number of cells in the macroscopic level. To maintain the periodicity for the whole domain, a uniform load with periodic boundary conditions was applied to this ROI. Therefore, in the static analysis, three compressive load cases were applied to the ROIs of trabecular bone microstructures as expressed in Eq. (4.18). The unidirectional uniform load was subjected to ROIs in left-right (axis-1), anterior-posterior (axis-2) and vertical (axis-3) axes for each case. Stress in Eq. (4.16) is then expressed by discretized form of finite element method, which can be written in vector form as follows:

$$\begin{aligned} \boldsymbol{\Sigma}^{(1)} &\equiv \left\{ \begin{array}{cccccc} -1 & 0 & 0 & 0 & 0 & 0 \end{array} \right\}^T \\ \boldsymbol{\Sigma}^{(2)} &\equiv \left\{ \begin{array}{cccccc} 0 & -1 & 0 & 0 & 0 & 0 \end{array} \right\}^T \\ \boldsymbol{\Sigma}^{(3)} &\equiv \left\{ \begin{array}{cccccc} 0 & 0 & -1 & 0 & 0 & 0 \end{array} \right\}^T \end{aligned} \tag{4.18}$$

4.4.2 Classification procedure

The aim of this method is to simplify the morphology of the complex trabecular bone microstructure into solely functional trabeculae. In order to present the procedures from a practical point of view, the following steps summarize the approach to this technique:

1. From the result of microscopic stress under unidirectional compression, the absolute values of maximum and minimum principal stresses for each voxel element are compared. The highest value is adopted as the microscopic principal stress for that element.

2. Voxel elements with higher microscopic stress than the average across the entire microstructure are considered as contributing to a main load path for that respective load direction.

3. Only these voxels are selected as working trabeculae. This concept is formulated in Eq. (4.17), which implies that, under certain constant microscopic strain, higher microscopic stress contributes to an increase in macroscopic stiffness.

4. By repeating steps 1 to 3 for each load case, the trabecular bone can then be classified by its respective load-bearing capabilities into eight groups, as illustrated by the Venn diagram in Fig. 4.6(a).

5. Next, the trabecular voxel elements are decomposed into three segments, depending on their response under the respective compressive load, as described in the following criteria:

   (a) *Primary trabeculae*: Working under vertical compression.

   (b) *Secondary trabeculae*: Working under horizontal (post-ant and left-right) loads only. Trabecular segments working under both horizontal and vertical compressions are included in *primary trabeculae*.

   (c) *Trabeculae of no contribution*: Lower microscopic stress than the average. It is easy to classify the trabecular segments from the Venn diagram, as shown in Fig. 4.6(b).

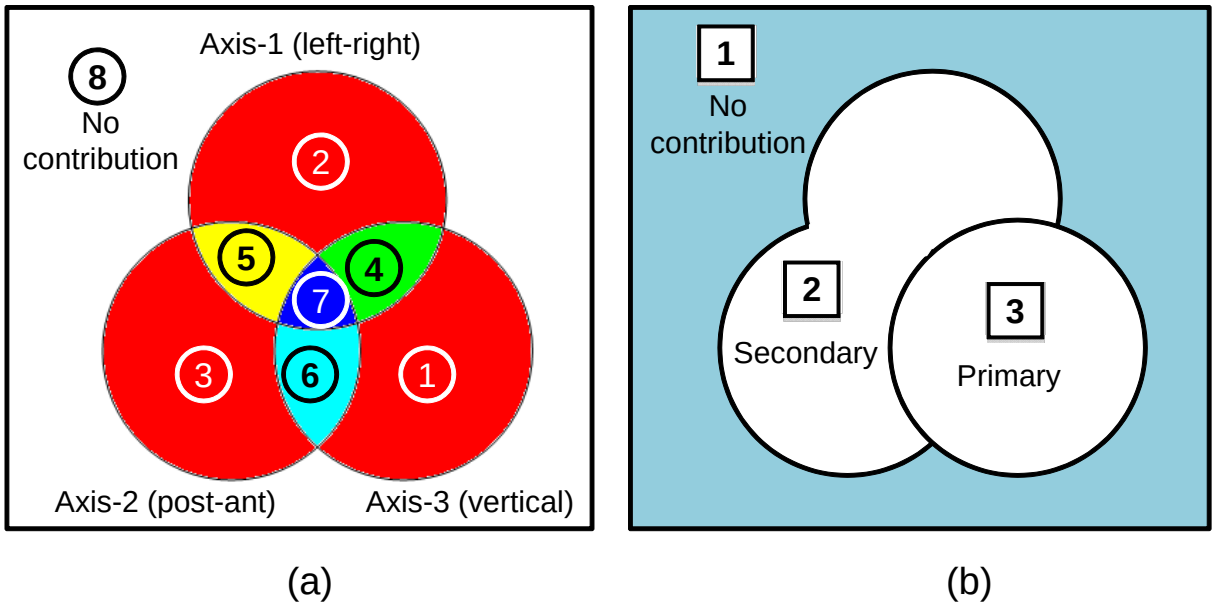

Figure 4.6: Classification of trabecular bone in a Venn diagram. (a) Eight groups; (b) Three segments.

4.5 Evaluation of microscopic stress

The principal microscopic stress response of trabecular bone under three compressive load cases is shown in Fig. 4.7 for ROI No. 8 and Fig. 4.8 for ROI No. 10. Stress under lateral compression (Fig. 4.7(a-b) and Fig. 4.8(a-b)) appeared to be higher than under vertical compression (Fig. 4.7(c) and Fig. 4.8(c)), because macroscopic strains are higher in lateral directions (axes 1 and 2) due to lower stiffness under this boundary condition, as presented in Table 4.1. Under compression in axis-2, the plate-like bone in ROI No. 8 was subjected to stress concentration, as shown in the blue contour. This specific plate-like bone was free from stress concentration under compressions in axes-1 and 3. The orientation of a plate-like surface was found to have contributed to this result.

Venn diagrams expressing the classification of trabecular bone response are shown in

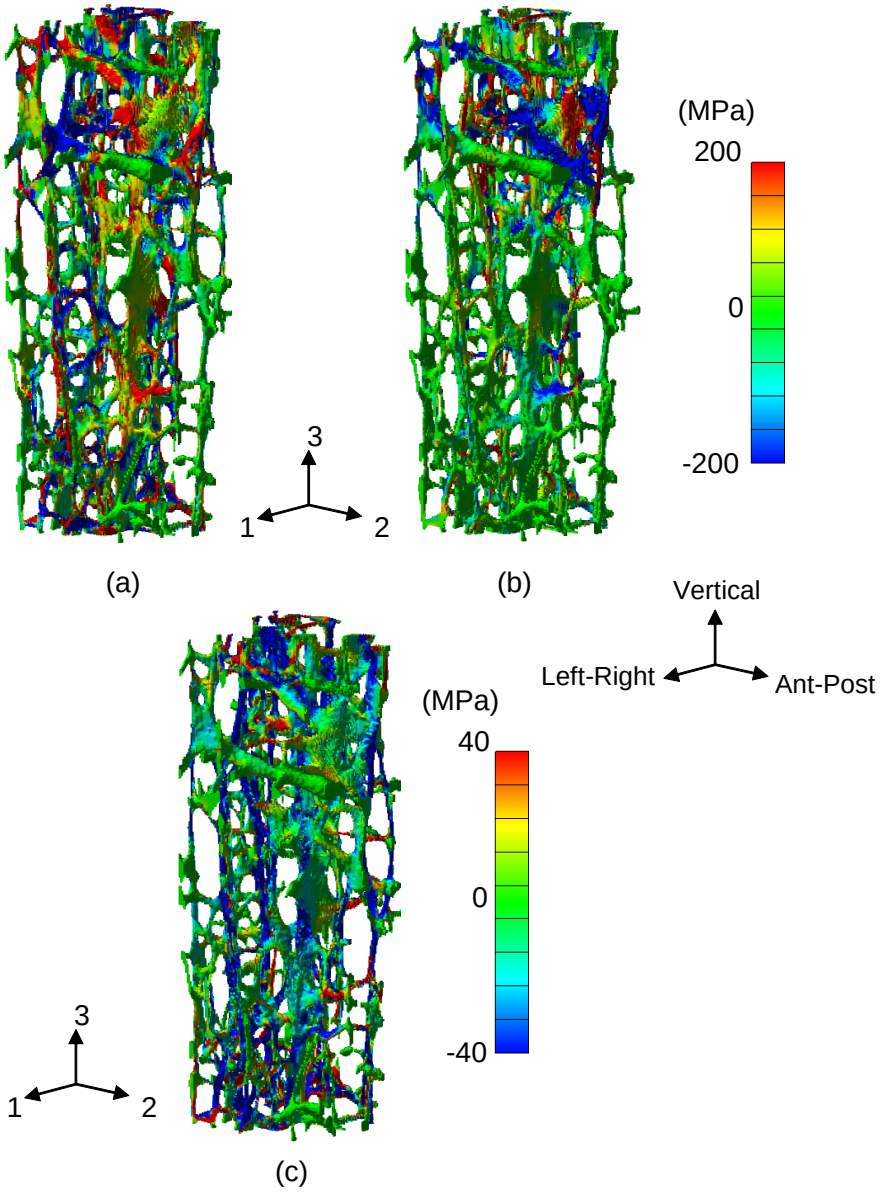

Figure 4.7: Principal stress contour for ROI No. 8: (a) under axis-1 compression; (b) under axis-2 compression; (c) under axis-3 compression.

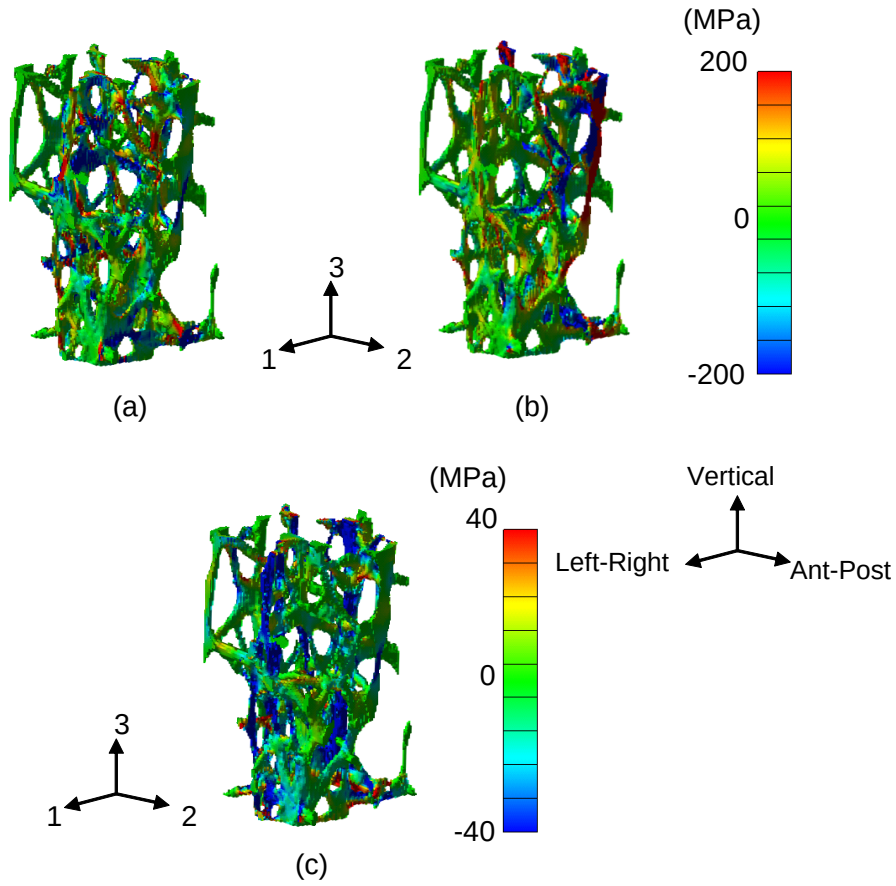

Figure 4.8: Principal stress contour for ROI No. 10: (a) under axis-1 compression; (b) under axis-2 compression; (c) under axis-3 compression.

Figs. 4.9 and 4.10 for the selected ROIs of healthy (Nos. 1, 2 and 4) and osteoporotic (Nos. 6, 8 and 10) cases, respectively. Among three healthy bone ROIs, percentages in the Venn diagrams were similar for ROI No. 1 (large ROI) and ROI No. 2 (plate-like trabeculae-rich). About 50% of trabecular bone was found responded to vertical compressive load for ROI No. 1 and No. 2. However, for ROI No. 4 (rod-like trabeculae-rich), the percentage under vertical compressive load was lower than the others. The overall behavior was close to that in the plate-like trabeculae-rich region, but the rod-like trabeculae-rich region near the inter-vertebral discs showed different mechanical responses. In the case of the osteoporotic bone, the percentage under vertical compressive load for all ROIs was lower than for the healthy case, which is only about 1/3. Also, under-loading in axis-1 was slightly lower than in axis-2, which corresponds to the apparent elastic moduli shown in Table 4.1.

4.6 Classified trabeculae structures

The present classification method was visualized in Fig. 4.11 for the large ROI No.1 and in Fig. 4.12 for ROI No. 6, which are healthy and osteoporotic bones, respectively. In Fig. 4.11(c) and Fig. 4.12(c), trabeculae working as main load paths under vertical compressive load are highlighted. As is more clearly seen in the magnified view of a certain portion, they are supposed to be the so-called primary trabecular bone. Here, the maximum principal stress vector in red always has a positive value, while the minimum principal stress vector has a blue negative value. Note again, eigen vectors of stress tensor in this thesis is called principal stress vector. Compared to the original models (Figs. 4.11(a) and 4.12(a)), the complicated trabecular architecture has been successfully simplified and the

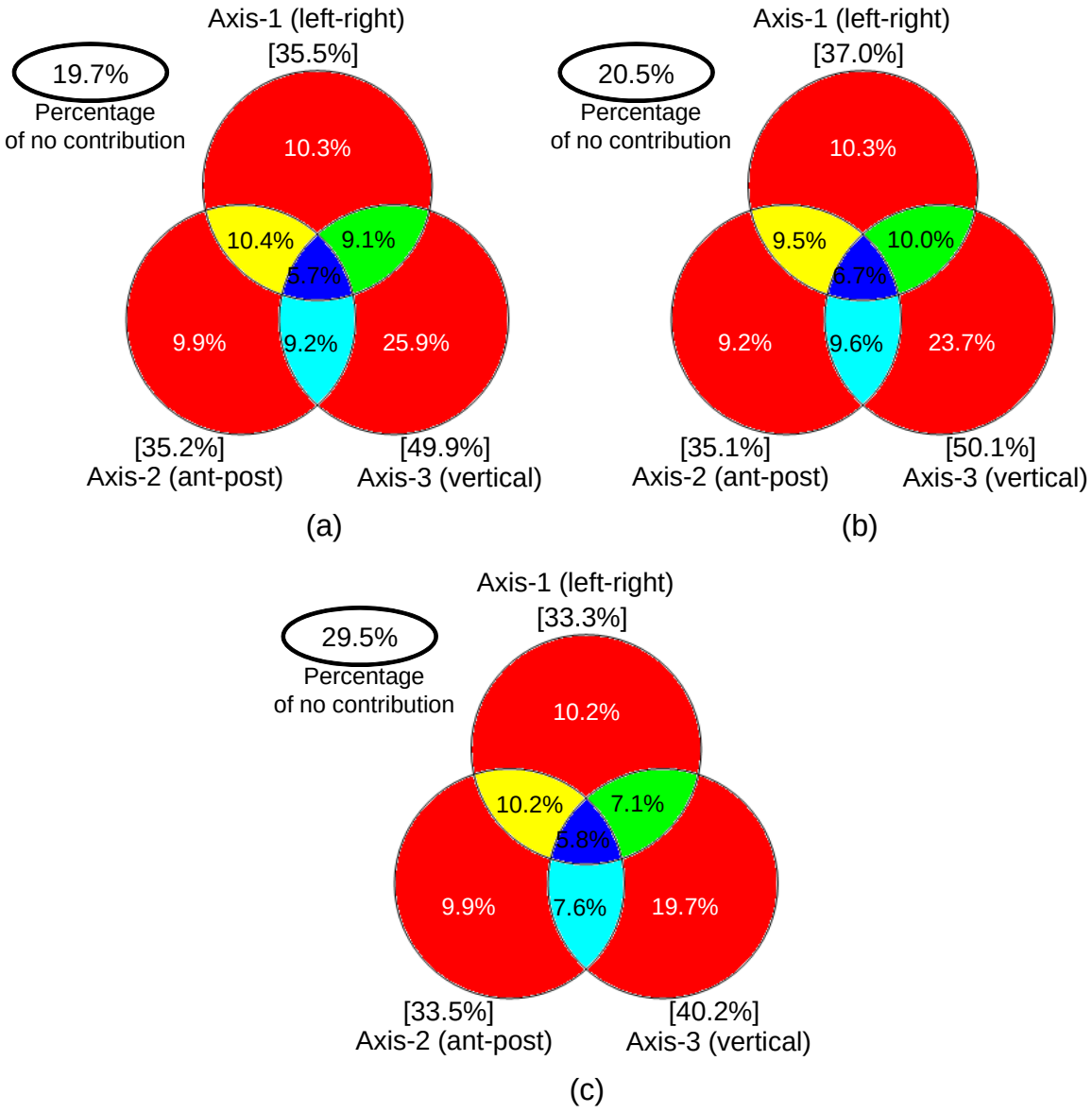

Figure 4.9: Classification of trabecular bone response for: (a) ROI No. 1, (b) ROI No. 2, and (c) ROI No. 4. [ ] corresponds to trabecular voxel percentage and the accumulation of percentages in Venn diagram subsets in respective compression directions (as indicated in axis names). The functional ability of each trabecular voxel is identified by specific colors.

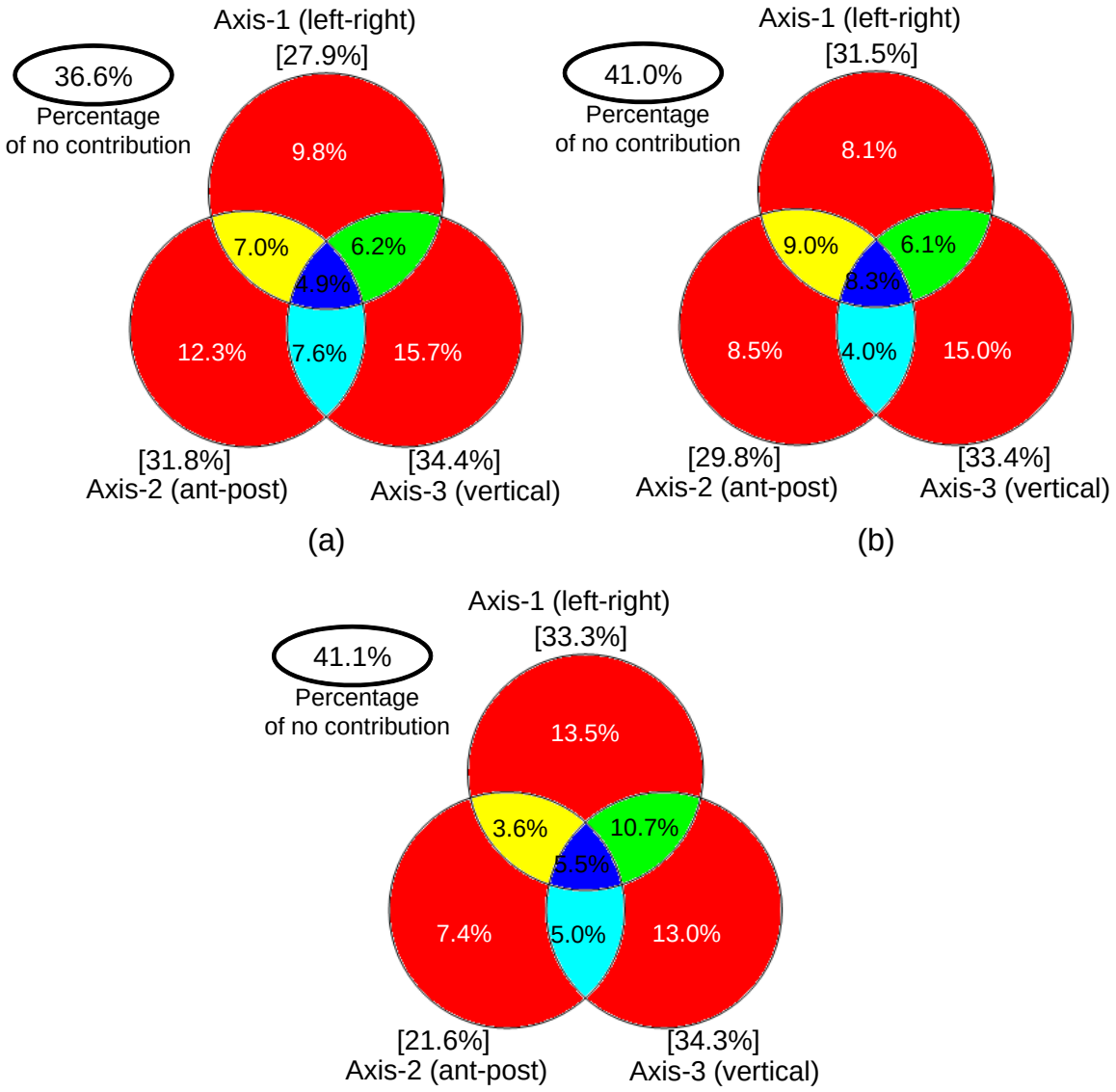

Figure 4.10: Classification of trabecular bone response for: (a) ROI No. 6, (b) ROI No. 8, and (c) ROI No. 10.

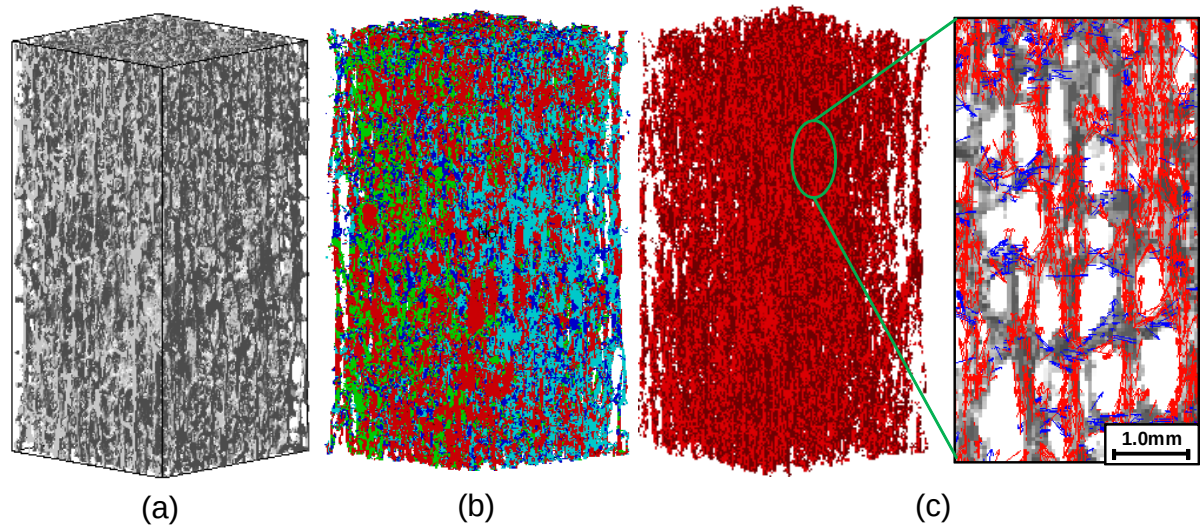

Figure 4.11: Classified trabecular under compression in axis-3 and a highlighted view of the primary trabeculae for ROI No. 1. (a) Original model. (b) Classified trabecular. (c) Primary trabeculae.

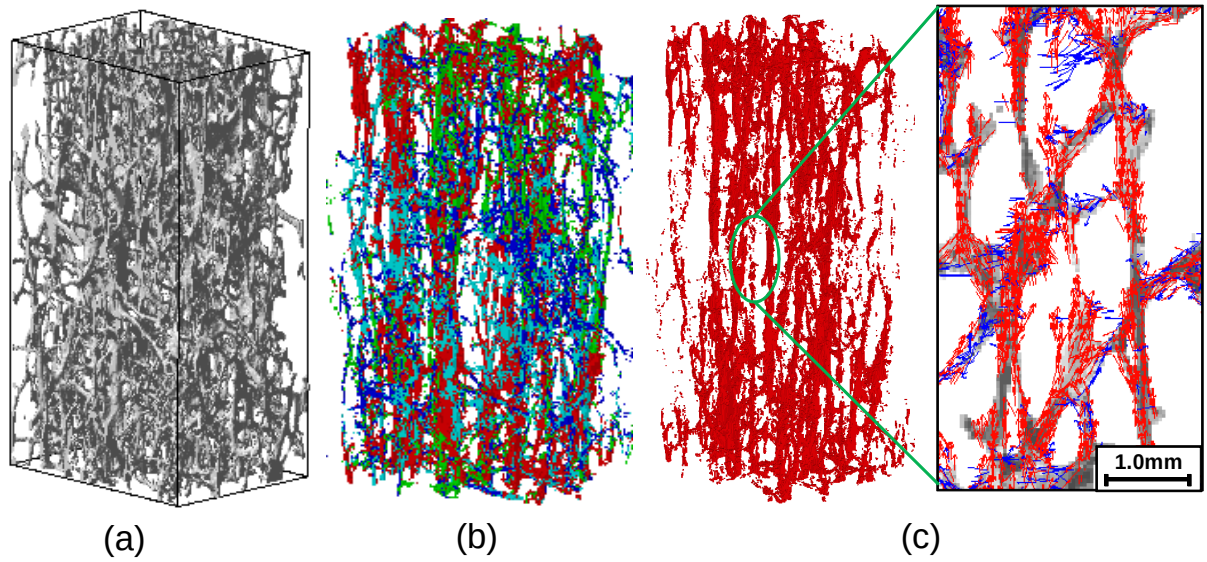

Figure 4.12: Classified trabecular under compression in axis-3 and a highlighted view of the primary trabeculae for ROI No. 6. (a) Original model. (b) Classified trabecular. (c) Primary trabeculae.

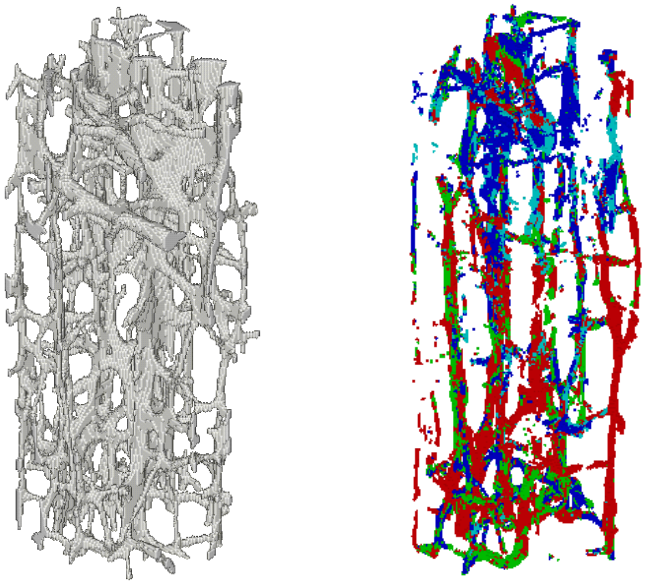

Figure 4.13: Contour of classified trabecular segments for ROI No. 8 of (a) original model and (b) primary trabeculae.

mechanical role of the primary trabecular under three axes of compression is visualized in contour.

Moreover, Figs. 4.13 and 4.14 display the contours of the segments classified as primary trabeculae for ROIs No. 8 and 10, in which the four colors correspond to the working trabeculae under vertical compression shown in the Venn diagram. It seems that the orientation of primary trabecular bone is almost vertical.

On the other hand, Fig. 4.15 shows the classified results under non-vertical load cases for ROI No. 1. They are totally different from Figs. 4.11 and 4.12. Careful observation through a magnified view, which is typically shown in Fig. 4.15, tells us that the secondary trabecular bone is highlighted successfully—the primary and secondary trabeculae bones are highlighted in a very complex trabecular microarchitecture. The

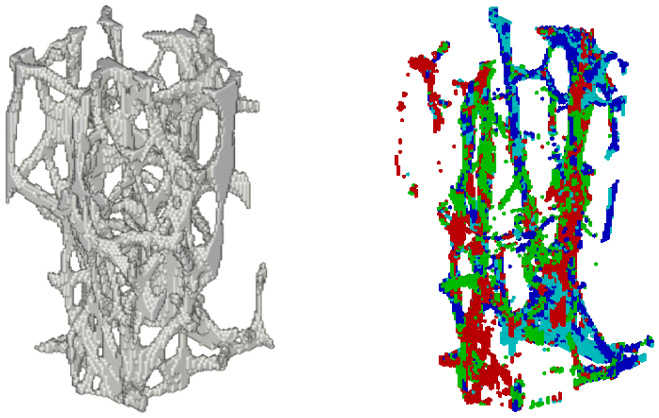

Figure 4.14: Contour of classified trabecular segments for ROI No. 10 of (a) original model and (b) primary trabeculae.

Venn diagram in Fig. 4.9 implies that the primary bone mainly supports self-weight, but half of it also works under compressive loads in the left-right and post-ant directions. The secondary bone can be visualized as the load path used only for loading in left-right or post-ant directions. However, the secondary bone was used as part of the load path network for all loading cases. The comparison between the apparent elastic moduli of healthy bones and osteoporotic bone implies that the secondary bone is dramatically decreased in the osteoporotic bone.

Figure 4.16(b-d) shows the 3D microstructure of the osteoporotic bone which was classified into primary trabecular, secondary trabecular and no contribution trabecular sections, respectively. Obviously, different trabecular microarchitecture behaviors were seen for each segment. The orientation of the primary trabecular was almost in a vertical direction, and most of the secondary trabecular was seen in a lateral direction. Compared to the original microstructure in Fig. 4.16(a), the complicated trabecular microarchitec-

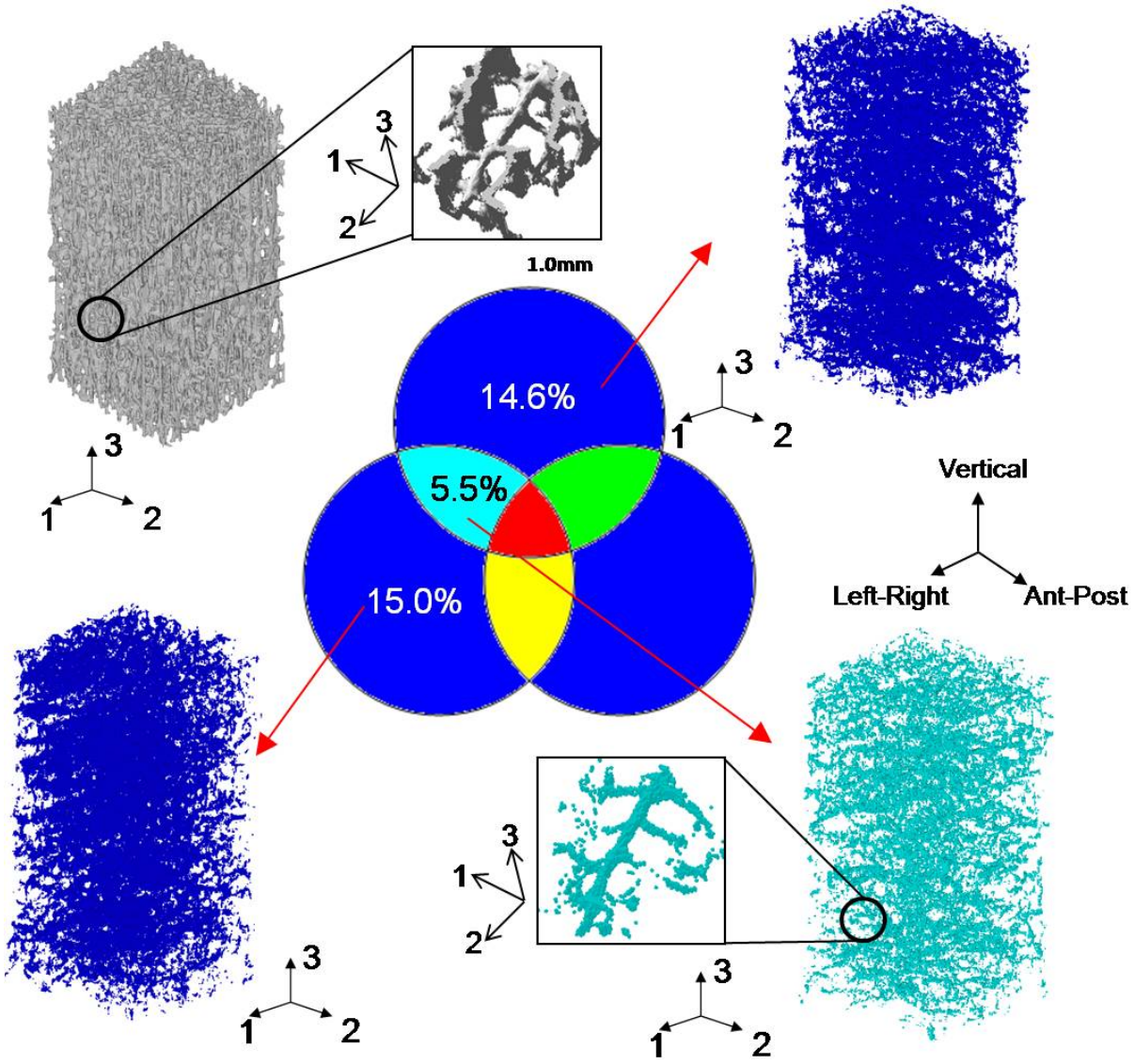

Figure 4.15: Highlighted view of a secondary trabecular in healthy bone (ROI No. 1).

ture was classified from a mechanical point of view. The majority of the trabecular (36.6%) was found to make no significant contribution to the load path, and about one-third of the trabecular responded to vertical loading. The percentage of secondary trabecular corresponding to the contributed element in a solely lateral direction was 29%. Conversely, the primary trabecular (49.9%) was dominant, whereas only about 20% of the no contribution trabecular was found in the healthy bone case, as shown in Fig. 4.17. About 30% of the secondary trabecular contributed to the load path. This result suggests that in healthy bone most of the elements in the microstructure respond well and contribute to load distribution efficiently. Hence, the numbers of trabeculae subjected to stress concentration in healthy bone were lower than that for the osteoporotic bone, which resulted in a higher fracture risk for the osteoporotic bone. Although the selected ROI are high in density, the orientation of the trabecular struts was distinguished easily from among all the classified trabeculae.

4.7 Role of trabecular types

The apparent Young's moduli for ROI No. 2 were higher than for ROIs No. 3 and No. 4, because bone density was high due to the existence of a plate-like bone-rich region, whereas No. 3 and No. 4 were lower because they consist of rod-like bone-rich region. The overall characteristics of trabecular bone in vertebrae are expressed by the large ROI model No. 1. The above numerical results imply that the plate-like rich region dominates the overall characteristics of trabecular bone, i.e. plate-like bone exerts a substantial influence on the mechanical responses of trabecular bone.

The plate-like trabecular bone included in ROI No. 2 is shown in Fig. 4.18(a).

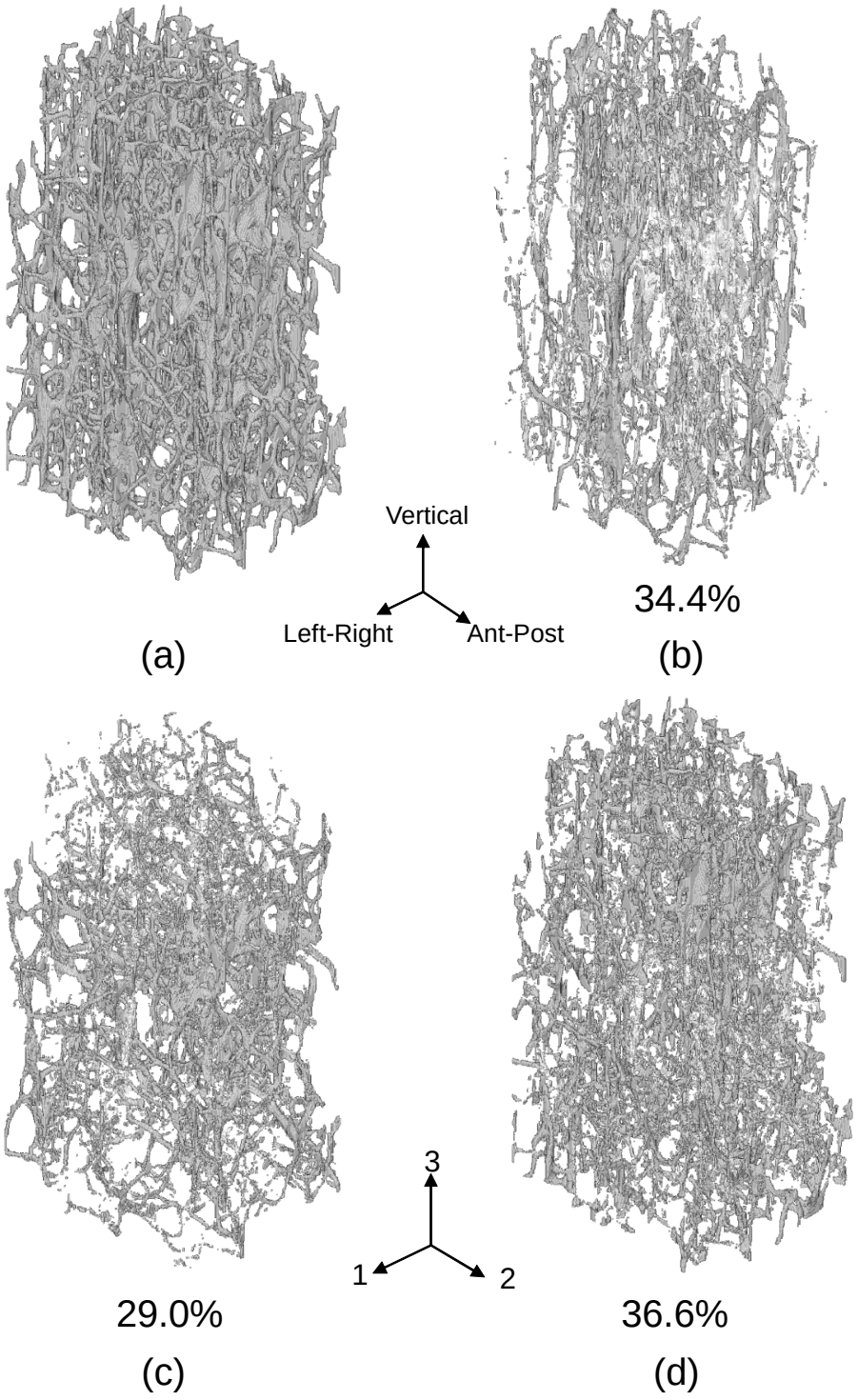

Figure 4.16: Classification of a 3D microstructure of osteoporotic bone (ROI No. 6). (a) Original microstructure, (b) primary trabecular, (c) secondary trabecular and (d) no contribution trabecular.

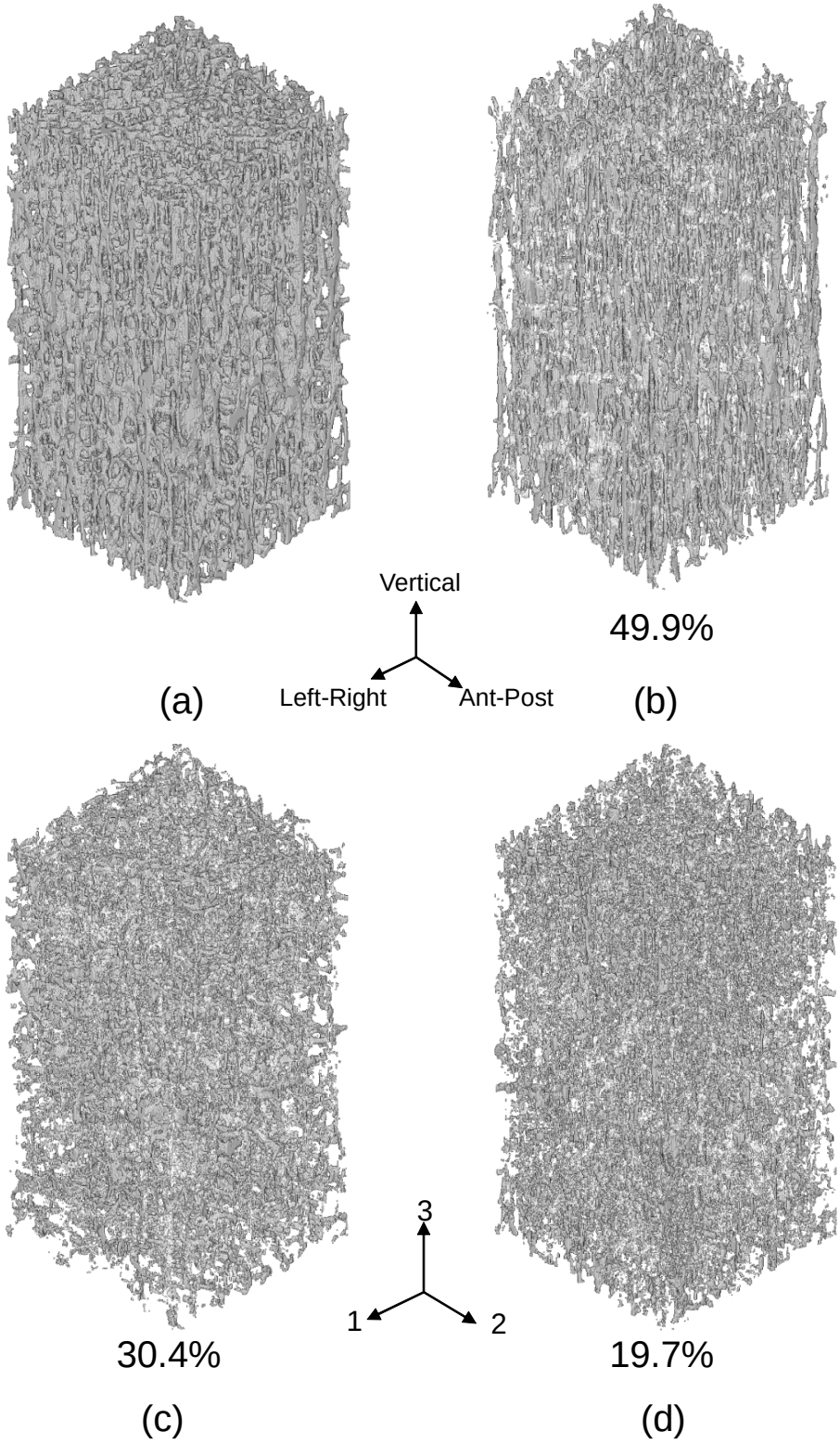

Figure 4.17: Classification of a 3D microstructure of healthy bone (ROI No. 1). (a) Original microstructure, (b) primary trabecular, (c) secondary trabecular and (d) no contribution trabecular.

Classification of the mechanical role is visualized in Fig. 4.18(b-d). The yellow part represents typical plate-like bone, which supports loads in the vertical and post-ant directions only, due to its orientation. The simplified morphology of ROI No.2, consisting of plate-like trabecular bone and connecting rod-like trabecular bones, and the load path transmissions are illustrated in Fig. 4.18(e). Suppose that the plate-like trabecular bone is subjected to a compressive load in axis-3, as indicated by the black double-ended arrows. The load exerted onto the plate-like bone is transmitted not only to the connecting rod-like bone in axis-3 but also to the connecting rod-like bones in axis-2, as displayed by the black single-ended arrows. A similar pattern of load path transmission occurs when loads are applied in axis-2, as displayed by the brown double-ended arrows, where it can be seen that part of the applied load is transmitted to axis-3, as illustrated by the brown single-ended arrows.

Plate-like trabecular bone, its area and the number of connected rod-like bones decrease in osteoporotic bone, which consequently increases the risk of fracture. A decrease in bone density leads to stress concentration in rod-like trabecular bone. Comparing Figs. 4.11(c) and 4.12(c), the length of the secondary bone, in other words, the distance between the primary bones, is greater for osteoporotic bone than for healthy bone. This may also lead to stress concentration in the secondary bone. Together with stress concentration, any loss of plate-like bone is supposed to raise the fracture risk of osteoporotic trabecular bone.

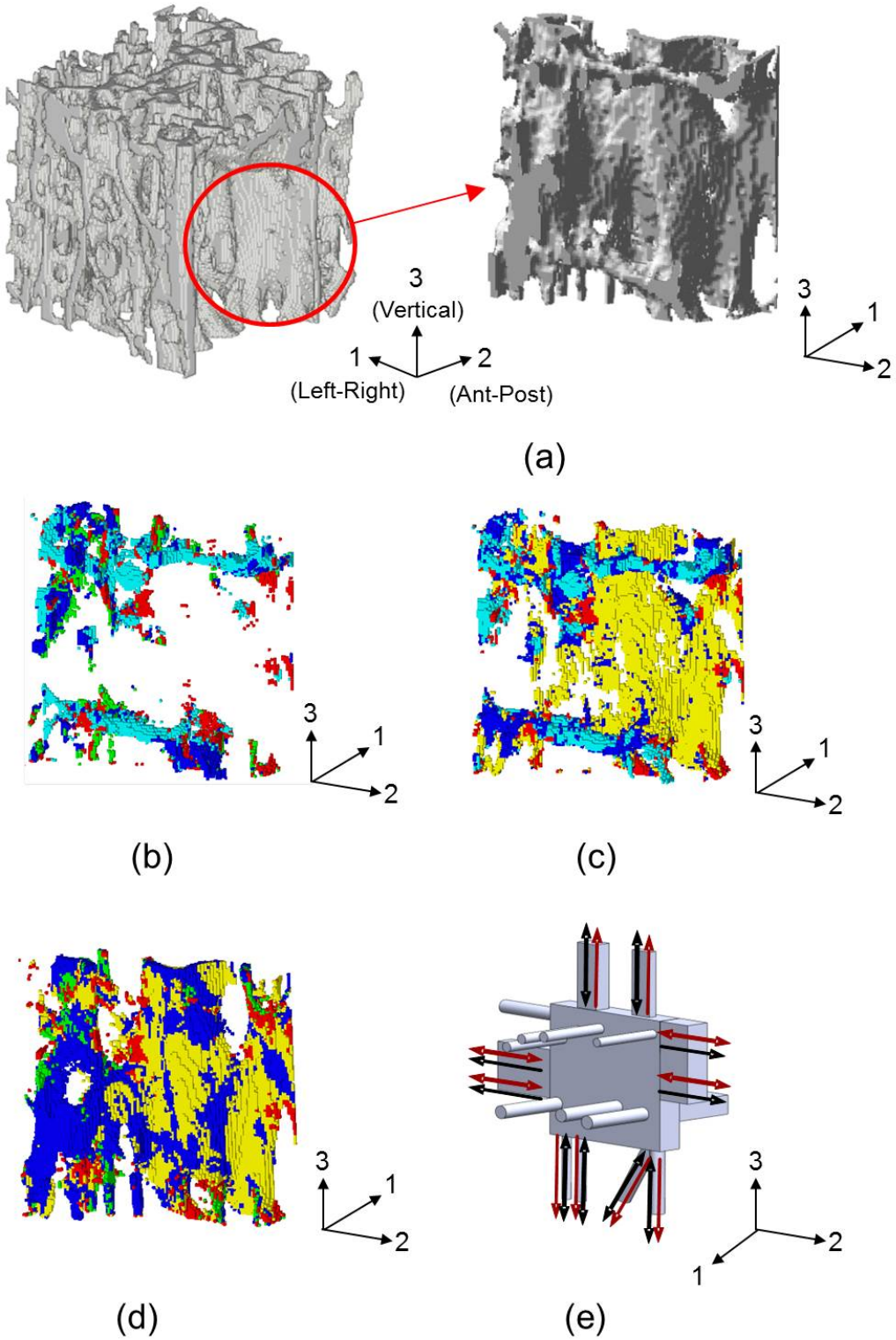

Figure 4.18: Classification of the mechanical role of plate-like trabecular bone in ROI No. 2. (a) ROI No. 2 and a magnified view of plate-like bone; (b) compression in axis-1; (c) compression in axis-2; (d) compression in axis-3, and (e) an illustration of the load path.

4.8 Summary

Homogenization and finite element methods were used to analyze microscopic trabecular bone in a human lumbar vertebra. The calculated apparent elastic moduli of healthy and osteoporotic bones were examined by focusing on the effect of trabecular morphology. A comparison of the calculated apparent Young's modulus with Keyak et al.'s experimental results showed good agreement. Trabecular morphology was found to contribute to bone stiffness as well as bone density. Following on from this analysis, a new classification method was proposed, in order to study the morphology and mechanical role of trabecular bone. The otherwise complicated trabecular was successfully simplified and classified from a mechanical point of view. Primary and secondary trabecular bones with load-bearing capability were visualized clearly, as a mechanical response against three macroscopic loading conditions. The characteristics of plate-like bone were described by relating the load path to the network architecture under static analysis. However, morphology analysis needs to be investigated further under dynamic loading, in order to enhance our understanding of morphology characteristics and the role of individual trabecular bones on load-bearing distribution in the trabecular network.

Chapter 5

Morphology analysis using dynamic FEM

5.1 Introduction

Computational analysis of trabecular bone under dynamic loading conditions is tough and costly, especially in image-based modeling, where the size of an element should be small and the number of elements is extremely large. It is hard to determine the mechanical response of specific nodes or elements in a large-scale and geometrically complex finite element model, since assigning particular target nodes or elements before analysis, which is common practice in structural analyses in mechanical design, is almost impossible. With additions to the complex morphology of the microstructure, visibility in the trabecular model is reduced. Furthermore, performing dynamic analysis on a trabecular microstructure requires a huge number of time steps, as a result generating a massive number of output files so that the selection of appropriate output data becomes difficult.

Accompanying the complicated trabecular network, an investigation of the morphology and mechanical responses of trabecular microstructures under dynamic loading is a challenging task.

Numerical assessments of trabecular bone morphology under dynamic loading have been conducted in a variety of studies. Kameo *et al.* (2011) simulated morphological changes in a three-dimensional trabecular under cyclic uniaxial loading with various frequencies, in order to study the effect of loading frequency as a significant mechanical factor in bone remodeling. The results of the simulation showed that trabeculae reoriented to the loading direction as bone remodeling progressed. Liu *et al.* (2008a) performed a dynamic simulation of bone remodeling processes, to evaluate the contributions of different microstructural bone loss mechanisms to the morphological and mechanical properties of human trabecular bone during menopause. The results suggested that the perforation of plate-like bone played a far more important role than other mechanisms in bone loss. Both studies confirm the importance of dynamic analysis in understanding the morphological changes of trabecular bone. Dynamic analyses in the context of ultrasound propagation have also been used to study the morphology of trabecular bone (Padilla *et al.*, 2006; Haïat *et al.*, 2007; Hosokawa, 2008, 2011). Padilla *et al.* (2006), for instance, performed a numerical simulation of wave propagation. Their results suggest that the morphological properties of the trabecular structure are the major determinants of wave propagation through this type of bone, and they also found that the main orientation of the trabecular network is consistently perpendicular to the direction of propagation.

Therefore, this chapter aims to describe the specific trabecular bone morphology that focuses on the role of trabecular networks and types (plate-like and rod-like) of load-bearing capability under dynamic loading. A new classification method, using asymptotic

homogenization theory, which is similar to the one in the previous chapter, is introduced to simplify the visualization of the trabecular network. In this approach, trabecular bone was separated into three segments—primary, secondary, and no contribution—based on the mechanical stress response under uniaxial compression in the left-right, anterior-posterior, and vertical directions. Once the trabecular classification was carried out, the morphological behavior of the trabecular bone could be investigated by viewing the propagation of load pathways in the selected trabecular bone segments under dynamic loading.

The classification or decomposition method used for trabecular bone structure has been introduced previously by using an advanced image processing technique based on a line skeleton graph (Pothuaud *et al.*, 2000, 2002) and volumetric extent (Stauber and Müller, 2006; Liu *et al.*, 2008b). The major difference between the approaches in these studies and ours is that the decomposition of the trabecular bone was actioned in a continuity portion rather than by individual trabecular type, so that the morphology study based on mechanical load transfer could be observed from the view point of a network system. The hierarchical approach to morphology analysis under dynamic loading is shown in Fig. 5.1. The approach of the present study in this respect is structured into three parts. The first part looks at the modeling process, which involves image-based modeling techniques with the appropriate selection of regions of interest (ROIs). The second part presents the algorithm for classifying trabecular bone into primary, secondary, and no contribution by using an asymptotic homogenization method. The first part has already been discussed in Chapter 3, whereas the second part was implemented in Chapter 4 and will be discussed further in this chapter. However, in this chapter, we focus on describing the application of dynamic analysis to the selected trabecular volumes.

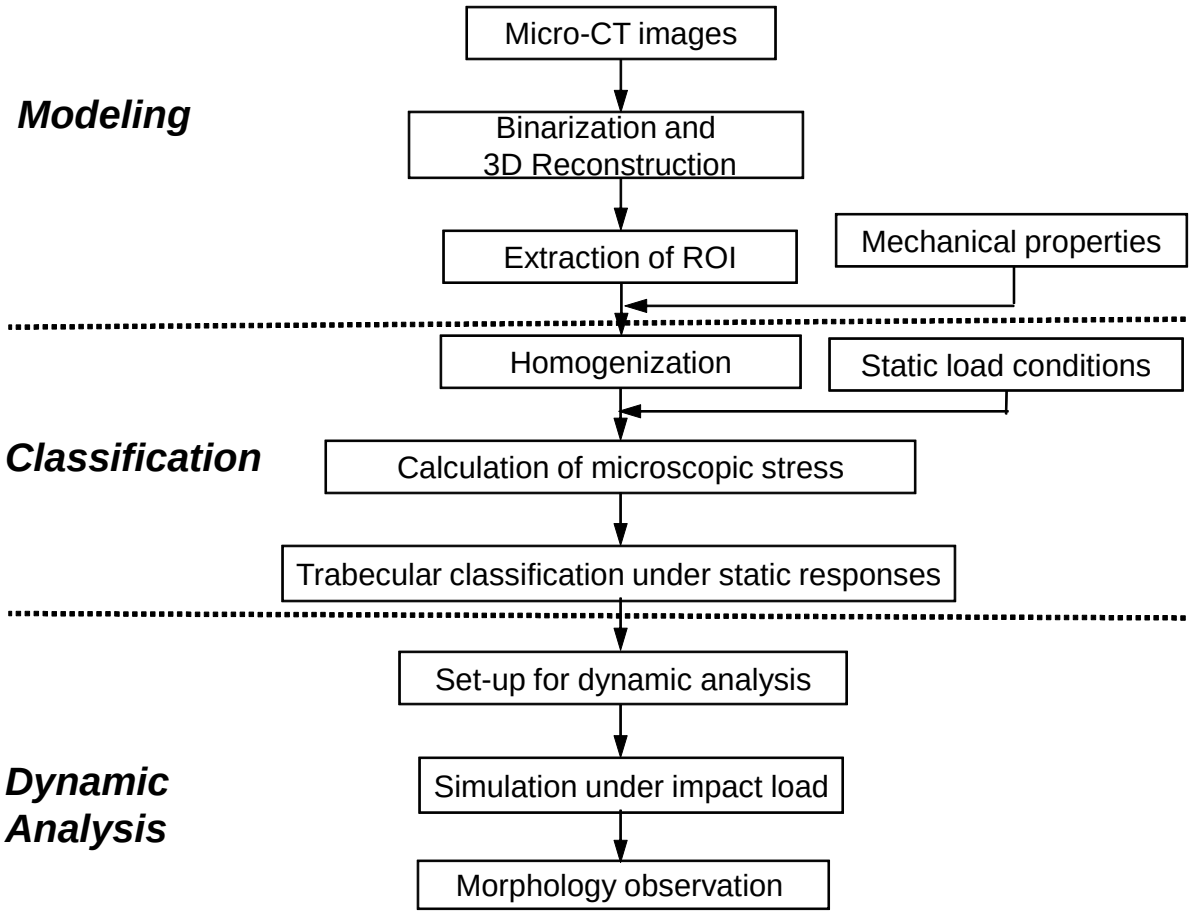

Figure 5.1: Hierarchical approach to morphology analysis under dynamic loading.

5.2 Modification of classification method

In order to improve the visualization of segmented trabeculae structures for large ROIs, the classification method described in Chapter 4 is updated in this chapter. In this method, only the inner part of the ROI is selected for visualization in the dynamic analysis. The procedure for this method, which is presented in the flow chart in Fig. 5.2, can be summarized in the following steps.

1. Select the large size ROI Y with $X_{ROI} \times Y_{ROI} \times Z_{ROI}$ dimensions, as shown in Fig. 5.3. Let the coordinate of each element in the ROI be written in the following equation:

$$(x, y, z) \in Y \equiv \left(\left[-\frac{X_{ROI}}{2}, \frac{X_{ROI}}{2} \right], \left[-\frac{Y_{ROI}}{2}, \frac{Y_{ROI}}{2} \right], \left[-\frac{Z_{ROI}}{2}, \frac{Z_{ROI}}{2} \right] \right) \tag{5.1}$$

   The ROI has N number of elements with volume $|Y|$.

2. Apply compressive macroscopic stress sequentially to the selected ROI in orthogonal directions, as shown in Fig. 5.3 and indicated as $\Sigma_{11} = -1, \Sigma_{22} = -1$ and $\Sigma_{33} = -1$. Axes-1 and 2 correspond to the lateral axis (left-right and post-ant), whereas axis-3 is in the vertical axis.

3. Calculate the minimum principal stress response for each voxel element i under three load cases and define them as $\left(\sigma_3^{(11)}\right)_i$, $\left(\sigma_3^{(22)}\right)_i$ and $\left(\sigma_3^{(33)}\right)_i$. The superscript denotes the loading direction.

4. Define the inner part of the ROI. The coordinate for the selected inner ROI Y_{in} is

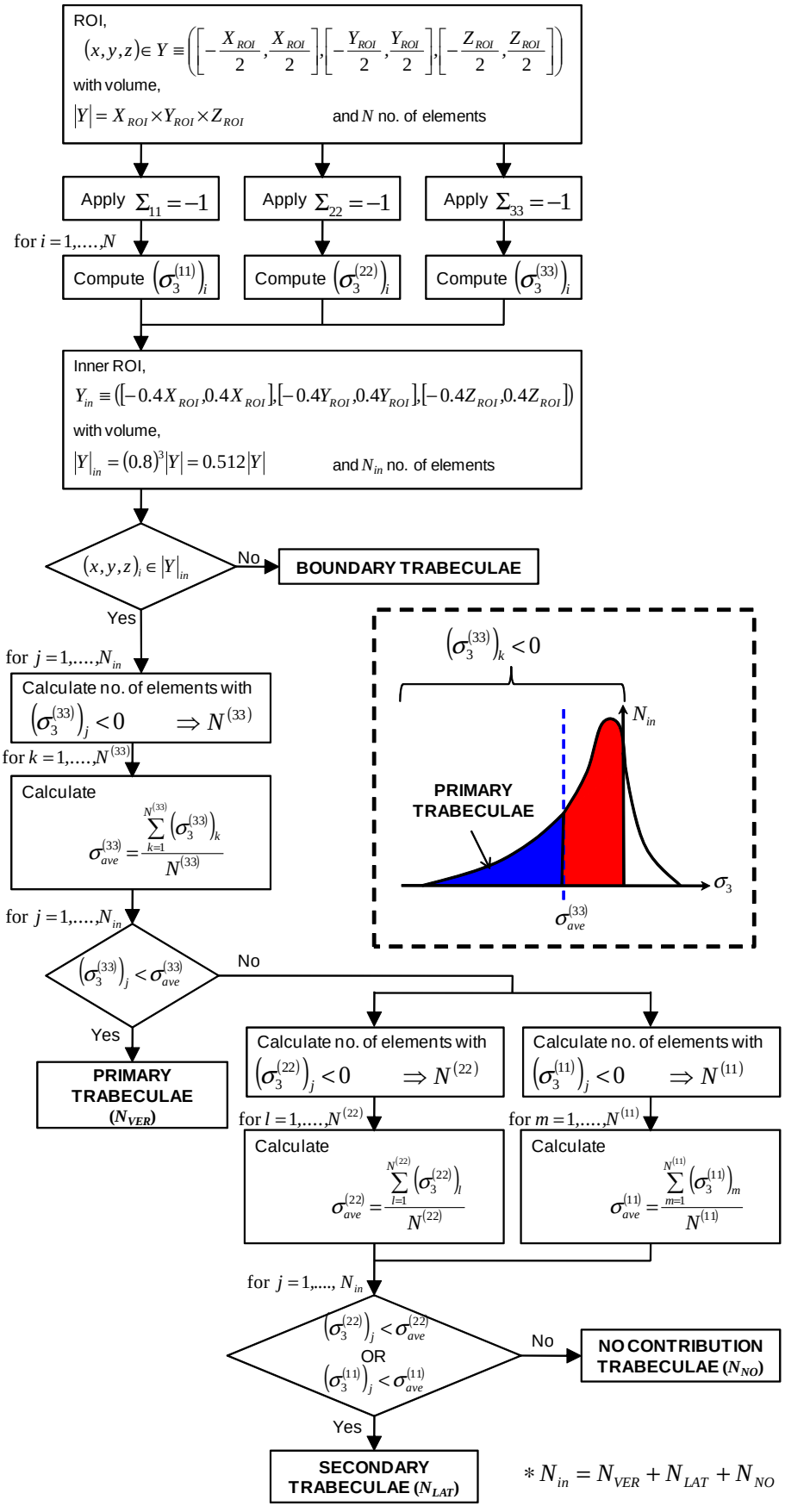

Figure 5.2: Flow diagram of the classification method.

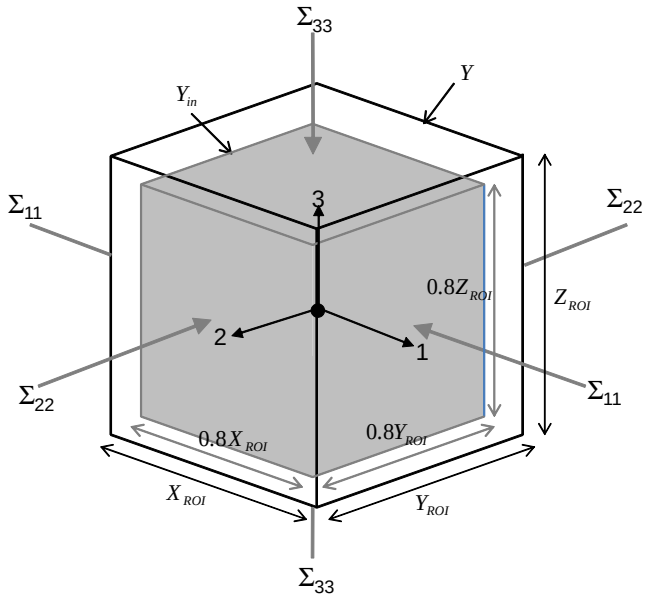

Figure 5.3: Indices of ROI in the classification method.

written as follows (Takano *et al.*, 2003), with N_{in} number of elements:

$$Y_{in} \equiv \left(\left[-0.4X_{ROI}, 0.4X_{ROI} \right], \left[-0.4Y_{ROI}, 0.4Y_{ROI} \right], \left[-0.4Z_{ROI}, 0.4Z_{ROI} \right] \right) \quad (5.2)$$

The volume of the inner ROI is then can be calculated as follows:

$$|Y_{in}| = (0.8)^3 |Y| = 0.512|Y| \quad (5.3)$$

5. Select the elements that are located in the inner part region, as expressed in Eq. (5.4), and classify those elements outside of the region as boundary trabeculae.

$$(x, y, z) \in |Y_{in}| \ \ (j = 1, \ldots, N) \quad (5.4)$$

6. Under vertical load condition, select elements j (in Y_{in}) with the minimum principal

stress (in compression) that is below than zero, as expressed in Eq. (5.5). The total number of elements under this condition is denoted as $N^{(33)}$.

$$\left(\sigma_3^{(33)}\right)_j < 0 \;\; (j = 1, \ldots, N_{in}) \tag{5.5}$$

7. Average out the minimum principal stress in compression under a vertical load case, calculated as follows:

$$\sigma_{ave}^{(33)} = \frac{\sum_{k=1}^{N^{(33)}} \left(\sigma_3^{(33)}\right)_k}{N^{(33)}} \quad \left(k = 1, \ldots, N^{(33)}\right) \tag{5.6}$$

where k is kth element number with the minimum principal stress in compression under a vertical load case.

8. Select the jth elements with lower compressive minimum principal stress than the average, as written in Eq. (5.7) and classify as primary trabeculae (N_{VER}). This classification process is illustrated in the dotted line box of Fig. 5.2.

$$\left(\sigma_3^{(33)}\right)_j < \sigma_{ave}^{(33)} \;\; (j = 1, \ldots, N_{in}) \tag{5.7}$$

9. Repeat steps 6 to 7 for the remaining elements in Y_{in} for the two other load cases (11) and (22). Select the jth elements that meet the requirements as written in either Eqs. (5.8) or (5.9), and then classify as secondary trabeculae (N_{LAT}).

$$\left(\sigma_3^{(11)}\right)_j < \sigma_{ave}^{(11)} \;\; (j = 1, \ldots, N_{in}) \tag{5.8}$$

$$\left(\sigma_3^{(22)}\right)_j < \sigma_{ave}^{(22)} \;\; (j = 1, \ldots, N_{in}) \tag{5.9}$$

10. Finally, the remaining elements in Y_{in}, which are not classified in steps 8 and 9, are then classify as no contribution trabeculae (N_{NO}). Hence, the total number of elements in the inner ROI can be written as follows:

$$N_{in} = N_{VER} + N_{LAT} + N_{NO} \tag{5.10}$$

5.3 Dynamic explicit FEM

The established ROI models and mechanical properties were used to perform the dynamic analysis. A dynamic explicit finite element method with a lumped mass matrix setup was used to analyze the transient response of the trabecular bone microstructure under impact loading. Using the explicit method, the dynamic analysis can be accelerated, but the following Courant, Friedrichs and Lewy (CFL) condition (Lewy *et al.*, 1967) must be met, in order to stabilize time integration:

$$\Delta t < \frac{l}{c_v} \tag{5.11}$$

where Δt is the interval time step, l denotes the minimum distance between voxel element nodes, and c_v is the velocity of the stress wave. This dynamic analysis used VOXEL-CON2011 commercial software (Quint Corp., Tokyo, Japan), which takes into account the value of the shear modulus G when calculating longitudinal wave velocity, as shown in the following formula:

$$c_v = \sqrt{\frac{\dfrac{E}{3(1-2v)} + \dfrac{4}{3}G}{\rho}} \tag{5.12}$$

E denotes Young's modulus and ρ stands for density. A density of 1.94×10^{-6} kg/mm^3 was chosen (Guo, 2001), and the time step interval for dynamic loading was set as 6.0×10^{-9} s, in order to meet time integration stability.

Since the trabecular bone microstructure extracted here is considered an infinite medium, a special viscous boundary (Lysmer and Kuhlemeyer, 1969; Kuhlemeyer and Lysmer, 1973), also called an infinite boundary treatment, was applied to avoid a wave reflection problem at the boundary. By setting the element boundary nodes with spring elements, in order to absorb the reflection of the stress wave, discontinuity at the boundary can be eliminated.

It is easy to handle the time-domain analysis using a viscous boundary, because it does not require an additional degree of freedom. The damping force $\boldsymbol{f_d}$, subjected to each node on the boundary surface, was set as:

$$\boldsymbol{f_d} = \frac{A\rho}{4} \begin{bmatrix} V_P & 0 & 0 \\ 0 & V_S & 0 \\ 0 & 0 & V_S \end{bmatrix} \begin{Bmatrix} \gamma_x \\ \gamma_y \\ \gamma_z \end{Bmatrix} \tag{5.13}$$

where A stands for area of the voxel, γ the vector of velocity in each direction, and V_P and V_S the velocities of the P and S waves, respectively, which are expressed by (Lysmer and Kuhlemeyer, 1969):

$$V_P = \sqrt{\frac{E(1-v)}{(1+v)(1-2v)\rho}} \tag{5.14}$$

and

$$V_S = V_P\sqrt{\frac{(1-2v)}{2(1-2v)}} \tag{5.15}$$

The viscous boundary condition was set for four side surfaces of the ROI. The bottom

surface of the ROI was fixed, while the top surface was subjected to the following force impulse F with a short time period t:

$$F(t) = -2 \text{ N for } 0 \leq t \leq 1.0 \times 10^{-5} \text{ s} \tag{5.16}$$

It is difficult to observe the trabecular bone response in a complex microarchitecture under dynamic analysis, especially in terms of visibility. Therefore, by using the classification of trabecular bone determined in the homogenization analysis, dynamic responses can be investigated separately in the primary, secondary, and no contribution trabecular segments, following which the propagation of stress wave behavior in each trabecular segment can be viewed in detail.

5.4 Percolation of load transfer

The principal stress distribution for ROI No. 8 under dynamic loading at time steps 2.5, 3.5, 4.5, and 5.5×10^{-6} s, and a comparison with the original model size is shown in Fig. 5.4. High stress is seen in the plate-like trabecular bone in Fig. 5.4(b), while Fig. 5.4(c) shows stress in the extracted primary trabecular bone. Here, the hidden trabecular bone is shown to act as a pathway for the stress wave. Note that the above-mentioned plate-like bone was removed. It seems that the orientation of plate-like trabecular bone is not aligned with axial load direction, and penetration of the stress wave is concentrated only in the center of the trabecular network.

In the same manner, the dynamic response of ROI No. 10 is displayed in Fig. 5.5 at time steps 1.5, 2.0, 2.5, and 3.0×10^{-6} s. In Fig. 5.5 (b), the stress wave is

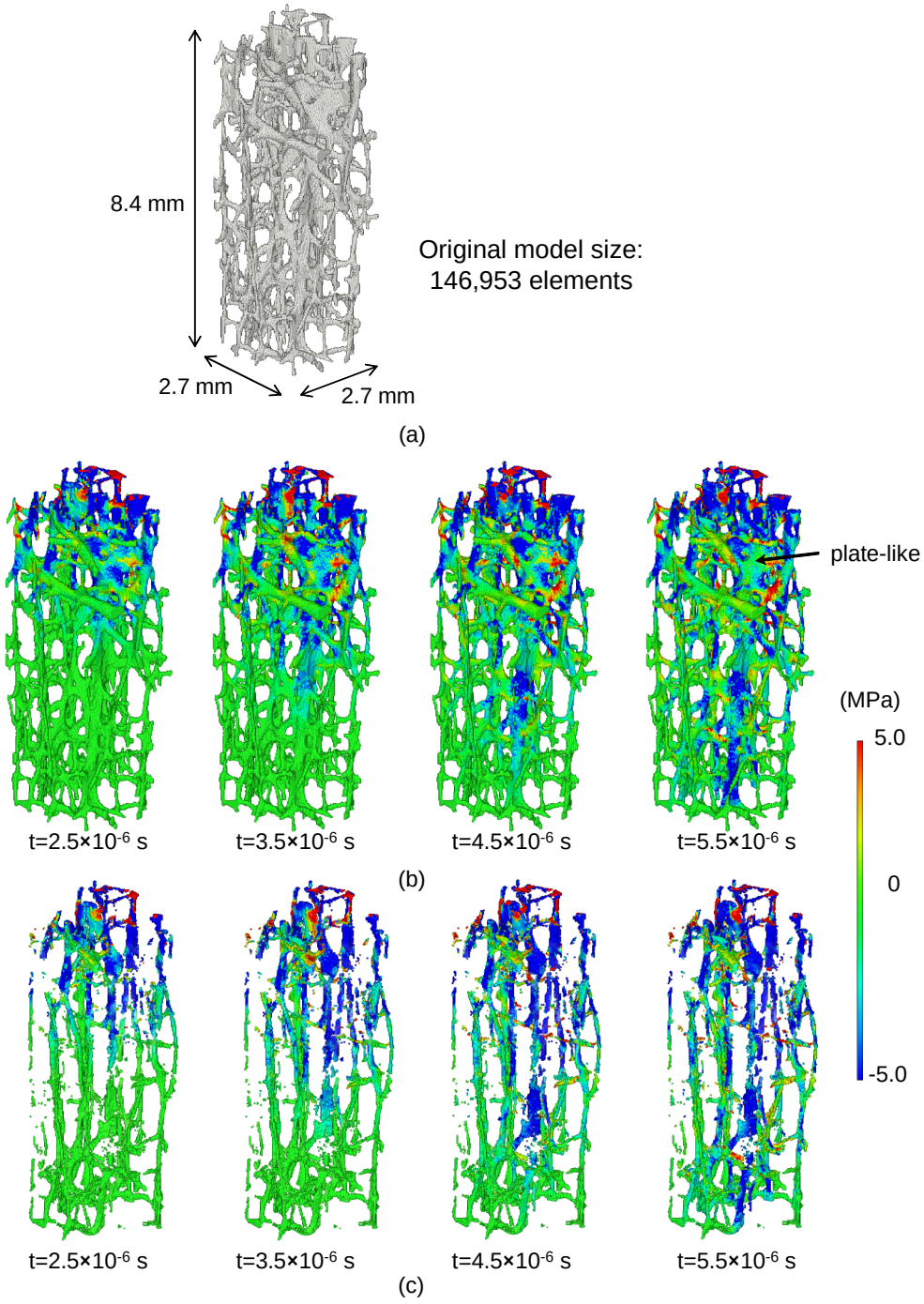

Figure 5.4: Principal stress contour for ROI No. 8 under a dynamic load. (a) Dimension and size of the original model; (b) dynamic response of the original model and (c) dynamic response of the primary trabecular. The existence of plate-like bone is denoted by the arrow.

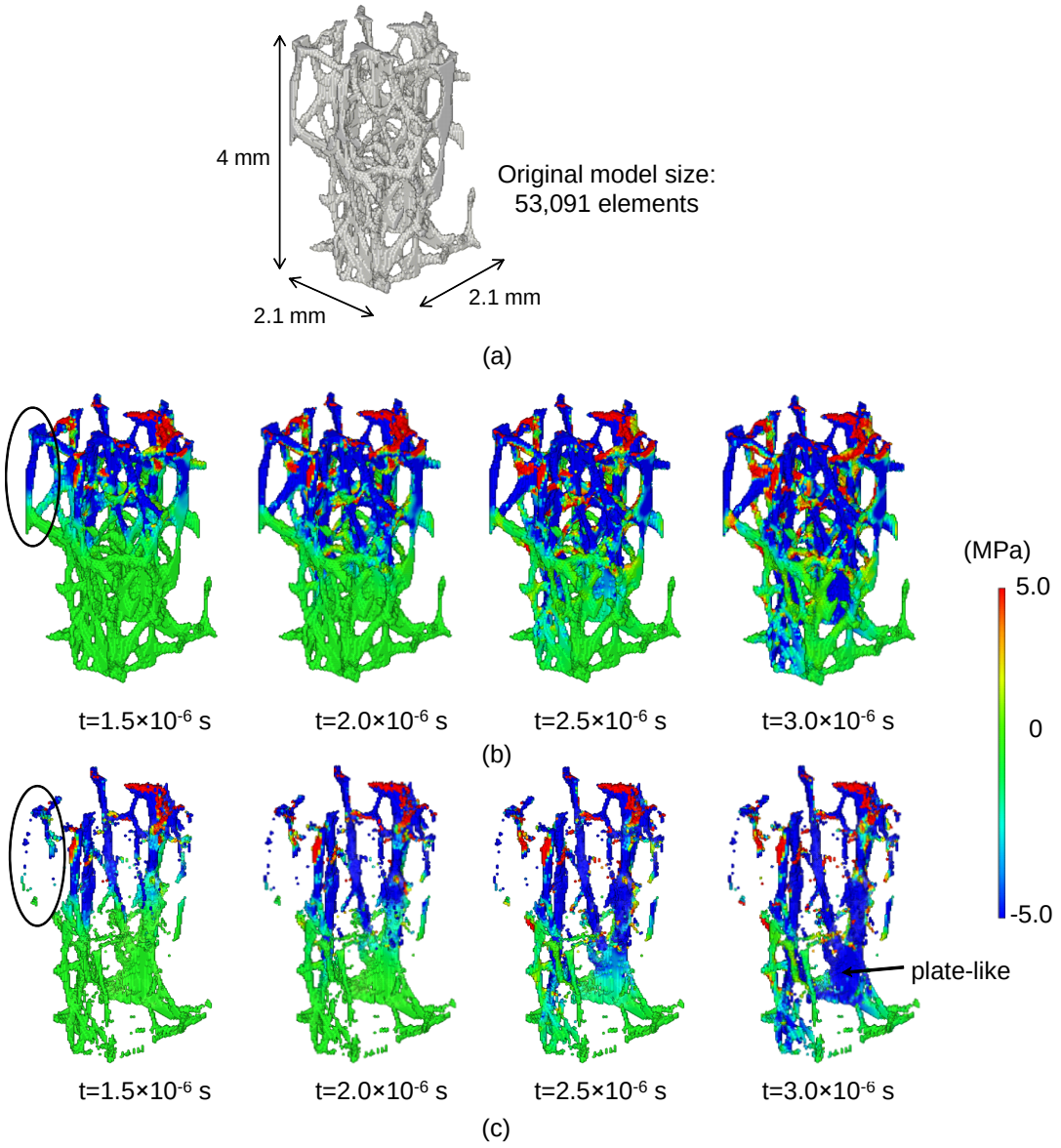

Figure 5.5: Principal stress contour for ROI No. 10 under a dynamic load. (a) Dimension and size of the original model; (b) dynamic response of the original model and (c) dynamic response of the primary trabecular.

distributed across a broader area. However, the percolated load path from the top part to the bottom is barely visible. For instance, the stress wave entered the marked part, but never penetrated through to the bottom. A rod-like trabecular that is almost vertical is not actually working as the main load path, because percolation of the network system does not exist, although other short-cut pathways are in evidence. This proves that connectivity plays a major role in load transfer capability. By eliminating trabeculae other than primary in Fig. 5.5(c), the existence and orientation of plate-like trabeculae is revealed, and it is clear that they are functioning as a load pathway. The marked trabecular was removed, and Fig. 5.6(a) shows the secondary trabecular segment. It seems that the stress waves propagated only in a horizontal direction. The segment of trabecular bone of no contribution is shown in Fig. 5.6(b), which includes the above-marked part. It appears that the stress wave was trapped in the middle of the trabecular volume, with no further percolation down to the bottom part of the trabecular region. This trabecular portion makes visibility worse, and it was successfully excluded as a result of the present static analysis and multi-scale theory.

Figure 5.7 shows the percolation of the principal stress contour in the inner region of ROI No. 6. In Fig. 5.7(b), the primary trabecular works as a main load path from the upper to the bottom parts. Most of them are in a compression condition (as displayed by the blue contour), thus corresponding to the compressive dynamic load subjected to the top of the ROI. On the other hand, the percolation of the stress wave in Fig. 5.7(c) suggests that the secondary trabecular supports the interconnected primary trabecular regarding load distribution in a lateral direction, but only in the dynamic analysis. Some parts display tension (as displayed by the red contour), in order to hold or restrict the primary trabecular from bending. In terms of trabecular size, the thickness of the main

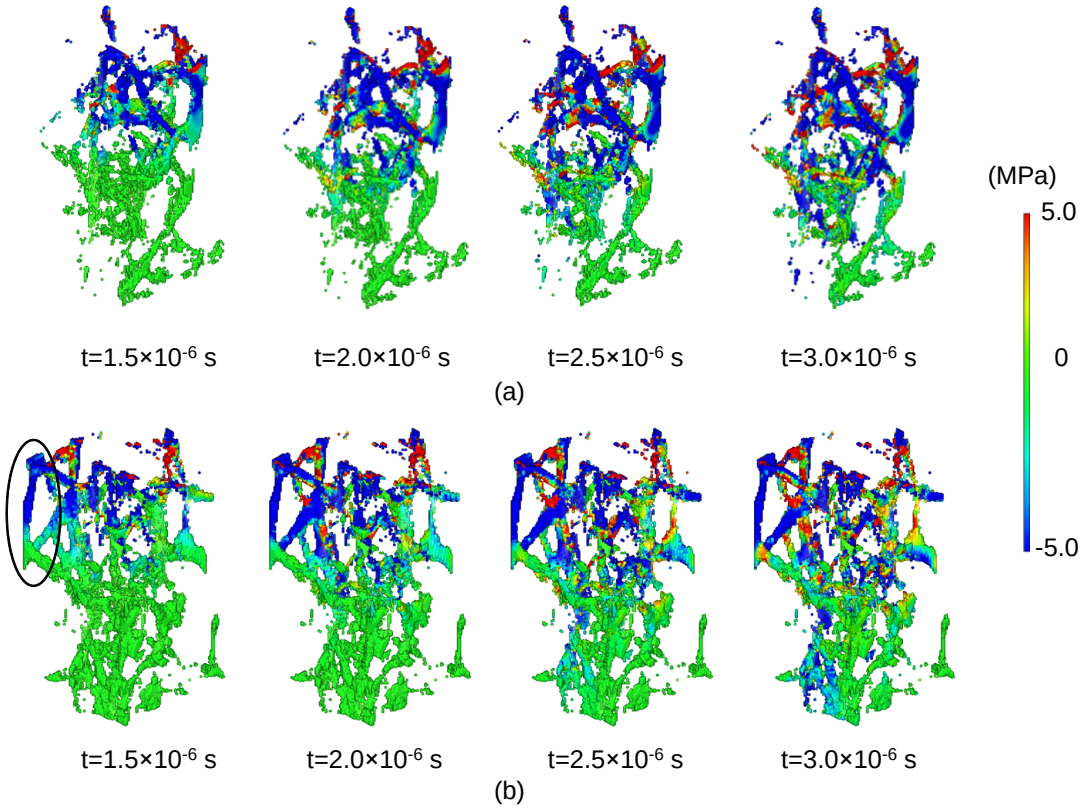

Figure 5.6: Principal stress contour for ROI No. 10 under a dynamic load for (a) secondary trabecular and (b) trabecular of no contribution. Inside the black line is a single trabecular bone with an almost vertical orientation. Plate-like trabecular bone exists near the bottom region with its face perpendicular to the principal load direction.

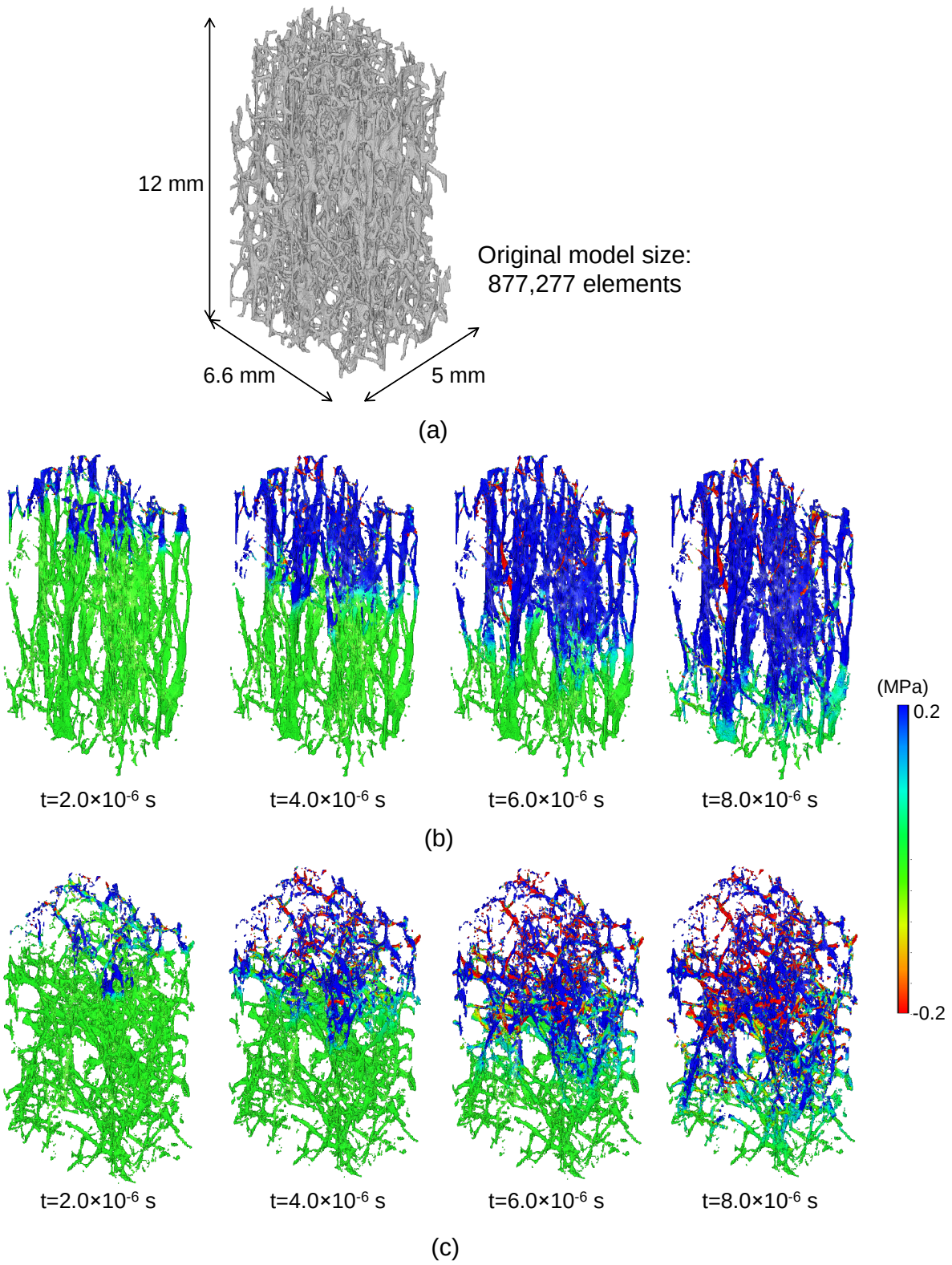

Figure 5.7: Principal stress contour for ROI No. 6 under a dynamic load. (a) Dimension and size of the original model; (b) dynamic response of the original model, and (c) dynamic response of the primary trabecular.

primary trabecular is greater than that of the secondary trabecular.

Next, penetration of the stress wave in a vertical direction for ROI No. 1 is visualized in Fig. 5.8(b). Although it is difficult to distinguish individual trabecular struts, the continuity of the load path is still recognizable; however, stress wave percolation in the secondary trabecular is hardly visualized, as shown in Fig. 5.8(c).

5.5 Trabecular network system

The results obtained in the present study suggest that the effectiveness of load-bearing capability in the trabecular microarchitecture depends on a combination of its types (rods and plates), orientation, and connectivity. Plate-like bone rather than rod-like bone contributes to the development of more efficient network systems, but its function is also influenced by its orientation (Shi *et al.*, 2010). The load is transferred smoothly among each rod-like neighbor, if the plate-like bone is parallel to the principal load direction (as discussed in Fig. 5.5(b)). If the face of the plate-like bone is not parallel to the load direction (as shown in Fig. 5.4(a)), only some of the load is distributed to the connected rod-like bone. Hence, the plate-like bone is presumed to play the role of a hub in the network system, in order to transfer the load to the connected rod-like bone. Microarchitectures with sufficient plate-like bone have some form of redundancy so the load can choose other pathways, even if some network hubs are missing. Any decreases or losses of plate-like bone in the microstructure cause the entire network system to become brittle, so that the failure risk in osteoporotic bone with diminished plate-like bone increases with additions to stress concentration as a result of the thinning of each rod-like trabecular bone (Siffert *et al.*, 1996; Homminga *et al.*, 2001; Blain *et al.*, 2008).

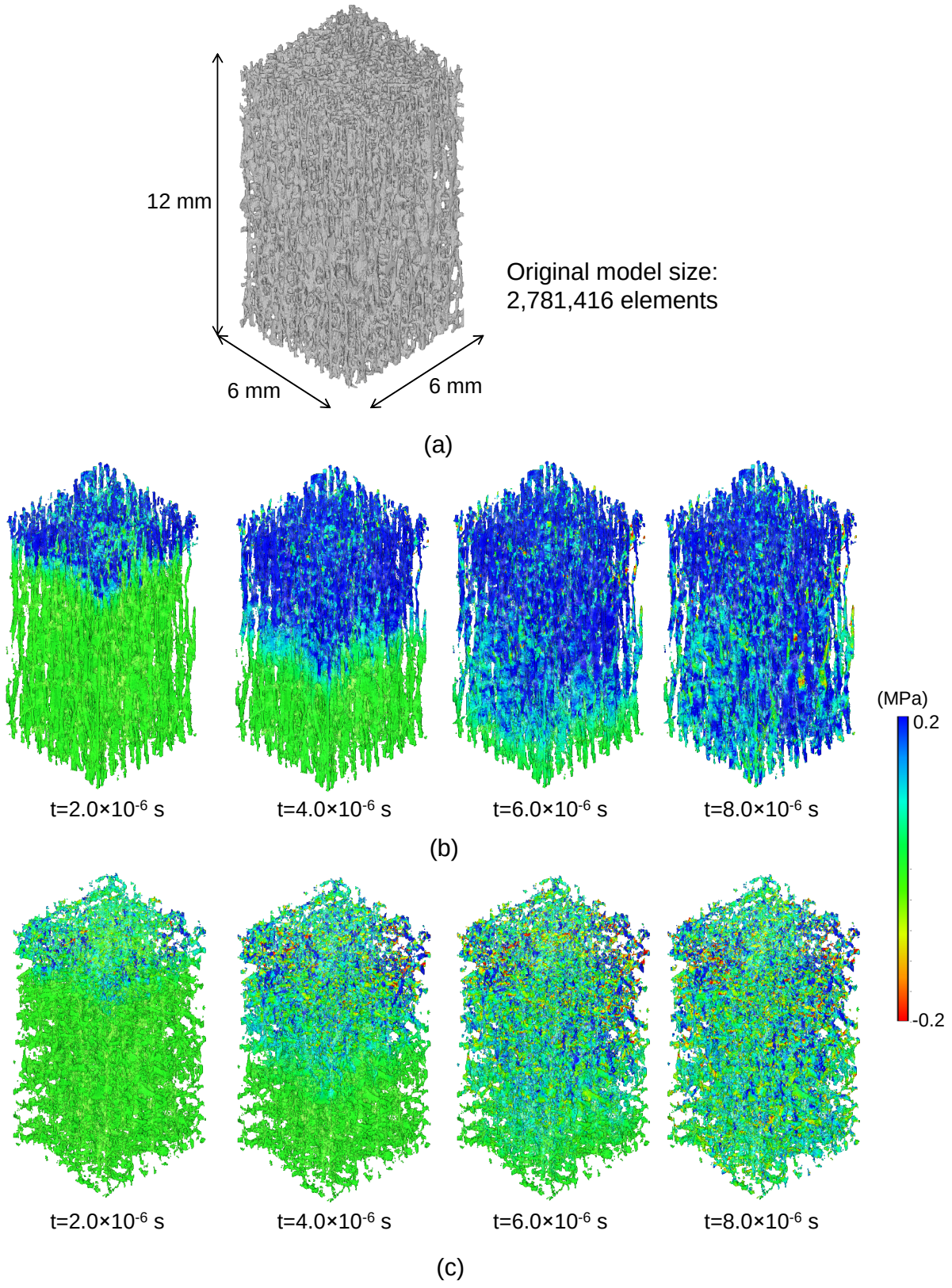

Figure 5.8: Principal stress contour for ROI No. 1 under a dynamic load. (a) Dimension and size of the original model; (b) dynamic response of the original model, and (c) dynamic response of the primary trabecular.

Moreover, an increase in connectivity among trabecular structures contributes an increase in the contact area. Hence, the ability of mechanical load transfer in the trabecular network improves because it is dependent on the contact area (Kinney and Ladd, 1998).

5.6 Summary

This study analyzed the morphology of vertebral trabecular bone by focusing on the mechanical role and load pathways of the trabecular network. A proposed classification method based on multi-scale theory was introduced, to classify trabecular segments as primary, secondary, and of no contribution. Dynamic explicit finite element analysis was conducted to investigate the morphology by viewing the percolation of stress waves in primary and secondary trabecular bone. Our results implied that plate-like bone plays the role of a hub in the trabecular network system, whereas rod-like bone was dependent on connectivity to and the orientation of load direction. The morphology of the trabecular architecture was found to play a major role in load distribution and to contribute to bone stiffness. In this study, apparent elastic properties were obtained, in order to describe anisotropic behavior caused by the morphology of the trabecular network. In conjunction with the complex disordered morphology of trabecular bone, other random parameters may arise and influence the evaluation of trabecular bone stiffness. Hence, further investigation into predicting apparent elastic moduli, by considering uncertainties in stochastic nature, is necessary, in order to ensure the reliability of the present calculations through homogenization theory.

Chapter 6

Stochastic apparent elastic moduli of trabecular bone

6.1 Introduction

An assessment of the mechanical properties of trabecular bone is essential when 'bone quality' becomes a matter of concern, in order to examine the fracture risk of human bones. The apparent mechanical properties of trabecular bone rely on many factors. In the context of bone characteristics, the effects of variations in bone volume fraction (Carter and Hayes, 1977; Keyak *et al.*, 1994), microarchitecture (Dempster, 2000; Pothuaud *et al.*, 2000), mineralization (van der Linden *et al.*, 2001; Sansalone *et al.*, 2010) and anatomical sites (Ashman *et al.*, 1989; Morgan *et al.*, 2003) on the stiffness of trabecular bone have been discussed in many research works. Bone remodeling (Adachi *et al.*, 2001) also plays a major influence on the apparent stiffness of trabecular bone, because morphology (Karim and Vashishth, 2011), mineral content (Weinans *et al.*, 1992), and biological apatite (BAp)

crystallite (Nakano *et al.*, 2005) conditions change during this process. These changes affect the stiffness of the trabecular bone tissue, and any fluctuations in mineral content and the *c*-axis orientation of BAp render trabecular bone tissue anisotropic (Tsubota and Adachi, 2004). As it is well understood that apparent mechanical properties are extremely dependent on bone tissue properties, the estimation of apparent trabecular bone stiffness should consider these uncertainty factors. Generally speaking, these factors are related mainly to inter-individual differences, due to variations in age (Thomsen *et al.*, 2002) and gender (Wolfram *et al.*, 2010). However, an investigation into the influence of inter-individual differences requires many subjects and specimens, and it is even more difficult in experimental works because destructive tests are commonly required.

Numerous experimental works over the last two decades have been conducted to measure the mechanical properties of trabecular bone, using various techniques such as ultrasonic (Rho *et al.*, 1993), compression (Anderson *et al.*, 1992; Keller, 1994), tensile (Ryan and Williamson, 1989; Rho *et al.*, 1993), bending (Choi *et al.*, 1990; Choi and Goldstein, 1992) mechanical tests, micro- (Wolfram *et al.*, 2010) and nano- (Rho *et al.*, 1997) indentation, and x-ray computed tomography (Hvid *et al.*, 1989). However, the results vary greatly despite employing the same techniques and anatomic sites. Many dependent factors contribute to errors or variations in apparent elastic moduli in the measurement process, such as the size and geometry of the trabecular specimen (Choi *et al.*, 1990; Linde *et al.*, 1992), artifact defects (Keaveny *et al.*, 1997; Ün *et al.*, 2006), energy source parameters (Hvid *et al.*, 1989), constraints (Linde and Hvid, 1989), loading conditions (Linde *et al.*, 1991), storage methods (Linde *et al.*, 1993), and others. Since there is no standard procedure available on how to measure the elastic properties of trabecular bone, some of the errors remain unchallenged, unclear, and miscellaneous.

Although a general correlation between elastic moduli of trabecular bone and bone density has been proposed in many experimental results, especially in power law relationships (Carter and Hayes, 1977; Odgaard and Linde, 1991; Keller, 1994) using the regression equation of statistical data, real experimental plots show widespread scattering (Keller, 1994; Keyak *et al.*, 1994).

Finite element methods—and particularly image-based modeling—enable the non-destructive evaluation of the apparent mechanical properties of trabecular bone. Through the availability of advanced imaging tools, realistic trabecular bone models can be generated. However, the reliability and accuracy of estimating mechanical properties are dependent on various factors within the image-processing procedure. The implications of image types, such as micro-CT, pQCT and MR images (van Rietbergen *et al.*, 1998), resolution (Bevill and Keaveny, 2009), and threshold values (Hara *et al.*, 2002; Yan *et al.*, 2012) have been found to have a major influence on the reconstruction of the trabecular bone model. Hara *et al.* (2002) reported that even a small variation in the threshold value affected bone volume fraction and morphological parameters, especially for the case of a low bone volume fraction. Moreover, unwanted artifacts (Kopperdahl *et al.*, 2002) and noise (Rajapakse *et al.*, 2009a) may be generated as part of the trabecular bone model, due to uncertainties in image-processing, and the affected trabecular connectivity (Kabel *et al.*, 1999) contributes to the fluctuation of apparent mechanical properties.

Nevertheless, in order to consider random variations in the trabecular bone microstructure caused by various uncertainty parameters, the use of a sampling method or conventional Monte Carlo simulation approach will require expensive calculation. Therefore, this study presents the stochastic multi-scale method applied to trabecular bone, in order to calculate variations in apparent elastic moduli by considering uncertainties

caused by bone characteristics, experimental works, and image-processing. The main objective is to propose a computational scheme that can predict the reliable apparent elastic moduli of trabecular bone by simulating the scattering of experimental results caused mainly by inter-individual differences, so that the reliability of the previous calculations using the deterministic homogenization method, as discussed in Chapters 4 and 5, can be proved.

6.2 Uncertainty factors to influence the apparent elastic moduli

Many uncertainty factors contribute to random variations in the microstructure of heterogeneous media, but in order to develop an appropriate probabilistic computational model, the essential step is to identify which uncertainty factor has a significant effect on the system's response. The area of interest in this study is apparent mechanical property. It is important to identify uncertainty factors so that the computational model sufficiently represents the parameters involved and any unnecessary factors can be ignored, to reduce computational cost. The use of the Phenomenon Identification and Ranking Table (PIRT) (The American Society of Mechanical Engineers, 2006) is a practical approach to identifying key uncertainty factors and helps to clarify the level of importance that can be attached to the system's response.

To show the implementation of this step, the PIRT was employed for estimating the apparent mechanical properties of trabecular bone in high-resolution micro-CT images. Table 6.1 lists the importance ranking for each particular uncertainty factor based on

Table 6.1: List of uncertainty factors and importance ranking.

Source	Uncertainty	Importance ranking
Bone characteristics	Inter-individual difference	High
	-Age	High
	-Gender	Low
	Remodeling	High
	-Morphology	High
	-Mineralization	High
	-Biological apatite (BAp)	High
Experiment	Specimen preparation	High
	Grip/chuck/end cap	High
	Specimen misalignment	High
	Constraints	High
	Loading conditions	High
	Definition of strain-stiffness	Medium
	Micro-damage	Low
Image	Artifacts and noise	High
	Connectivity	Medium
	Resolution	Medium

human bone characteristics, experimental work and image. These sources were taken into account, in order to develop a computational model of the present system's response. In the context of bone characteristics, the bone remodeling process is rated as highly important, since morphology and microscopic properties change as a result of mineralization (Sansalone *et al.*, 2010) and BAp crystallite orientation (Miyabe *et al.*, 2007). Obviously, the influence of age on mechanical properties is more significant than gender in terms of inter-individual differences.

A comparison with experimental results in developing the mathematical algorithm could improve the reliability of the computational model. However, the results obtained by the experimental study on the mechanical properties of trabecular bone produced widespread scattering, for instance, as displayed in Fig. 4.5 and performed by Keyak

et al. (1994). Very surprisingly, the vertical axis in Fig. 4.5 uses a logarithmic scale. Hence, it appears that the regression curve that corresponds to the average line of the dispersal plots does not always characterize the real behavior of each case. The scattered result is influenced by the uncertainty involved, not only during the compression test but also in the pre- and post-experimental works. The listed uncertainty in Table 6.1 depicts most of the factors that have a strong influence on the system's response, except for the definitions of the linear strain-stress relation (interpretation of the result) and micro-damage (a pre-failure mode condition), which are categorized as medium and low, respectively.

In the computational analysis of bone mechanics, the use of 3D imaging is almost compulsory when constructing a realistic microstructure model; hence, any uncertainty in imaging procedures has been considered. Although determining the threshold value (Hara *et al.*, 2002) is crucial in image processing, its purpose is to avoid unwanted artifacts and noise generated as part of the microstructure model. Thus, a high level of importance has been given to the uncertainty of artifacts and noise (Rajapakse *et al.*, 2009a), because they contribute to changes in morphology and volume fraction in the numerical model. The connectivity of rod-like trabecular bone, which determines load-bearing capability and stiffness, is also significant. Furthermore, it has been confirmed the ROI size is not particularly influential on the final result (as proved in Chapter 4). For the above reason, ROI size is excluded from the uncertainty factors.

6.3 Theoretical framework of stochastic modeling

Based on the multi-scale theory of a linear problem, the apparent elastic properties of trabecular bone $\hat{\boldsymbol{D}^{\boldsymbol{H}}}$ depend mainly on the geometry of microstructure $\hat{X}$ and the microscopic properties of bone tissue $\hat{\boldsymbol{D}}$. Variations in the geometries of trabecular bone microstructures could possibly be generated as a result of fluctuations in bone volume fraction V and morphological parameters A. In image-based modeling, imaging parameters $\hat{I}$, such as threshold value, image resolution, etc., also affect the final geometry of the trabecular bone model. Consequently, the estimation of $\hat{\boldsymbol{D}^{\boldsymbol{H}}}$ can be formulated as in Eq. (6.1):

$$\hat{\boldsymbol{D}^{\boldsymbol{H}}} = \mathcal{F}(\hat{X}(V, A, \hat{I}), \hat{\boldsymbol{D}}) \tag{6.1}$$

where $\mathcal{F}$ is a function of $\hat{\boldsymbol{D}^{\boldsymbol{H}}}$. In this study, any uncertainties that arise in the geometry of the trabecular bone microstructure and the microscopic properties of trabecular bone tissue are represented by variations in image-based modeling and c-axis BAp crystallite orientation, respectively.

Variables which contain random fluctuation are denoted by hat symbol. If the microscopic property is assumed to have a small random fluctuation, the stochastic response of the $\hat{\boldsymbol{D}}$ matrix is characterized by a sum of the deterministic term $\boldsymbol{D^*}$ and a stochastic term that is denoted by α as follows:

$$\hat{\boldsymbol{D}} = \boldsymbol{D^*}(1 + \alpha) \tag{6.2}$$

The stochastic apparent elastic properties can then be formulated as a function of α and

approximated in expansion form, as written in the following equation:

$$\hat{\boldsymbol{D}^{\boldsymbol{H}}} = \boldsymbol{D}^{\boldsymbol{H}}(\alpha) \approx \sum_{k} (\boldsymbol{D}^{\boldsymbol{H}})^k \phi^k \tag{6.3}$$

where ϕ is a fluctuation with a kth order. Based on the perturbation theory, ϕ in the equation above is equal to α. The stochastic apparent elastic properties are then rewritten in perturbation form.

$$\hat{\boldsymbol{D}^{\boldsymbol{H}}} = (\boldsymbol{D}^{\boldsymbol{H}})^0 + (\boldsymbol{D}^{\boldsymbol{H}})^1 \alpha + (\boldsymbol{D}^{\boldsymbol{H}})^2 \alpha^2 + \ldots \tag{6.4}$$

Considering the fluctuation of α is characterized by probability density function $f(\alpha)$, an expectation of the apparent elastic properties can be calculated as follows:

$$\begin{aligned} \mathrm{Exp}(\hat{\boldsymbol{D}^{\boldsymbol{H}}}) &= \int_{-\infty}^{\infty} \boldsymbol{D}^{\boldsymbol{H}}(\alpha) f(\alpha)\, d\alpha \\ &\approx \int_{-\infty}^{\infty} \left\{ (\boldsymbol{D}^{\boldsymbol{H}})^0 + (\boldsymbol{D}^{\boldsymbol{H}})^1 \alpha + \ldots \right\} f(\alpha)\, d\alpha \end{aligned} \tag{6.5}$$

Applying the first-order perturbation method to this calculation and assuming that the stochastic variable α is in the Gaussian normal distribution range with a mean value of zero, the expected value (Exp) and variance (Var) of the apparent elastic properties are computed in Eqs. (6.6) and (6.7), respectively (Koishi *et al.*, 1996; Sakata *et al.*, 2008):

$$\mathrm{Exp}(\hat{\boldsymbol{D}^{\boldsymbol{H}}}) = (\boldsymbol{D}^{\boldsymbol{H}})^0 \tag{6.6}$$

$$\begin{aligned} \mathrm{Var}(\hat{\boldsymbol{D}^{\boldsymbol{H}}}) &= \int_{-\infty}^{\infty} (\boldsymbol{D}^{\boldsymbol{H}}(\alpha) - \mathrm{Exp}(\hat{\boldsymbol{D}^{\boldsymbol{H}}}))^2 f(\alpha)\, d\alpha \\ &= (\boldsymbol{D}^{\boldsymbol{H}})^1 (\boldsymbol{D}^{\boldsymbol{H}})^1 \int_{-\infty}^{\infty} \alpha^2 f(\alpha)\, d\alpha \\ &= (\boldsymbol{D}^{\boldsymbol{H}})^1 (\boldsymbol{D}^{\boldsymbol{H}})^1 \mathrm{cov}\,(\alpha, \alpha) \end{aligned} \tag{6.7}$$

where cov(α,α) is the covariance of α. The order of '0' is defined as the deterministic term, whereas '1' corresponds to the first-order differential for stochastic variation α at α = 0.

The apparent elastic properties derived here are in tensor matrix form. In order to obtain stochastic apparent elastic moduli, the inverse of the tensor matrix form is derived. Let the first-order approximation of the stochastic elastic properties be written as follows:

$$\hat{\boldsymbol{D}^{\boldsymbol{H}}} = (\boldsymbol{D}^{\boldsymbol{H}})^0 + (\boldsymbol{D}^{\boldsymbol{H}})^1 \alpha \tag{6.8}$$

Taking the inverse, we obtain $\hat{C_{ij}^H}$ (for i, j=1-3)

$$\hat{\boldsymbol{C}^{\boldsymbol{H}}} = (\hat{\boldsymbol{D}^{\boldsymbol{H}}})^{-1} = \frac{1}{|\hat{\boldsymbol{D}^{\boldsymbol{H}}}|} \begin{bmatrix} c_{11} & c_{12} & c_{13} \\ c_{21} & c_{22} & c_{23} \\ c_{31} & c_{32} & c_{33} \end{bmatrix} \tag{6.9}$$

where

$$|\hat{\boldsymbol{D}^{\boldsymbol{H}}}| = (D_{11}^{H0} + D_{11}^{H1}\alpha)(D_{22}^{H0} + D_{22}^{H1}\alpha)(D_{33}^{H0} + D_{33}^{H1}\alpha) + ... \tag{6.10}$$

The approximation up to the first order of α yields

$$|\hat{\boldsymbol{D}^{\boldsymbol{H}}}| = (D_{11}^{H0} D_{22}^{H0} D_{33}^{H0} + ...) + (D_{11}^{H1} D_{22}^{H0} D_{33}^{H0} + D_{11}^{H0} D_{22}^{H1} D_{33}^{H0} + D_{11}^{H0} D_{22}^{H0} D_{33}^{H1} + ...)\alpha \tag{6.11}$$

which can be simplified as

$$|\hat{\boldsymbol{D}^{\boldsymbol{H}}}| = \left(|\boldsymbol{D}^{\boldsymbol{H}}|\right)^0 + \left(|\boldsymbol{D}^{\boldsymbol{H}}|\right)^1 \alpha \tag{6.12}$$

Using a similar method, each component of c_{ij} can be obtained as

$$\begin{aligned} c_{11} &= (D_{22}^{H0} + D_{22}^{H1}\alpha)(D_{33}^{H0} + D_{33}^{H1}\alpha) - (D_{32}^{H0} + D_{32}^{H1}\alpha)(D_{23}^{H0} + D_{23}^{H1}\alpha) \\ &= (D_{22}^{H0}D_{33}^{H0} - D_{32}^{H0}D_{23}^{H0}) + (D_{22}^{H0}D_{33}^{H1} + D_{22}^{H1}D_{33}^{H0} - D_{32}^{H0}D_{23}^{H1} - D_{32}^{H1}D_{23}^{H0})\alpha \end{aligned} \tag{6.13}$$

$$\begin{aligned} c_{21} &= -\left\{(D_{12}^{H0} + D_{12}^{H1}\alpha)(D_{33}^{H0} + D_{33}^{H1}\alpha) - (D_{32}^{H0} + D_{32}^{H1}\alpha)(D_{13}^{H0} + D_{13}^{H1}\alpha)\right\} \\ &= (D_{32}^{H0}D_{13}^{H0} - D_{12}^{H0}D_{33}^{H0}) + (D_{32}^{H0}D_{13}^{H1} + D_{32}^{H1}D_{13}^{H0} - D_{12}^{H0}D_{33}^{H1} - D_{12}^{H1}D_{33}^{H0})\alpha \end{aligned} \tag{6.14}$$

$$\begin{aligned} c_{31} &= -\left\{(D_{12}^{H0} + D_{12}^{H1}\alpha)(D_{23}^{H0} + D_{23}^{H1}\alpha) - (D_{13}^{H0} + D_{13}^{H1}\alpha)(D_{22}^{H0} + D_{22}^{H1}\alpha)\right\} \\ &= (D_{13}^{H0}D_{22}^{H0} - D_{12}^{H0}D_{23}^{H0}) + (D_{13}^{H0}D_{22}^{H1} + D_{13}^{H1}D_{22}^{H0} - D_{12}^{H0}D_{23}^{H1} - D_{12}^{H1}D_{23}^{H0})\alpha \end{aligned} \tag{6.15}$$

$$\vdots$$

$$\hat{\boldsymbol{c}} = \boldsymbol{c}^0 + \boldsymbol{c}^1\alpha \tag{6.16}$$

Then, using the approximation of Eqs. (6.12) to (6.16), the stochastic compliance matrix $\hat{\boldsymbol{C^H}}$ can be written as

$$\hat{\boldsymbol{C^H}} = \frac{\boldsymbol{c}^0 + \boldsymbol{c}^1\alpha}{\left(|\boldsymbol{D}^{\boldsymbol{H}}|\right)^0 + \left(|\boldsymbol{D}^{\boldsymbol{H}}|\right)^1 \alpha} \tag{6.17}$$

Taking the approximation $1/(1+x) = 1 - x - x^2$, where $x \ll 1$, Eq. (6.17) can be written

in an expanded form by neglecting the higher order of α:

$$\hat{\boldsymbol{C^H}} = \frac{\boldsymbol{c}^0}{\left(|\boldsymbol{D^H}|\right)^0} + \left(\frac{\boldsymbol{c}^1(|\boldsymbol{D^H}|)^0 - \boldsymbol{c}^0(|\boldsymbol{D^H}|)^1}{\left((|\boldsymbol{D^H}|)^0\right)^2} \right) \alpha = (\boldsymbol{C^H})^0 + (\boldsymbol{C^H})^1 \alpha \tag{6.18}$$

Using a similar approach for i, j = (4,4),(5,5),(6,6), the stochastic compliance matrix $\hat{C_{ij}^H}$ is written as

$$\hat{\boldsymbol{C^H}} = \frac{1}{\hat{\boldsymbol{D^H}}} = \frac{1}{(\boldsymbol{D^H})^0 + (\boldsymbol{D^H})^1 \alpha} = \frac{1}{(\boldsymbol{D^H})^0} - \frac{(\boldsymbol{D^H})^1}{\left((\boldsymbol{D^H})^0\right)^2} \alpha \tag{6.19}$$

As trabecular bone is an orthotropic material, the stochastic apparent elastic moduli are calculated as follows:

$$\hat{E_{11}^H} = \frac{1}{C_{11}^{H0}} - \frac{C_{11}^{H1}}{(C_{11}^{H0})^2}\alpha = E_{11}^{H0} + E_{11}^{H1}\alpha \tag{6.20}$$

$$\hat{E_{22}^H} = \frac{1}{C_{22}^{H0}} - \frac{C_{11}^{H1}}{(C_{22}^{H0})^2}\alpha = E_{22}^{H0} + E_{22}^{H1}\alpha \tag{6.21}$$

$$\hat{E_{33}^H} = \frac{1}{C_{33}^{H0}} - \frac{C_{33}^{H1}}{(C_{33}^{H0})^2}\alpha = E_{33}^{H0} + E_{33}^{H1}\alpha \tag{6.22}$$

$$\hat{\nu_{32}^H} = -\frac{E_{33}^{H0}}{C_{32}^{H0}} - \left(\frac{E_{33}^{H1}}{C_{32}^{H0}} + \frac{E_{33}^{H0} C_{32}^{H1}}{(C_{32}^{H0})^2} \right) \alpha = \nu_{32}^{H0} + \nu_{32}^{H1}\alpha \tag{6.23}$$

$$\hat{\nu_{31}^H} = -\frac{E_{33}^{H0}}{C_{31}^{H0}} - \left(\frac{E_{33}^{H1}}{C_{31}^{H0}} + \frac{E_{33}^{H0} C_{31}^{H1}}{(C_{31}^{H0})^2} \right) \alpha = \nu_{31}^{H0} + \nu_{31}^{H1}\alpha \tag{6.24}$$

$$\hat{\nu_{21}^H} = -\frac{E_{22}^{H0}}{C_{21}^{H0}} - \left(\frac{E_{22}^{H1}}{C_{21}^{H0}} + \frac{E_{22}^{H0} C_{21}^{H1}}{(C_{21}^{H0})^2} \right) \alpha = \nu_{21}^{H0} + \nu_{21}^{H1}\alpha \tag{6.25}$$

$$\hat{G_{23}^H} = \frac{1}{C_{44}^{H0}} - \frac{C_{44}^{H1}}{(C_{44}^{H0})^2}\alpha = G_{23}^{H0} + G_{23}^{H1}\alpha \tag{6.26}$$

$$\hat{G_{31}^H} = \frac{1}{C_{55}^{H0}} - \frac{C_{55}^{H1}}{(C_{55}^{H0})^2}\alpha = G_{31}^{H0} + G_{31}^{H1}\alpha \tag{6.27}$$

$$\hat{G_{12}^H} = \frac{1}{C_{66}^{H0}} - \frac{C_{66}^{H1}}{(C_{66}^{H0})^2}\alpha = G_{12}^{H0} + G_{12}^{H1}\alpha \tag{6.28}$$

Finally, the expected values of and variances in the apparent elastic moduli $\hat{S^H}$ are calculated by using the first-order perturbations second moment, expressed as follows:

$$\mathrm{Exp}(\hat{S^H}) = (S^H)^0 \tag{6.29}$$

$$\mathrm{Var}(\hat{S^H}) = (S^H)^1(S^H)^1\mathrm{cov}\,(\alpha,\alpha) \tag{6.30}$$

where $(S^H)^0$ and $(S^H)^1$ represent the zeroth and first-order of each apparent elastic modulus derived in Eqs. (6.20) through (6.28).

6.4 Stochastic image-based multi-scale method: first-order perturbation

6.4.1 Image-based modeling

According to the list of uncertainties highlighted in Table 6.1, the applicability of each factor in computational modeling has been clarified. At first, uncertainty in imaging procedures was modeled, in order to create a variation in the trabecular morphology of one bone specimen. The voxel (cubic-type) finite element was used in the construction of the microstructure model. Eight image-based modeling treatments were proposed, to compensate for analyzing many individual specimens, by generating eight types of

Table 6.2: Image-based modeling treatments.

I	Image-based modeling process
1	labelling
2	labelling→voxel edge→labelling
3	labelling→dilation→erosion→labelling
4	labelling→dilation→erosion→voxel edge→labelling
5	labelling→dilation×2→erosion×2→voxel edge→labelling
6	labelling→dilation×2→erosion×2→labelling
7	labelling→dilation×3→erosion×3→voxel edge→labelling
8	labelling→dilation×3→erosion×3→labelling

morphology to represent inter-individual differences.

The proposed image-based modeling treatments for each model are listed in Table 6.2. The labeling process was implemented, in order to eliminate noises and artifacts that exist after reconstructing the 3D model. In the voxel edge process, for each two voxel elements that were only connected at one edge, the other two neighboring voxel elements were generated. The two-dimensional illustration of this process is shown in Fig. 6.1(a). In the dilation-erosion process, the connectivity of the microstructure was improved. Figure 6.1(b-d) illustrates the possible outcome models that could be created when performing the dilation-erosion process. Figures 6.2 to 6.4 show the reconstructed trabecular bone models according to the treatments proposed in Table 6.2, for ROIs O1, H1 and H2, respectively. At a glance it is difficult to identify the differences in each case, but by comparing some parts as indicated in the dotted line circle, the changes are apparent.

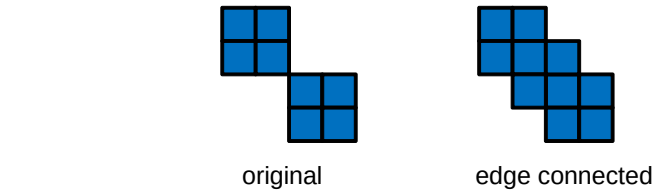

(a) voxel edge

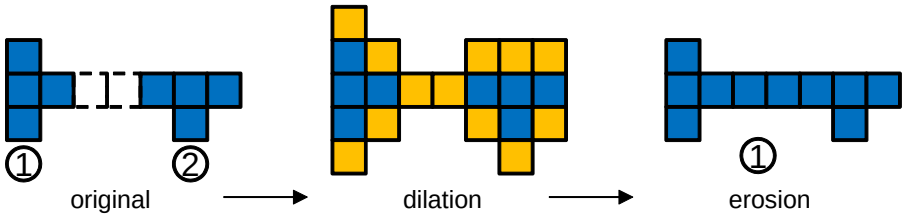

(b) dilation→erosion (connected)

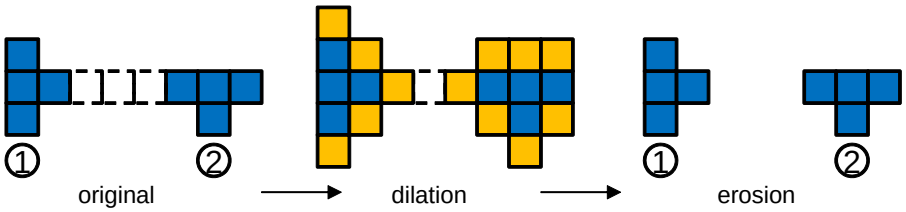

(c) dilation→erosion (not connected)

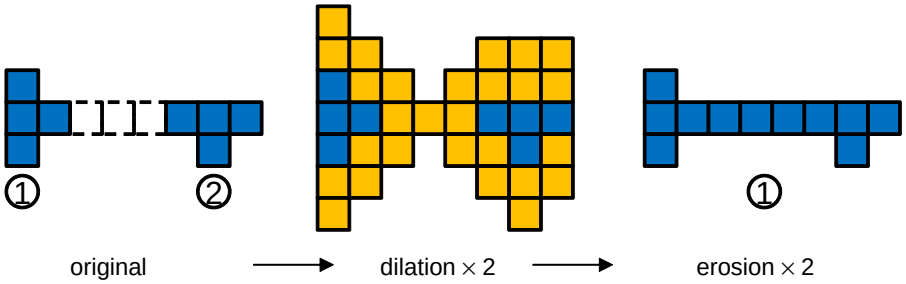

(d) dilation×2→erosion×2 (connected)

Figure 6.1: Illustration of 2D voxel elements subjected to image-based modeling treatments.

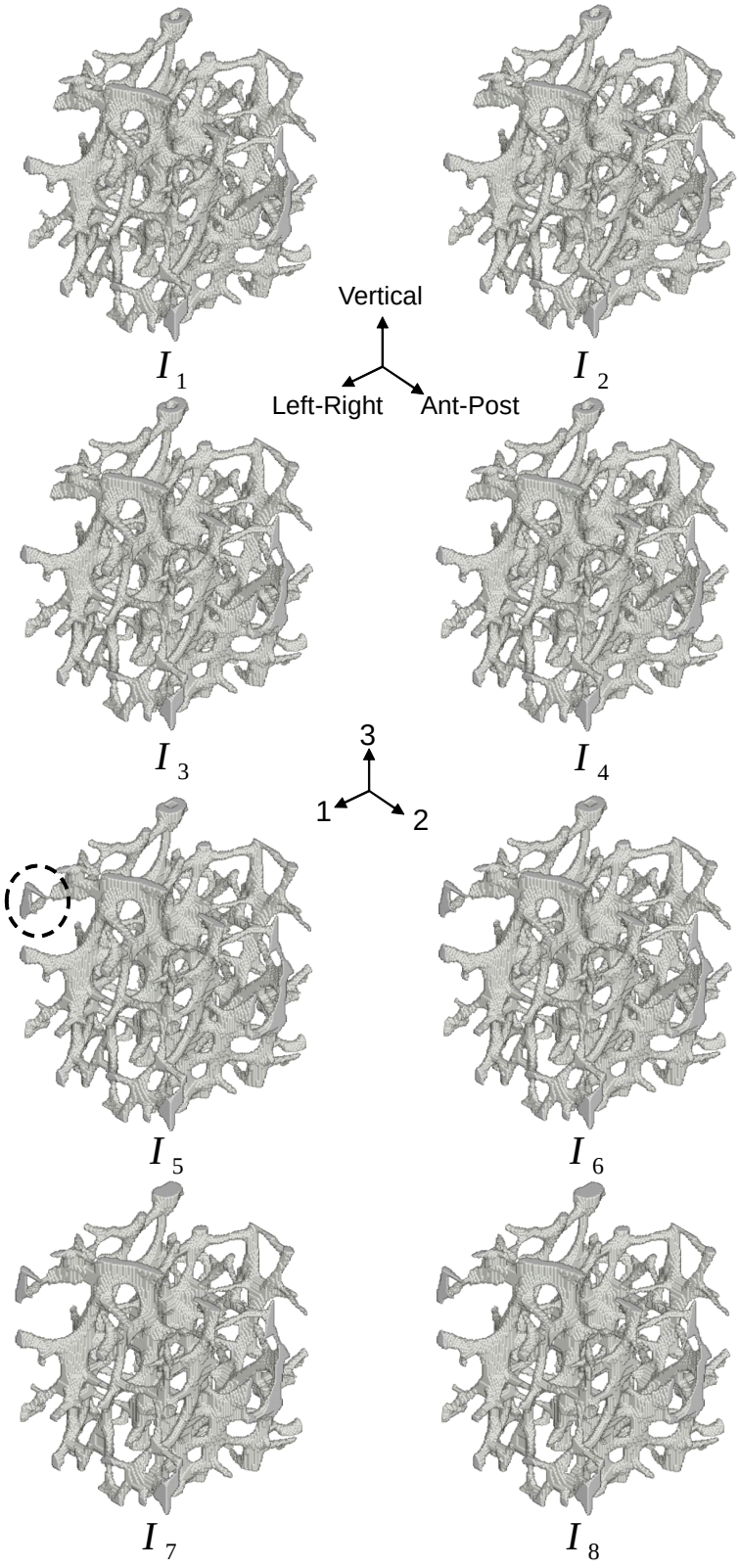

Figure 6.2: Reconstructed trabecular bone models under eight image-based modeling treatments for ROI O1.

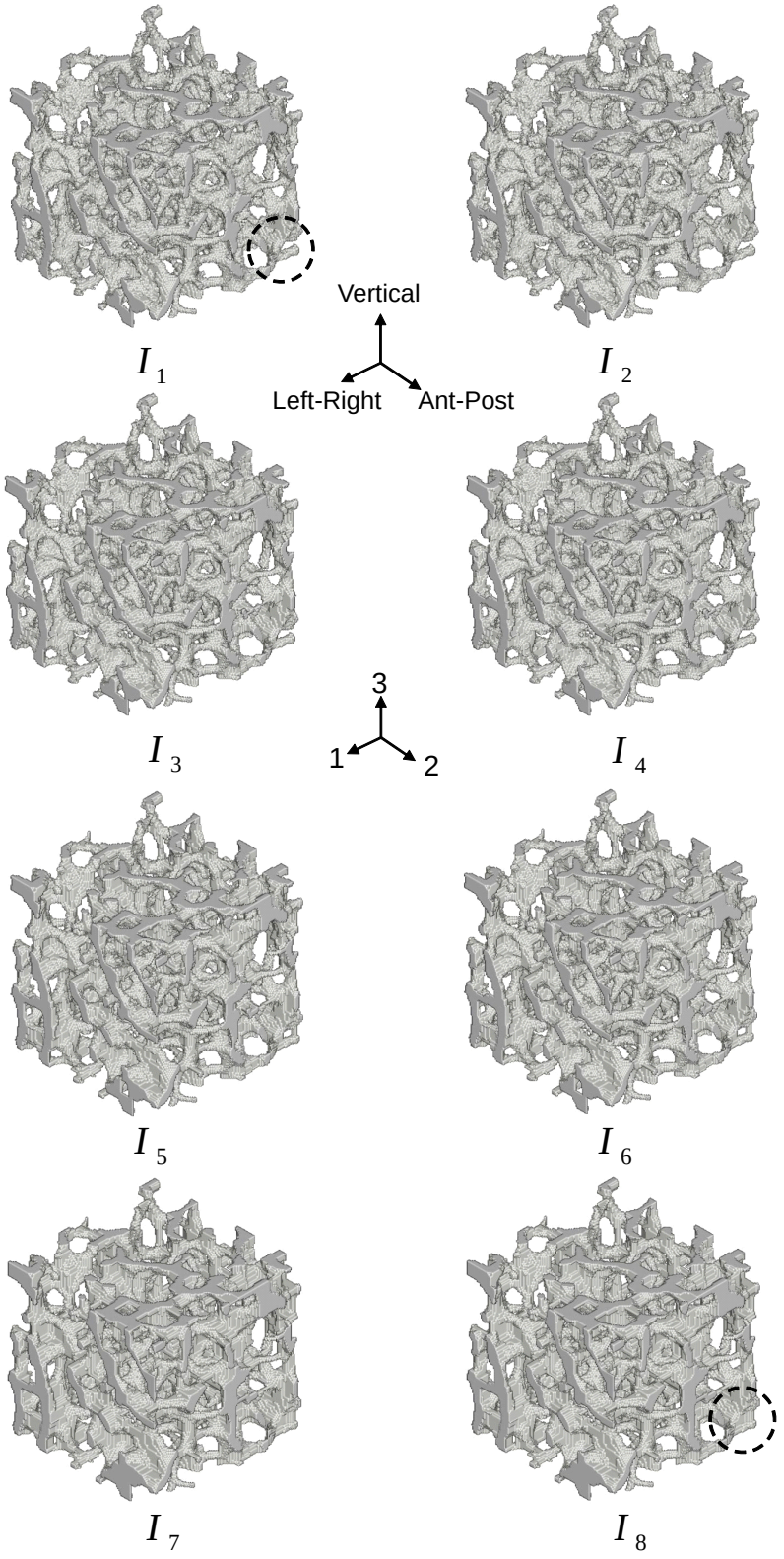

Figure 6.3: Reconstructed trabecular bone models under eight image-based modeling treatments for ROI H1.

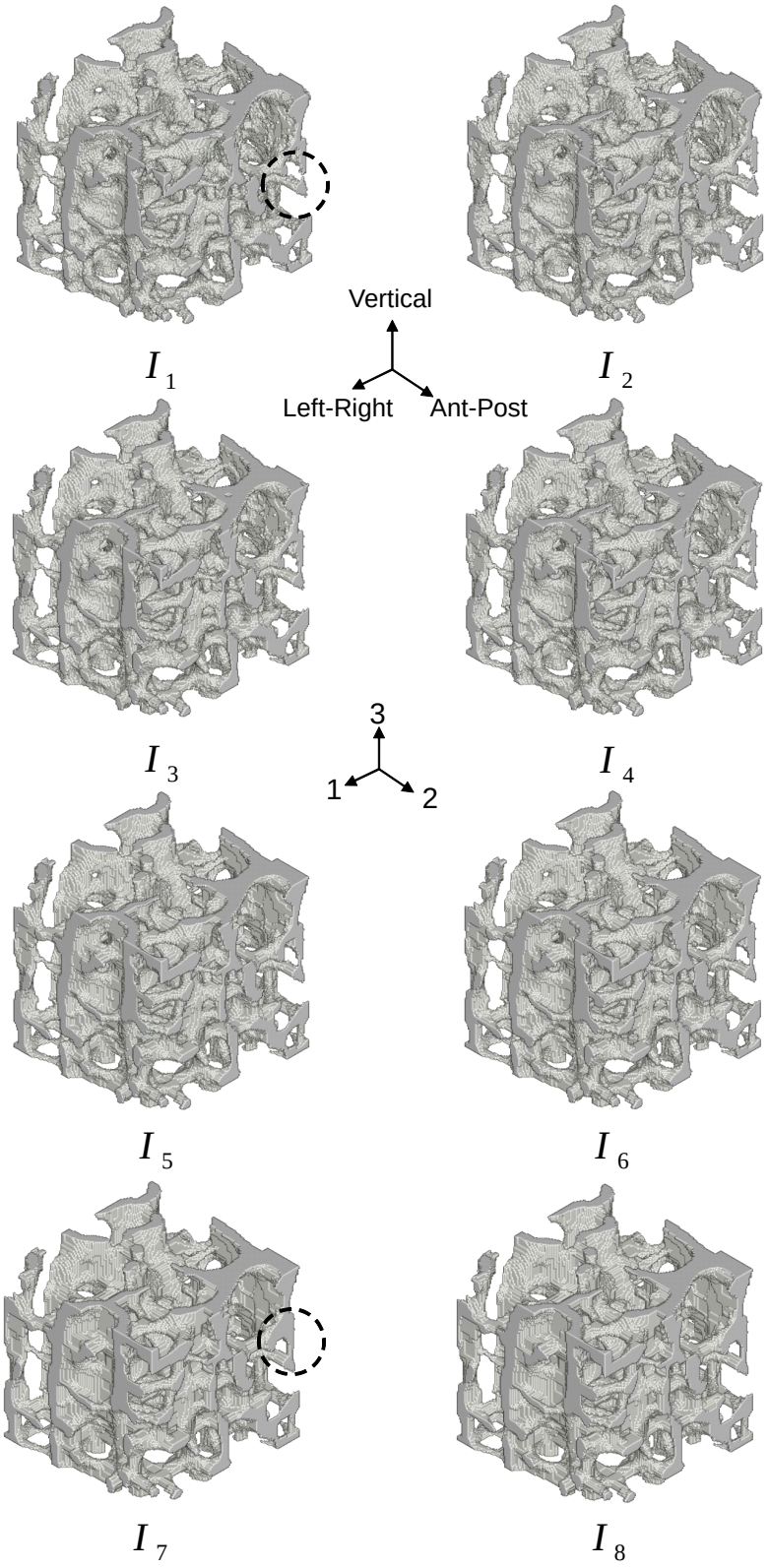

Figure 6.4: Reconstructed trabecular bone models under eight image-based modeling treatments for ROI H2.

6.4.2 BAp crystallite orientation

Uncertainty regarding the trabecular stiffness of bone tissue might arise due to the bone remodeling process reacting against mechanical loads. Trabecular bone tissue was found stiffer in the preferential alignment of the *c*-axis BAp crystallite orientation than the other directions by measuring using an X-ray diffraction method (Miyabe *et al.*, 2007). Fluctuations in the alignment of the *c*-axis BAp crystallite at the nano-scale that result from bone remodeling might cause variations in trabecular stiffness. Thus, the stochastic anisotropy in the material axis of trabecular bone tissue was investigated in this study. The fluctuation of the *c*-axis's orientation with respect to the principal axis of the trabecular microstructure (or in axis-3 for the present model) was assumed as normally distributed after X-ray diffraction measurement (Miyabe *et al.*, 2007), following which the Young's modulus of the trabecular bone tissue in axis-3 $\hat{E}_3$ was written as follows:

$$\hat{E}_3 = E^0(1+\alpha) \tag{6.31}$$

where E^0 is the deterministic Young's modulus of trabecular bone tissue. Next, the fluctuation in the Young's modulus in the other two orthogonal axes was set at half of that in the principal axis, as written in Eq. (6.32):

$$\hat{E}_1 = \hat{E}_2 = \frac{\hat{E}_3}{2} = \frac{E^0}{2}(1+\alpha) \tag{6.32}$$

The deterministic Poisson's ratio ν and the stochastic response of shear modulus $\hat{G}$ were set as Eqs. (6.33) and (6.34), respectively, in order to hold the symmetry of the compliance matrix.

$$\nu_{21} = \nu_{12} = \nu_{31} = \nu_{32} = \nu \text{ and } \nu_{13} = \nu_{23} = \frac{\nu}{2} \tag{6.33}$$

$$\hat{G_{23}} = \hat{G_{31}} = \hat{G_{12}} = \frac{E^0}{2(1+\nu)}(1+\alpha) \tag{6.34}$$

Next, compliance matrix $\hat{\boldsymbol{C}}$, considering the uncertainty of the Young's modulus, can be written as:

$$\hat{\boldsymbol{C}} = \begin{bmatrix} \frac{2}{E^0(1+\alpha)} & -\frac{2\nu}{E^0(1+\alpha)} & -\frac{\nu}{E^0(1+\alpha)} & 0 & 0 & 0 \\ -\frac{2\nu}{E^0(1+\alpha)} & \frac{2}{E^0(1+\alpha)} & -\frac{\nu}{E^0(1+\alpha)} & 0 & 0 & 0 \\ -\frac{\nu}{E^0(1+\alpha)} & -\frac{\nu}{E^0(1+\alpha)} & \frac{1}{E^0(1+\alpha)} & 0 & 0 & 0 \\ 0 & 0 & 0 & \frac{2(1+\nu)}{E^0(1+\alpha)} & 0 & 0 \\ 0 & 0 & 0 & 0 & \frac{2(1+\nu)}{E^0(1+\alpha)} & 0 \\ 0 & 0 & 0 & 0 & 0 & \frac{2(1+\nu)}{E^0(1+\alpha)} \end{bmatrix} \tag{6.35}$$

To obtain stochastic bone tissue properties $\hat{\boldsymbol{D}}$, take the inverse of the compliance matrix. This manipulation yields

$$\hat{\boldsymbol{D}} = \frac{E^0}{4}(1+\alpha)\begin{bmatrix} \frac{2-\nu^2}{(1-\nu-\nu^2)(\nu+1)} & \frac{\nu^2+2\nu}{(1-\nu-\nu^2)(\nu+1)} & \frac{2\nu}{(1-\nu-\nu^2)} & 0 & 0 & 0 \\ \frac{\nu^2+2\nu}{(1-\nu-\nu^2)(\nu+1)} & \frac{2-\nu^2}{(1-\nu-\nu^2)(\nu+1)} & \frac{2\nu}{(1-\nu-\nu^2)} & 0 & 0 & 0 \\ \frac{2\nu}{(1-\nu-\nu^2)} & \frac{2\nu}{(1-\nu-\nu^2)} & \frac{4(1-\nu)}{(1-\nu-\nu^2)} & 0 & 0 & 0 \\ 0 & 0 & 0 & \frac{4}{2(1+\nu)} & 0 & 0 \\ 0 & 0 & 0 & 0 & \frac{4}{2(1+\nu)} & 0 \\ 0 & 0 & 0 & 0 & 0 & \frac{4}{2(1+\nu)} \end{bmatrix} \tag{6.36}$$

Details of the setup of anisotropy in trabecular bone tissue and the random variable are described in Appendix A.

6.4.3 Derivation of stochastic apparent elastic moduli

Based on the deterministic asymptotic homogenization theory, geometrical information $\hat{X}$ in Eq. (6.1) is replaced by characteristic displacement $\hat{\boldsymbol{\chi}}$ and is written as:

$$\hat{\boldsymbol{D}^{\boldsymbol{H}}} = \mathcal{F}\left(\hat{\boldsymbol{\chi}}(V, A, \hat{I}), \hat{\boldsymbol{D}}(\alpha)\right) \tag{6.37}$$

Considering the volume of the 3D image-based model $\hat{Y}$ relies on jth image-based modeling treatments I_j, $\hat{\boldsymbol{D}^{\boldsymbol{H}}}$ is calculated by Eq. (6.38):

$$\hat{\boldsymbol{D}^{\boldsymbol{H}}}_{I_j} = \frac{1}{|\hat{Y_{I_j}}|} \int_{\hat{Y_{I_j}}} \hat{\boldsymbol{D}} \left(\mathrm{I} - \frac{\partial \hat{\chi}}{\partial y}\right) d\hat{Y_{I_j}} \tag{6.38}$$

where $\hat{Y_{I_j}}$ is dependent on the parameters V, A and $\hat{I}$.

$$\hat{Y_{I_j}} \equiv Y_{I_j}(V, A, \hat{I}) \tag{6.39}$$

$\hat{\boldsymbol{\chi}}$ is the solution of the microscopic equation and is written in the following linear algebraic form:

$$\hat{\boldsymbol{K}}\hat{\boldsymbol{\chi}} = \hat{\boldsymbol{F}} = \int_{\hat{Y_{I_j}}} \boldsymbol{B}\bar{\boldsymbol{D}}\, d\hat{Y_{I_j}} \tag{6.40}$$

where $\boldsymbol{B}$ is the strain-displacement matrix and $\bar{\boldsymbol{D}}$ a vector extracted from the $\hat{\boldsymbol{D}}$ matrix due to heterogeneity at the microscopic scale, based on the asymptotic homogenization theory (Guedes and Kikuchi, 1990). Because the random fluctuation is assumed to arise

in $\hat{\boldsymbol{D}}$, stiffness matrix $\hat{\boldsymbol{K}}$ and vector $\hat{\boldsymbol{F}}$ are approximated using a first-order perturbation:

$$\begin{aligned}\hat{\boldsymbol{K}} &\approx \boldsymbol{K}^0 + \boldsymbol{K}^1\alpha \\ &= \int_{\hat{Y_{I_j}}} \boldsymbol{B}^T\boldsymbol{D}^0\boldsymbol{B}\, d\hat{Y_{I_j}} + \left\{\int_{\hat{Y_{I_j}}} \boldsymbol{B}^T \frac{\partial\hat{\boldsymbol{D}}}{\partial\alpha}\Big|_{\alpha=0}\boldsymbol{B}\, d\hat{Y_{I_j}}\right\}\alpha\end{aligned} \tag{6.41}$$

$$\begin{aligned}\hat{\boldsymbol{F}} &\approx \boldsymbol{F}^0 + \boldsymbol{F}^1\alpha \\ &= \int_{\hat{Y_{I_j}}} \boldsymbol{B}\bar{\boldsymbol{D}}^0\, d\hat{Y_{I_j}} + \left\{\int_{\hat{Y_{I_j}}} \boldsymbol{B}\frac{\partial\bar{\boldsymbol{D}}}{\partial\alpha}\Big|_{\alpha=0} d\hat{Y_{I_j}}\right\}\alpha\end{aligned} \tag{6.42}$$

When random quantities are inserted into $\hat{\boldsymbol{K}}$ and $\hat{\boldsymbol{F}}$ in Eq. (6.40), the linear algebraic equation should be rewritten. Therefore, vector $\hat{\boldsymbol{\chi}}$ is also expressed in an approximate form:

$$\hat{\boldsymbol{\chi}} \approx \boldsymbol{\chi}^0 + \boldsymbol{\chi}^1\alpha \tag{6.43}$$

Substituting Eqs. (6.41 through 6.43) into the linear algebraic equation gives the following equation.

$$\left(\boldsymbol{K}^0 + \boldsymbol{K}^1\alpha\right)\left(\boldsymbol{\chi}^0 + \boldsymbol{\chi}^1\alpha\right) = \boldsymbol{F}^0 + \boldsymbol{F}^1\alpha \tag{6.44}$$

By equating the order of α in Eq. (6.44), the solution for the zeroth and first orders of α is calculated as Eqs. (6.45) and (6.46) with a periodic boundary condition:

$$\boldsymbol{\chi}^0 = \left(\boldsymbol{K}^0\right)^{-1}\boldsymbol{F}^0 \tag{6.45}$$

and

$$\boldsymbol{\chi}^1 = \left(\boldsymbol{K}^0\right)^{-1}\left(\boldsymbol{F}^1 - \boldsymbol{K}^1\boldsymbol{\chi}^0\right) \tag{6.46}$$

Next, using a similar approach we substitute the perturbation form of the $\hat{\boldsymbol{D}}$ matrix and vector $\hat{\boldsymbol{\chi}}$ into Eq. (6.38), which yields:

$$\hat{\boldsymbol{D}\boldsymbol{H}}_{I_j} = \frac{1}{|\hat{Y_{I_j}}|}\int_{\hat{Y_{I_j}}} (\boldsymbol{D}^0 + \boldsymbol{D}^1\alpha)\, d\hat{Y_{I_j}} - \frac{1}{|\hat{Y_{I_j}}|}\int_{\hat{Y_{I_j}}} (\boldsymbol{D}^0 + \boldsymbol{D}^1\alpha)\boldsymbol{B}\left(\boldsymbol{\chi}^0 + \boldsymbol{\chi}^1\alpha\right)\, d\hat{Y_{I_j}} \quad (6.47)$$

Finally, the zeroth and first orders of the stochastic apparent elastic properties can be calculated by equating the order of α, as written in Eq. (6.48) and (6.49), respectively:

$$(\boldsymbol{D}^{\boldsymbol{H}}{}_{I_j})^0 = \frac{1}{|\hat{Y_{I_j}}|}\int_{\hat{Y_{I_j}}} \boldsymbol{D}^0\, d\hat{Y_{I_j}} - \frac{1}{|\hat{Y_{I_j}}|}\int_{\hat{Y_{I_j}}} \boldsymbol{D}^0\boldsymbol{B}\boldsymbol{\chi}^0\, d\hat{Y_{I_j}} \quad (6.48)$$

$$(\boldsymbol{D}^{\boldsymbol{H}}{}_{I_j})^1 = \frac{1}{|\hat{Y_{I_j}}|}\int_{\hat{Y_{I_j}}} \boldsymbol{D}^1\, d\hat{Y_{I_j}} - \frac{1}{|\hat{Y_{I_j}}|}\int_{\hat{Y_{I_j}}} (\boldsymbol{D}^0\boldsymbol{B}\boldsymbol{\chi}^1 + \boldsymbol{D}^1\boldsymbol{B}\boldsymbol{\chi}^0)\, d\hat{Y_{I_j}} \quad (6.49)$$

Each order of $\boldsymbol{D}^{\boldsymbol{H}}{}_{I_j}$ is applied to Eqs. (6.6) and (6.7), in order to obtain the expected value of and variance in the apparent elastic properties.

The Young's modulus of bone tissue E^0 was set to 10 GPa (Rho *et al.*, 1993; Nicholson *et al.*, 1997; Hou *et al.*, 1998) and 0.4 of a Poisson's ratio. A periodic boundary condition was applied to the ROI in order to eliminate possible errors due to boundary condition setting (Ladd and Kinney, 1998). The fluctuation of the *c*-axis orientation that was denoted by α was assumed to be in normal distribution with a zero mean value and variance of 0.03^2. The value of coefficient of variance was recommended to be below 0.1, in order to maintain accuracy by using the approximation of perturbation method (Kaminski and Kleiber, 2000).

6.5 Influence of morphological differences

The influence of morphological differences and fluctuations in the *c*-axis of BAp crystallite orientation on the dispersion of apparent Young's modulus $\hat{E^H}$ in axes 1, 2, and 3 of ROI H1 is shown in Fig. 6.5. The error bar indicates the standard deviation of the apparent Young's modulus. Stiffness was increased with respect to minor change increments in the image-based modeling treatments. The increment rate of $\hat{E^H}$ appeared greater for the dilation-erosion process than for the voxel-edge process. $\hat{E^H}$ at I_8 was increased by almost 50% compared to I_1 in all axes. It was noted that the expected value of $\hat{E_3^H}$ was almost four times greater than $\hat{E_1^H}$ and three times more than $\hat{E_2^H}$ for all $\hat{I}$'s. In the same manner, Fig. 6.6 shows the effect of $\hat{I}$ on variations in the apparent shear modulus for $\hat{G_{23}^H}$, $\hat{G_{31}^H}$, and $\hat{G_{12}^H}$. A similar pattern to the apparent Young's moduli was found in the apparent shear moduli. $\hat{G_{23}^H}$ exhibited the highest apparent shear modulus of the present ROIs. Conversely, the apparent Poisson's ratio $\hat{\nu^H}$ was not sensitive to changes in morphology, as shown in Fig. 6.7, and although $\hat{\nu_{32}^H}$ shows some increments with respect to changes to $\hat{I}$, the value is relatively very small.

The apparent elastic moduli of vertebral trabecular bone are predicted stochastically when uncertainties regarding trabecular bone stiffness orientation and image-based modeling are considered. It appears that the apparent elastic properties of trabecular bone are sensitive to image processing, even though only minor adjustments were performed in the trabecular bone model. Similar findings may have been reported in the past, such as the effect of image threshold (Hara *et al.*, 2002; Yan *et al.*, 2012), noise, and resolution (Rajapakse *et al.*, 2009a) on trabecular stiffness, but the image-based modeling steps that are introduced here are intended to compensate for the connectivity of the trabecular net-

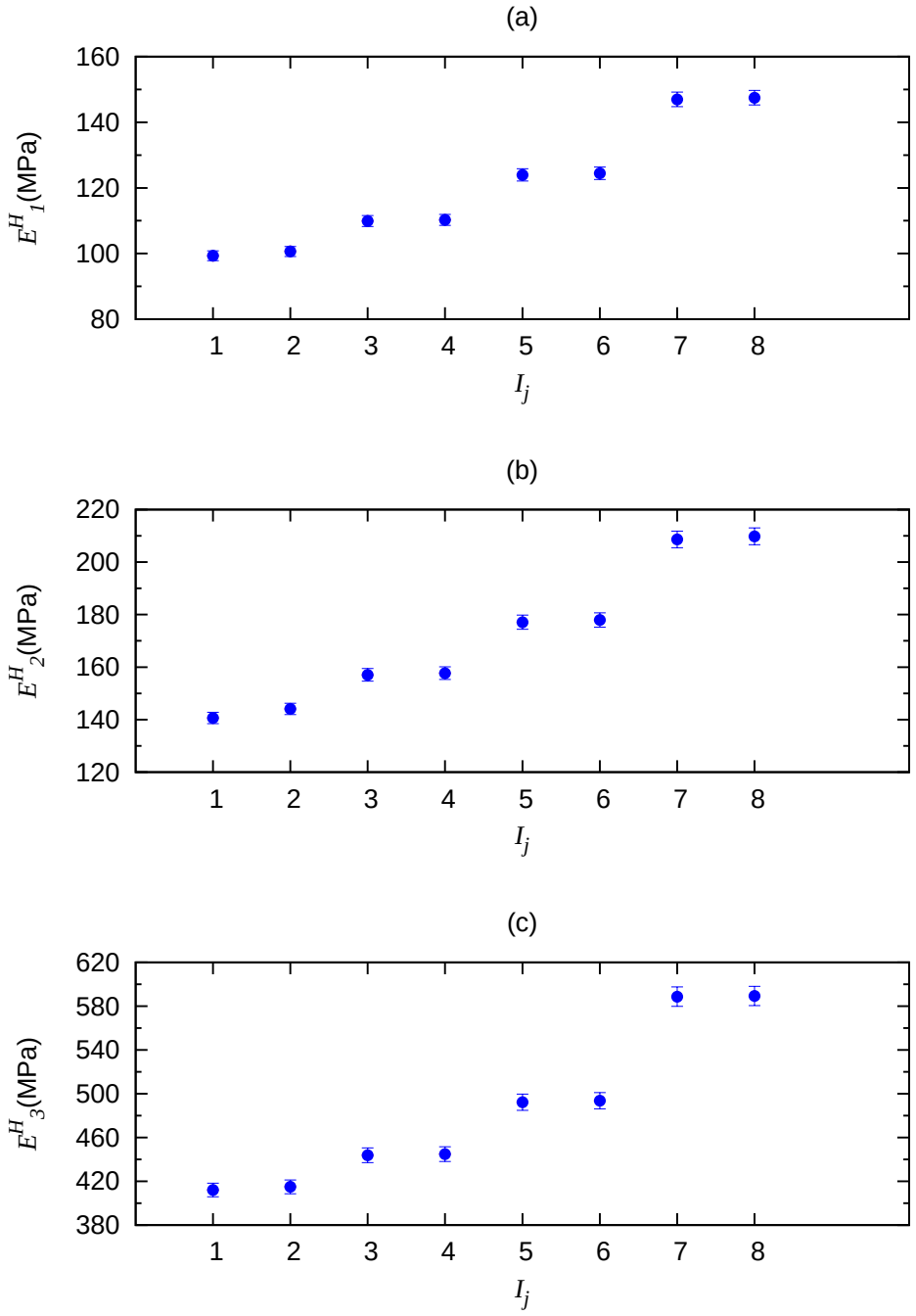

Figure 6.5: Influence of morphological differences due to image-based modeling treatments on the stochastic apparent Young's moduli for ROI H1. Error bar indicates the standard deviation.

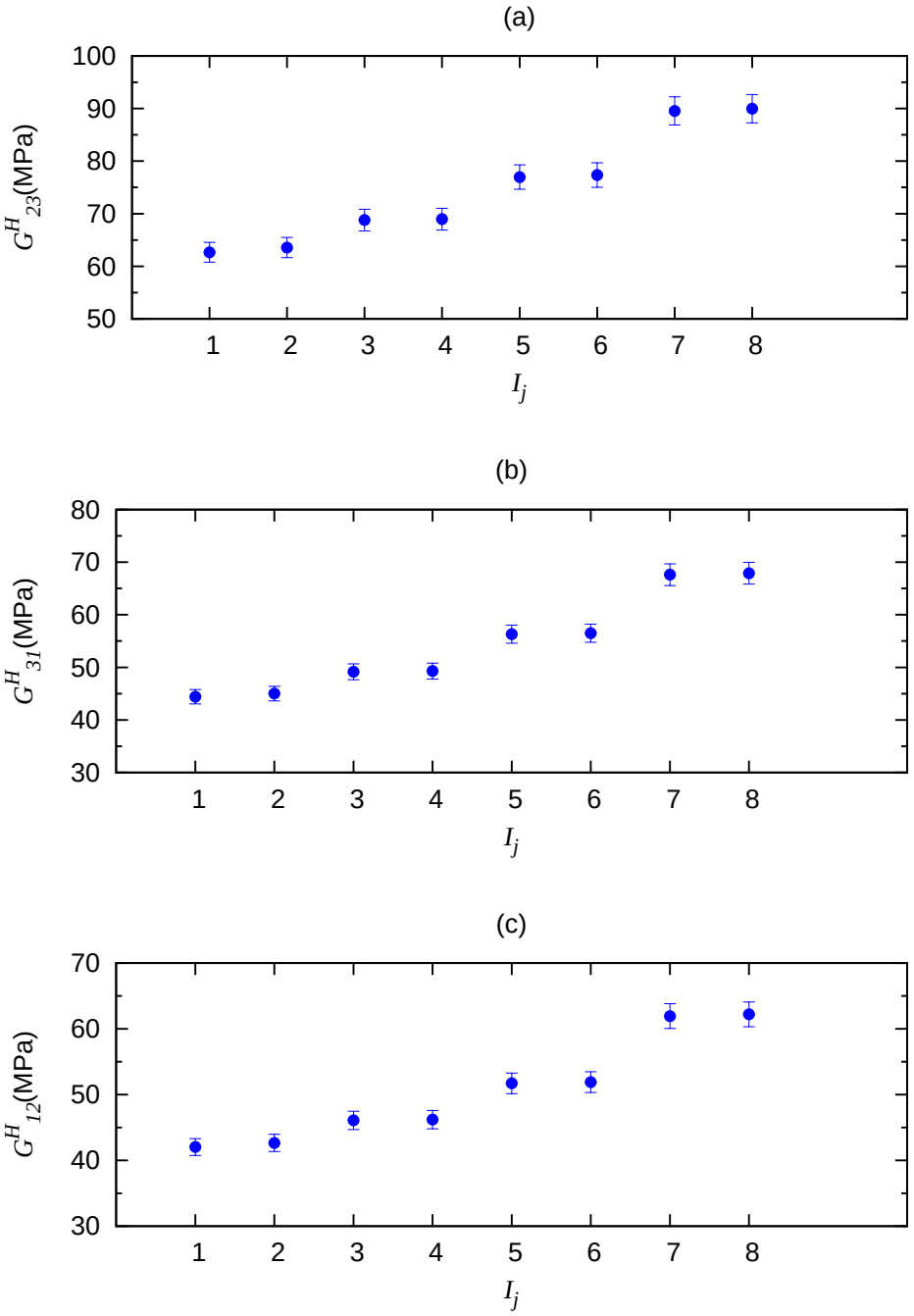

Figure 6.6: Influence of morphological differences due to image-based modeling treatments on the stochastic apparent shear moduli for ROI H1.

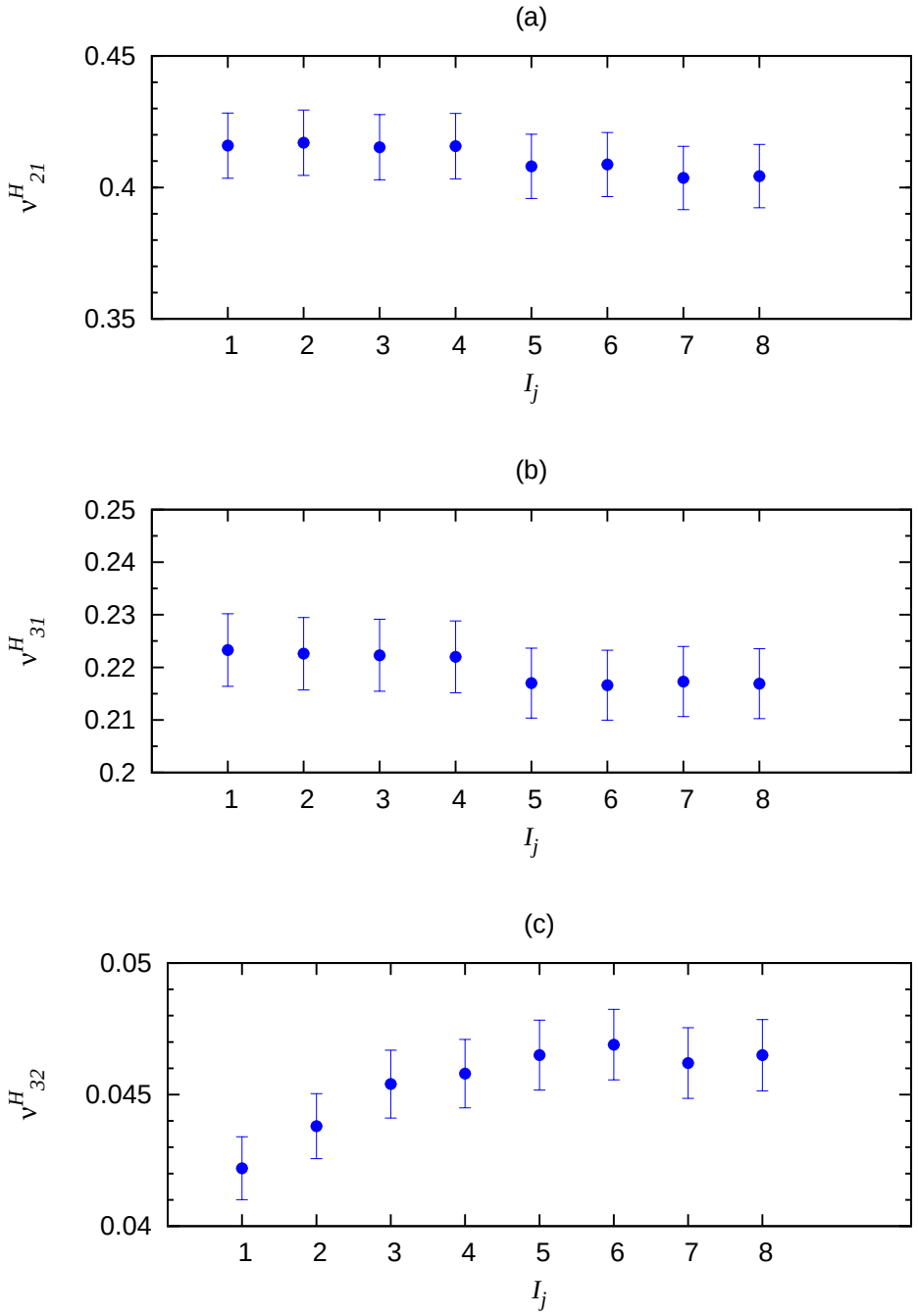

Figure 6.7: Influence of morphological differences due to image-based modeling treatments on the stochastic apparent Poisson's ratio for ROI H1.

work that may break or disappear due to uncertainty in the image-processing procedure, especially for the case of thin trabecular struts. Our result suggests that even a minor improvement to connectivity increases the apparent stiffness of trabecular bone, which is consistent with other literatures (Kinney and Ladd, 1998; Kabel *et al.*, 1999). However, the effect of trabecular stiffness orientation fluctuations on the apparent elastic moduli is barely visible when observing standard deviation in the present result (Figs. 6.5 to 6.7). This is because of the limitation of a first-order perturbation method, where the random fluctuation of α should be small and the coeffient of the variation of the random input variable is recommended to be lower than 0.1 (Kaminski, 2009). However, approximation using a first-order perturbation can obtain an accurate result for the Young's modulus variation, but estimations using the Poisson's ratio variation require higher order expansions (Sakata *et al.*, 2008). Sakata *et al.* (2008) reported that higher order approximation does not always improve the accuracy of stochastic estimations, especially for Young's moduli that exhibit variations (Sakata *et al.*, 2008). Therefore only the Young's modulus was assumed to have any form of fluctuation due to the uncertainty surrounding *c*-axis BAp crystallite orientation in the present study.

According to the results (Figs. 6.5 through 6.7), small fluctuations in uncertainty parameters at the micro-scale level disperse apparent elastic moduli. Variations in the estimated result might be increased if other uncertainty factors are considered. For instance, the scattering of the mean value of the apparent Young's modulus in the vertical axis shown in Fig. 6.5(c) is only due to morphological differences utilized by image-based modeling treatments. A comparison of this result with the mean values of seven other experimental results (Linde and Hvid, 1989; Odgaard and Linde, 1991; Linde *et al.*, 1992; Keyak *et al.*, 1994; Morgan *et al.*, 2003) for the same bone density shown in Fig 6.8 affirms

Table 6.3: Other published experimental results on the estimation of the apparent Young's modulus of trabecular bone in the principal axis.

No	Authors (Ref.)	Anatomic site	$E = f(\rho)$[a]	r[b]	Density type
1	Hvid *et al.* (1989)	tibia	$2132\rho^{1.46}$	0.78	dry
2	Linde and Hvid (1989)	tibia	$10256\rho^{2.5}$	0.92	dry
3	Odgaard and Linde (1991)	tibia	$23500\rho^{2.1}$	0.85	ash
4	Linde *et al.* (1992)	tibia	$4778\rho^{1.99}$	0.89	dry
5	Keyak *et al.* (1994)	tibia	$33900\rho^{2.2}$	0.92	ash
6	Kopperdahl and Keaveny (1998)	vertebra	$2350\rho^{1.2}$	0.93	dry
7	Morgan *et al.* (2003)	vertebra	$4730\rho^{1.56}$	0.93	dry

[a]Young's modulus E in MPa and apparent density ρ in g/cm^3
[b]correlation coeffcient of regression equation

that scattering normally happens when predicting apparent trabecular bone properties. The mean value of experimental results was calculated from the regression equation listed in Table 6.3. For a certain bone density, Fig. 6.8 shows the eight plots of the present result are predicted within the range of the highest and lowest experimental results. Obviously, scattering could be the result of inter-individual differences.

6.6 Uncertainty parameter β

In general, variations in trabecular bone characteristics correlate with inter-individual differences. In order to estimate reliable apparent mechanical properties, for instance when considering multiple ages and genders for a certain bone density, a huge amount of tests are required. Even with these tests it is difficult to obtain the same bone density from different individuals. Therefore, the uncertainty parameter β is introduced in the present approximation, in order to characterize the dispersion of the prediction caused by inter-individual differences, besides unknown factors and miscellaneous errors, which are

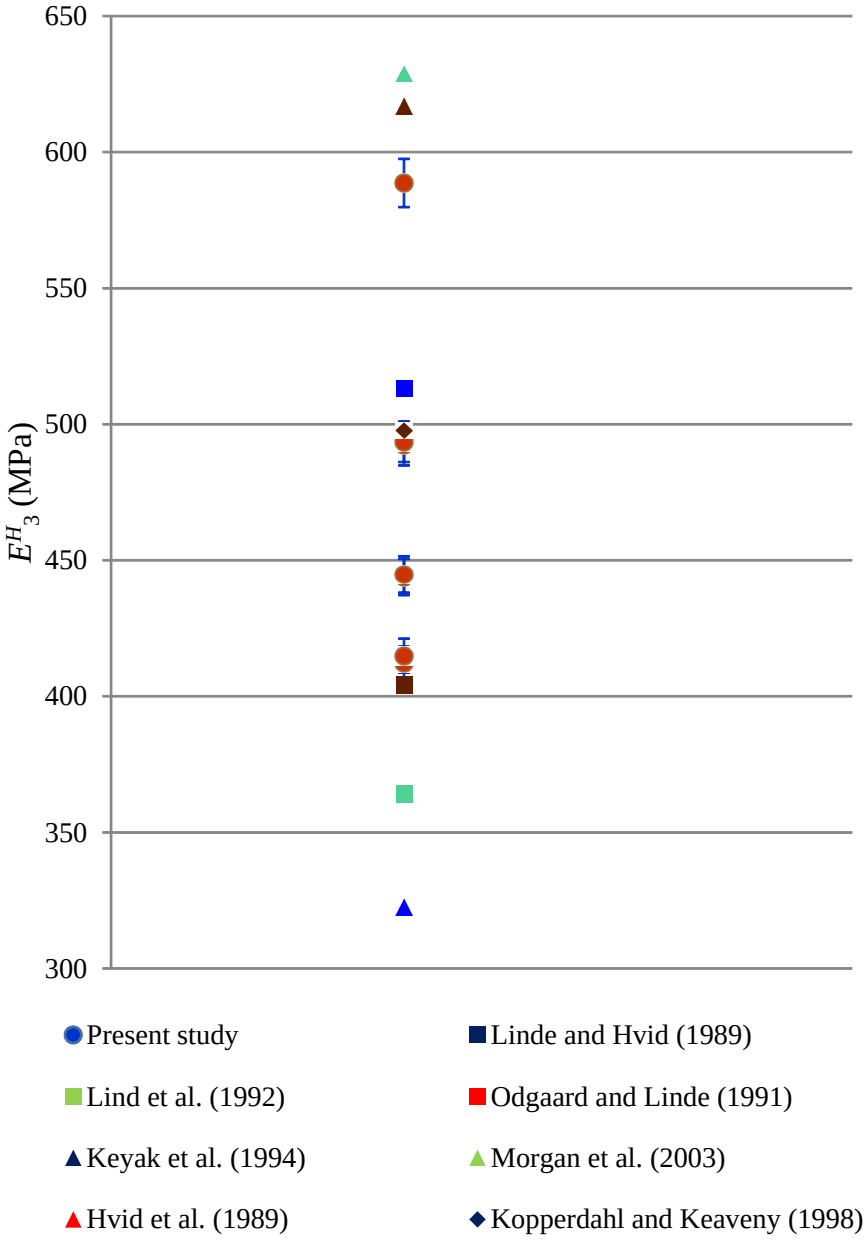

Figure 6.8: Scattering plots due to morphological differences and experimental results.

possibly generated due to uncertainty in the experimental work. Hence, $\hat{\boldsymbol{D}^{\boldsymbol{H}}}$ in Eq. (6.8) is updated and rewritten as follows:

$$\hat{\boldsymbol{D}^{\boldsymbol{H}}} = \mathcal{F}\left(\hat{\boldsymbol{\chi}}(V, A, \hat{I}), \hat{\boldsymbol{D}}(\alpha), \beta\right) \tag{6.50}$$

where $\hat{\boldsymbol{D}^{\boldsymbol{H}}}$ in perturbation form is calculated approximately as Eq. (6.51).

$$\hat{\boldsymbol{D}^{\boldsymbol{H}(\boldsymbol{\beta})}}_{I_j} = \left(\boldsymbol{D^H}_{I_j}\right)^0 + \beta\left(\boldsymbol{D^H}_{I_j}\right)^1 \alpha \tag{6.51}$$

β is defined as a scalar value and is multiplied by the stochastic part of $\hat{\boldsymbol{D}^{\boldsymbol{H}}}$ to represent the magnification of the fluctuation caused by inter-individual differences, unknown factors, and miscellaneous errors. The value of β is determined by fitting it to existing reliable experimental results as listed in Table 6.3. By assuming that the highest and lowest mean values from the experimental results represent the upper and lower bounds of tail probability, β is calibrated when the predicted probability density function (PDF) covers all seven experimental results.

Considering uncertainty in image-processing $\hat{I}$, all 3D models in Table 6.2 can be generated practically. If all models are considered and the probability of each $\hat{I}$ (PrI) is dependent on probability density function f, then Eq. (6.52) should hold:

$$\int_{\hat{I}} f(\hat{I})\, d\hat{I} \approx \sum_{j=1}^{8} PrI_j = 1 \tag{6.52}$$

where j indicates the jth number of image processing procedures in Table 6.2. Thus, a unique solution considering all possible 3D models can be obtained by applying Eq. (6.52). By assuming that $f(\hat{I})$ is in normal distribution and each PrI stands for a unit interval

I_j	PrI
1	0.002
2	0.021
3	0.136
4	0.341
5	0.341
6	0.136
7	0.021
8	0.002

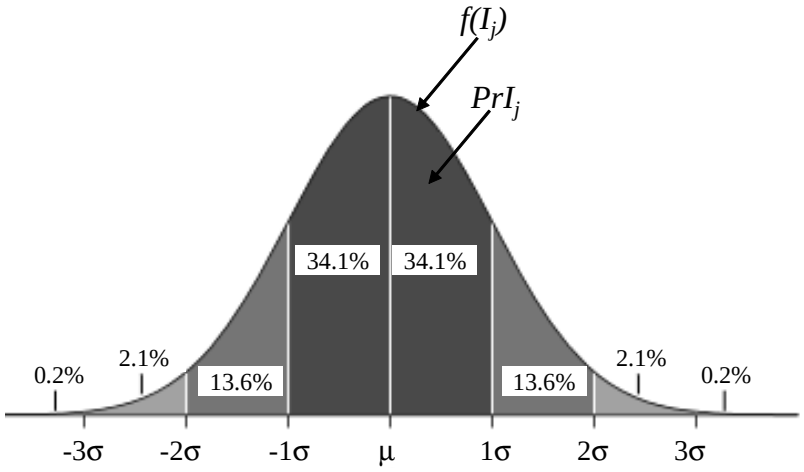

Figure 6.9: Probability of image-based models (PrI).

α, each PrI can be computed by using the empirical Gaussian normal distribution rule, as shown in Fig. 6.9. A further explanation on the setup of PrI is described in Appendix B.

Finally, the effective apparent elastic moduli considering all $\hat{Y}_{I_j}$ is computed using a Gaussian mixture model, as formulated in Eq. (6.53), by multiplying Eq. (6.51) with the probability of $\hat{I}$ in Fig. 6.9.

$$\boldsymbol{D}^{\hat{\boldsymbol{H}}} = \sum_{j=1}^{8} (PrI_j)\, \boldsymbol{D}^{\hat{\boldsymbol{H}}(\boldsymbol{\beta})}{}_{I_j} \tag{6.53}$$

The implementation of the present uncertainty modeling is summarized in the flow diagram shown in Fig. 6.10. The effective apparent elastic moduli of trabecular bone, considering the uncertainties of the c-axis of BAp crystallite orientation and image-based modeling, were computed using the proposed stochastic image-based multi-scale method.

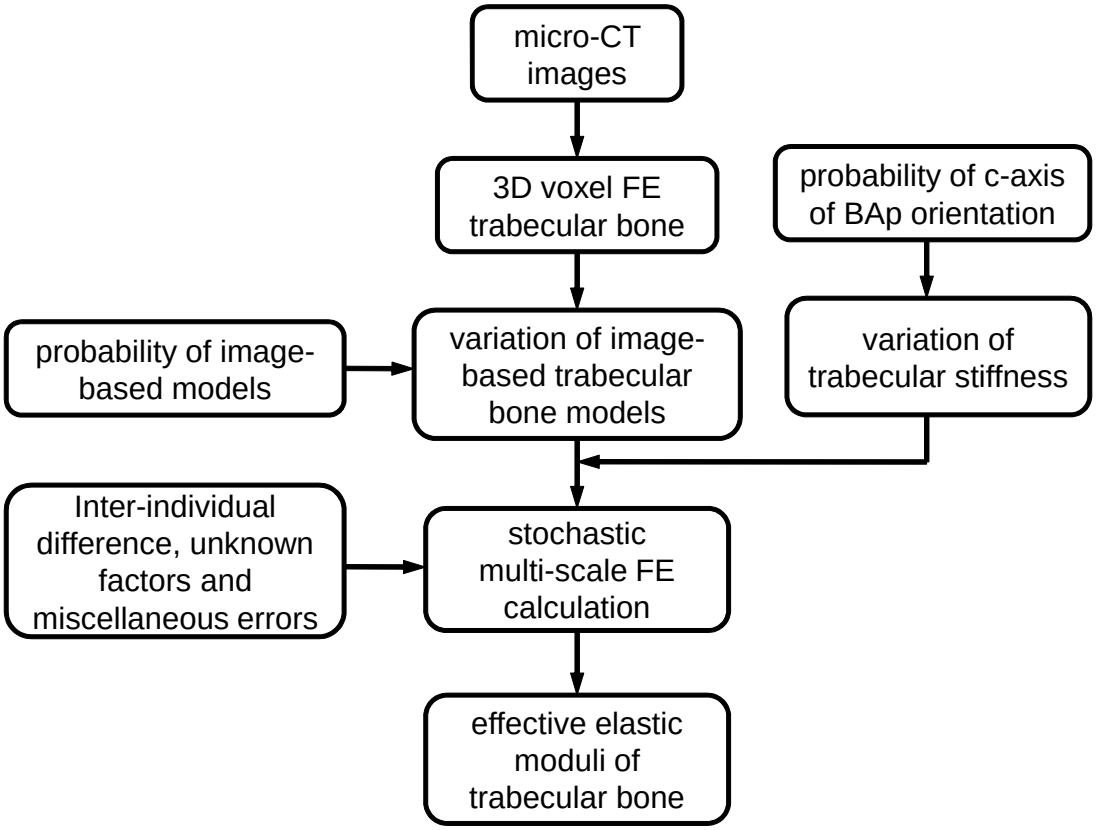

Figure 6.10: A flow diagram of uncertainty modeling.

6.7 Calibration of uncertainty parameter β

Figure 6.11 shows the predicted probabilistic density of the effective Young's modulus in the vertical axis ($\hat{E_3^H}$) of the O1 (osteoporotic No. 1) model, considering uncertainty in the bone characteristics, experimental works, and image-processing for β=6, 8, and 10. The obtained probability density is not in strict normal distribution, but it is close. The mean values (based on the regression equation) of other published experimental results are also plotted in Fig. 6.11. The results obtained by Keyak *et al.* (1994), which is now most frequently referred to in many studies, were found to roughly match the mean values of our predicted result for all selected β.

In the same manner, Figs. 6.12 and 6.13 show the predicted PDF of $\hat{E_3^H}$ for the H1 and H2 (healthy No. 1 and No. 2) models, respectively. Conversely, Keyak et al.'s result was plotted in the tail part of our predicted probability density, but all of the experimental results were located within the bounds of our prediction for β=8 and 10. When β is smaller than 6, the predicted PDF cannot cover the mean values of the seven references. Even when β= 6, the lower and upper bounds of their scattering are not covered fully. In this sense, β >6 are appropriate. Note that the probability of the mean value is not a matter of concern in this study, but the coverage of seven references in the tail probability is emphasized nevertheless. One problem is that possible errors in the experiments cannot be eliminated, especially considering that they were performed by medical doctors who ordinarily do not specialize in mechanical testing. When comparing the PDFs for β= 6, 8, and 10, there is only a slight change in the expression of tail probability. Therefore, it is concluded that β more than or equal to 8 is appropriate in order to give a meaningful prediction regarding the mechanical properties of healthy bones.

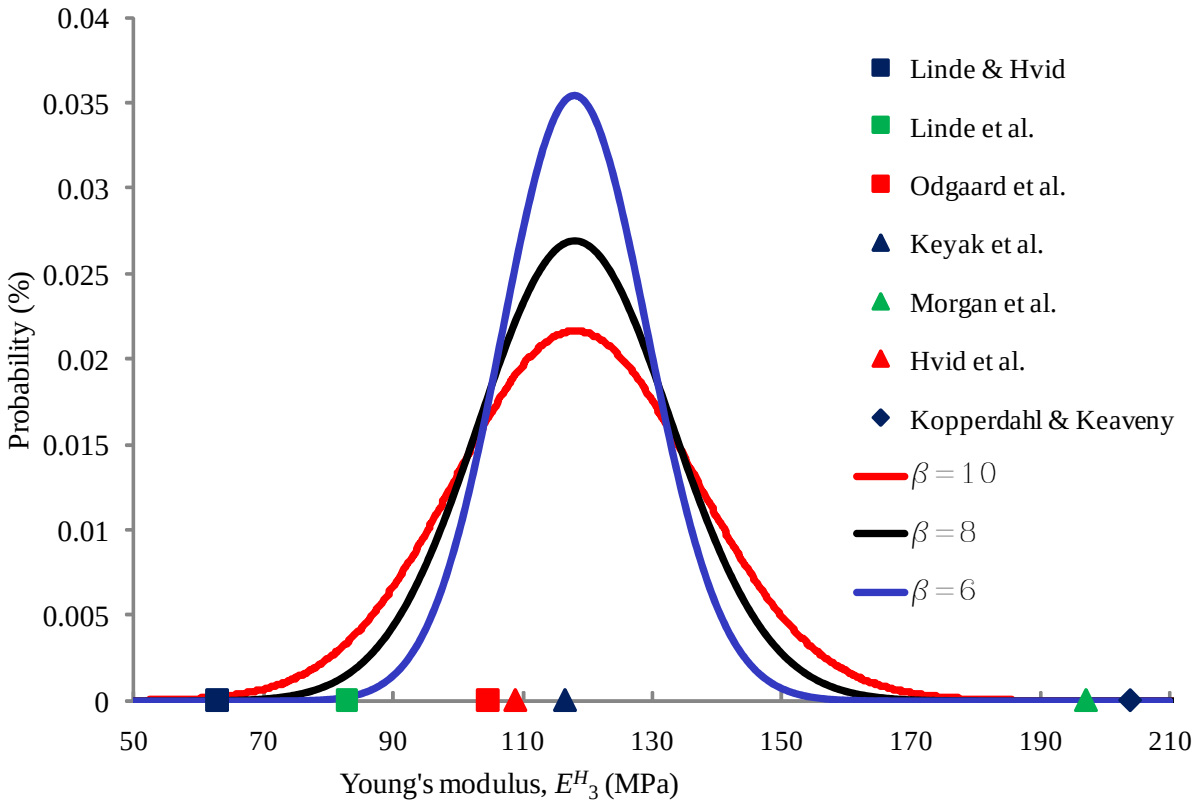

Figure 6.11: Predicted probabilistic density of the effective stochastic apparent Young's modulus in the vertical axis of the O1 model.

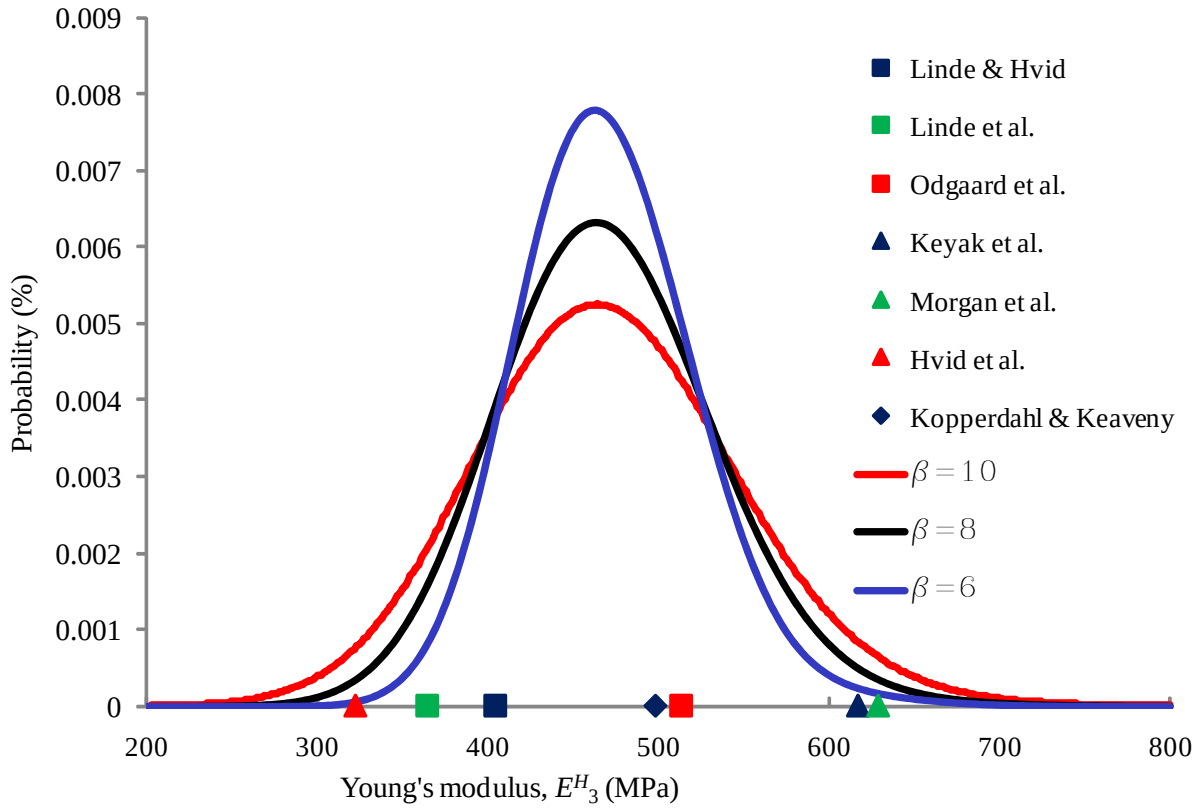

Figure 6.12: Predicted probabilistic density of the effective stochastic apparent Young's modulus in the vertical axis of the H1 model.

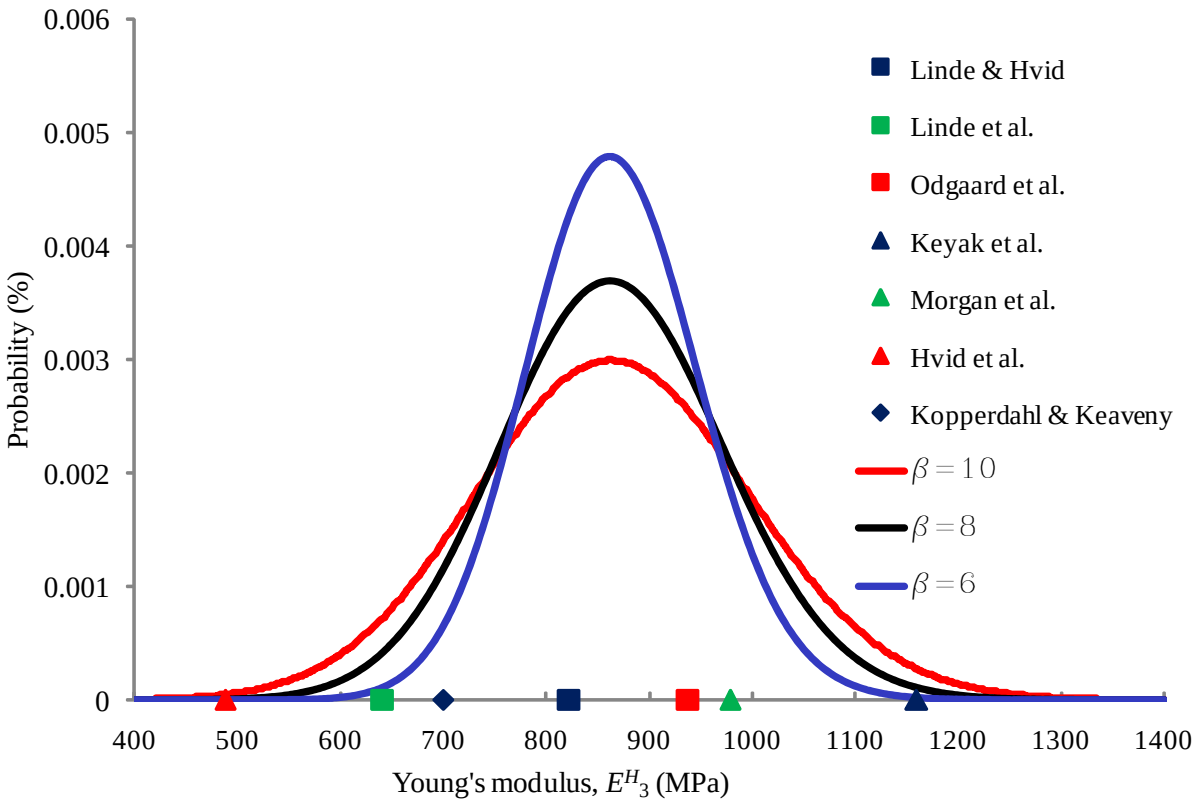

Figure 6.13: Predicted probabilistic density of the effective stochastic apparent Young's modulus in the vertical axis of the H2 model.

For the case of β=8, the mean value of $\hat{E_3^H}$ was found at approximately at 118, 462 and 860 MPa for O1 with an equivalent bone density of 0.075 g/cm^3, H1 (0.162 g/cm^3), and H2 (0.215 g/cm^3), respectively. The results suggest that the bounds of the predicted result were increased with respect to an increase in equivalent bone density. It is interesting, however, that the probabilistic simulation implies that the effective properties are not always a function of bone density only. This fact is recognized as the effect of bone quality, which is another factor, as well as bone density, which contributes to bone strength (Hernandez and Keaveny, 2006). Variations in bone tissue properties and the microarchitecture of trabecular bone, which were considered in this study, could represent the characterization of bone quality. Our results indicate the existence of this factor in determining effective mechanical properties. Hence, the proposed method may provide new insights into understanding bone characteristics.

6.8 Predicted results and discussion

A comparison was made with respect to the equivalent bone density proposed by Keyak *et al.* (1994). The experimental result performed by Keyak *et al.* (1994) has been used widely for comparison with finite element analysis. Next, the predicted results for β=8 were plotted against the experimental results proffered by Keyak *et al.* (1994) in Fig. 6.14. It appears that our result for the lower bone density (O1) case has very good agreement with the regression curve of Keyak et al.'s result, whereas our results are close to the lower bound of Keyak et al.'s result for their high bone density (H1 and H2) cases. Recalling the original experimental plot in Fig. 4.5, however, only a few experimental results existed for the high bone density region, especially for more than 0.15 g/cm^3. Also, remembering that

our prediction for H1 and H2 were in very good alignment with many other experimental results, as shown in magnified view of Fig. 6.14, it would be natural to say that a very small number of experimental results by Keyak et al. were insufficient in obtaining a reliable regression curve in the high bone density region. In other words, our results suggest that the regression curve by Keyak et al. overestimates real effective properties. It is hard to identify the reasons for this result, but they are expressed in our theory by parameter β. Moreover, it is found that the width of the present probabilistic distribution result almost same as the bounds on Keyak's experimental plot. Hence, by using only three cadavers, the proposed stochastic model was successfully simulated the widespread scattering of experimental result mainly due to inter-individual differences.

On the other hand, the mean value provided by the regression equation of other experimental results (as listed in Table 6.4) does not describe the real behavior of the measured value. Difficulty may lie in predicting a reliable apparent elastic modulus with respect to certain bone densities from the greatly dispersed results obtained from the experiment, as illustrated in Fig. 4.5. The reliability of the experimental result is not a matter of concern in this case, but an improved evaluation procedure should be considered rather than a regression equation, in order to give a meaningful prediction of trabecular stiffness with respect to bone volume fraction. For instance, our estimation result in probability density form is able to give a guideline to evaluate the measurement data. The distribution curve could be represented as a weight or as a percentage of the reliability of the measured value. The measured value nearest to the mean value should have more weightage than the value near to the upper and lower bounds.

The present method provides an additional insight into predicting more reliable apparent elastic moduli of trabecular bone, since as many uncertainty parameters as possible

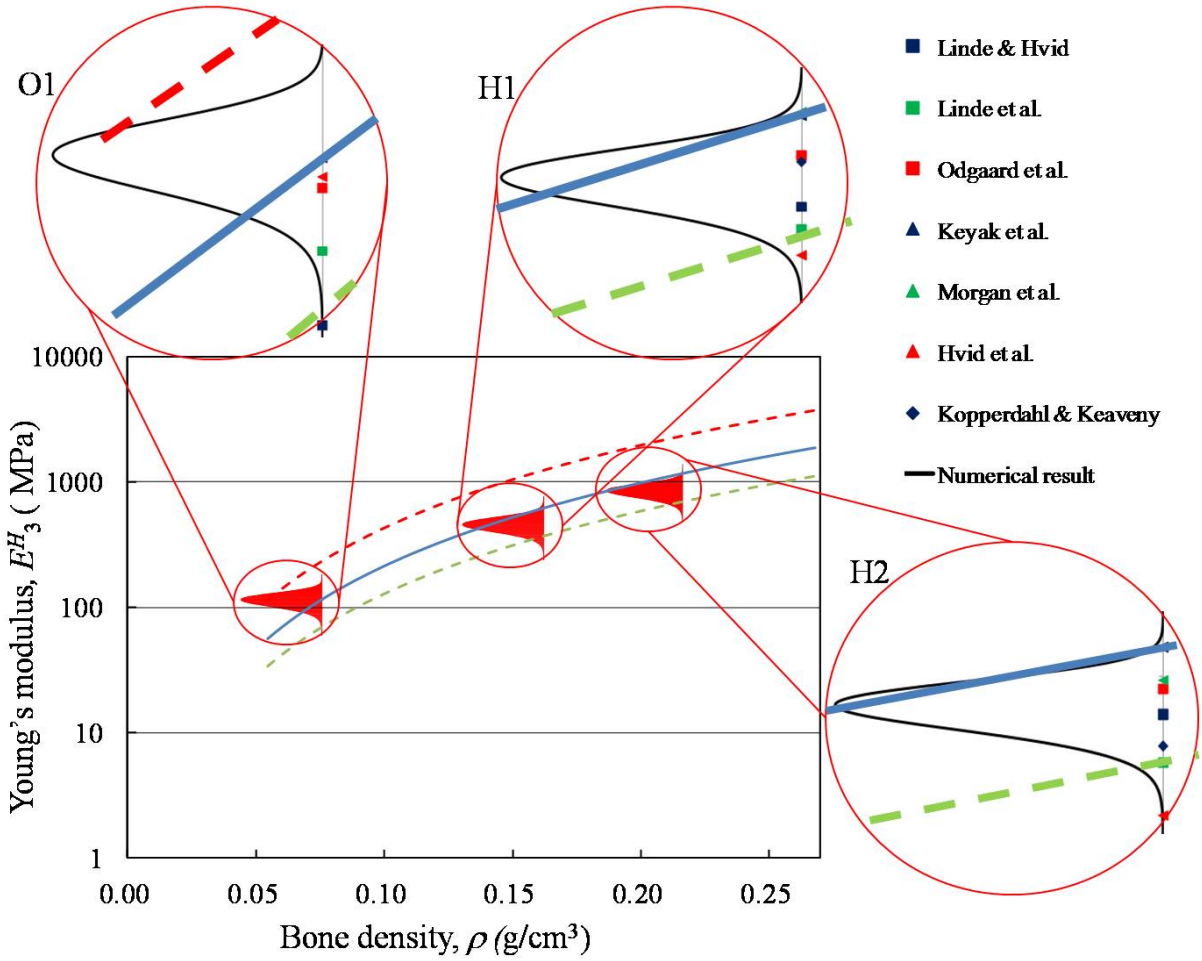

Figure 6.14: Comparison with the scattered experimental results by Keyak et al.

were taken into account. Other possible errors that have been commonly highlighted in previous studies, such as discretization (Ulrich *et al.*, 1998), boundary conditions (Ladd and Kinney, 1998), and ROI size (Choi *et al.*, 1990), are minimized in this study. Chevalier *et al.* (2007) reported that a voxel-based FE with a size of 30-45 μm^3 is an appropriate level for linear elastic analysis, and this was validated through the results of mechanical tests and nano-indentation. Although discontinuity occurs quite readily at trabecular strut boundaries, due to the shape of the voxel elements, the use of a voxel edge process in the present method improved the smoothness of the trabecular geometry. Errors caused by boundary conditions in numerical modeling were eliminated when the periodic boundary condition (as opposed to the asymptotic homogenization theory (Hollister *et al.*, 1991)) was applied. The ROI was also carefully selected to hold periodicity by using a specific computational tool (DoctorBQ), and the size satisfied the requirements of the appropriate numerical test (Harrigan *et al.*, 1987).

The main purpose of the present stochastic model is to ensure the trustworthiness of the apparent elastic moduli estimation related to the morphology of the trabecular network described in Chapters 4 and 5. Although the reliability of the prediction focused on the Young's modulus in the vertical axis, it could also be applied to the other eight parameters of orthotropic material. For instance, according to stochastic apparent elastic properties with respect to image-processing results (Figs. 6.8 to 6.10), the scattering pattern and the bounds of variation are similar for each physical quantity (Young's moduli, shear moduli, and Poisson's ratio). We expect that a similar result could be obtained for other apparent elastic moduli, besides $\hat{E_3^H}$. Predicting the present stochastic apparent elastic moduli is based on the stochastic multi-scale method, which provides the mean value and its variance. The mean value of the predicted result was found to agree reason-

ably with the mean value of the experimental results provided by many researchers (Figs. 6.11 through 6.13). Hence, the apparent elastic moduli calculated using multi-scale theory in the previous chapters, which correspond to the mean value of the stochastic apparent moduli, are sufficient to hold the reliability of the estimation.

In this study, uncertainty factors were handled in a systematic manner and the predicted results were verified with experimental results, to ensure the credibility of the present computational modeling. Through further discussion on a comparison with the data provided by Keyak *et al.* (1994), our numerical results may be able to update the reliability of the regression curve, even in a region with a few experimental results. That is, the proposed method is useful for predicting variations in effective properties by extrapolating the calibrated case against another case without experimental results. Also, it should be noted that very widespread scattering, due mainly to inter-individual differences, could be estimated by employing the proposed theory. In the case of many composite and porous engineering materials, the scattering of experimental data is not as great as for human bone. Therefore, the proposed model has a certain of degree of potential for application to many engineering materials with random microstructures. Also, in the numerical design of the microstructure for the emergence of desired macroscopic properties, the use of stochastic simulation is expected to solve the mismatch between the numerically designed microstructure and the fabricated one, by updating reliability by changing parameter β using appended experimental data.

6.9 Summary

The stochastic computational method was presented in this study to estimate variations in apparent the elastic moduli of vertebral trabecular bone by considering uncertainties caused primarily by trabecular stiffness orientation and image-based modeling. The apparent elastic moduli were found to be sensitive to morphological differences in the trabecular bone network influenced by image-based modeling treatments. The apparent elastic modulus was increased with respect to minor improvement in trabecular connectivity. The reliability of the prediction was improved by introducing uncertainty parameter β to represent various bone characteristics as the result of inter-individual differences, unknown factors, and miscellaneous errors in experimental work. The predicted results showed good agreement with the mean values of widely scattered experimental facts offered by many researchers. Our numerical results suggest that the regression curve obtained by Keyak *et al.* (1994), which has been referred to frequently, overestimates effective properties in the high bone density region, because the number of measured data is not sufficient. In short, the reliability of the mean value obtained using the deterministic homogenization method to describe trabecular morphology in the previous chapters has been proven by the present stochastic results. Moreover, the present stochastic model was successfully simulate the widespread scattering of experimental result by using only three bone specimens in order to represent the variation due to inter-individual differences. In future, we expect that the proposed method will be used as an extrapolation technique from one verified case to another case without measured data. Since a general theoretical framework was proposed in this chapter, it may also be applicable to a variety of composite and porous engineering materials.

Chapter 7

Conclusion

7.1 Findings

Trabecular bone morphology plays a key role in determining apparent bone stiffness, besides bone density. The connectivity and microarchitecture of a trabecular network appear to influence load-bearing capability and contribute to optimal stiffness and strength per trabecular bone mass. Obviously, the major difference between healthy and osteoporotic bones is the bone volume fraction, but the differences among them in trabecular morphology are also essential factors that determine apparent bone properties. When observing apparent elastic moduli using the homogenization method, healthy bone was found as being transverse-isotropic on the left-right and post-ant axes, whereas osteoporotic bone showed anisotropy. Even the degree of anisotropy increased for osteoporotic bone rather than healthy bone when we observed the ratio of lateral shear moduli with respect to the vertical shear moduli for both bone cases. The redundancy of trabecular morphology along the cross-section of regions of interest (ROIs) for healthy bone could be found easily

and contributed to the mechanical properties.

Trabecular bone stiffness is not always a function of bone density. Both Keyak et al.'s experimental result and ours proved this fact via the plot of the Young's modulus with respect to bone density. Bone microarchitecture determines the degree of effectiveness in load distribution among trabecular networks and consequently influences the stiffness of bone properties. About 40% to 50% of a healthy trabecular network is oriented almost in a vertical (principal) direction, also known as primary trabecular bone, whereas about 30% of that is secondary trabecular bone, which is almost in a lateral (left-right and post-ant) direction. The primary bone mainly supports self-weight, but half of it also supports loads in a lateral direction. The secondary bone supports the primary bone and is also used as part of the load path network for all loading directions. The percentage of secondary bone in osteoporotic bone decreases compared to healthy bone. The volume of secondary bone is only about 20% to 30% of the total volume of interest, whereas about one-third of an osteoporotic trabecular network is primary bone. This fact also contributes to the anisotropic behavior of osteoporotic bone.

Not all trabecular struts in trabecular network play a role in the load-bearing capability, as it is dependent on orientation, connectivity, and geometry. The primary and secondary bones are defined as trabecular structures involved as pathways for load distribution. A decrease in primary and secondary bones in osteoporotic bone reduces the flexibility of load transmission in the trabecular network, resulting in the weakening of apparent bone properties. The effectiveness of load transmission is enhanced by the existence and orientation of trabecular struts, called plate-like bone and interconnected rod-like bone. Plate-like bone participates in the construction of a systematic network system, and it is presumed to function as a hub in the trabecular network system to

transfer the load to connected rod-like bones. Morphology with sufficient plate-like bone is redundant so the load can choose other pathways even if some hubs of the network are missing. A decrease in plate-like bone in the trabecular microstructure can cause the whole network system to become brittle, which leads to an increase in fracture risk in osteoporotic bone with the additions of stress concentration by the thinning of each trabecular strut.

Trabecular morphology is a complex, disordered microstructure with random characteristics at the tissue level because the bone remodeling process, morphology, mineralization, and biological apatite (BAp) crystallite conditions change, and these changes affect the stiffness of trabecular bone tissue. Inconsistencies in mineral content and the *c*-axis orientation of BAp crystallite cause the anisotropy of trabecular bone tissue. Uncertainties arise not only in the tissue level, but also in measurement procedures or modeling processes when evaluating apparent bone mechanical properties. Errors in measurement due to inaccuracies regarding specimen preparation, experimental set-up, and data collection are difficult to eliminate, and even in some cases they remain classified as 'unknown factors'. Since there is no standard procedure on how to measure apparent trabecular bone properties, the results obtained from many experimental works are wide and highly variable. Even in the computational modeling of trabecular bone from micro-computed tomography (micro-CT) images, inconsistency happens during image-processing, such as when determining the threshold of a binary image and the existence of artifacts and noise. Minor improvements to the connectivity of trabecular networks due to image-based modeling procedures could increase apparent elastic properties dramatically.

A stochastic computational model was developed to predict the apparent elastic moduli of trabecular bone by considering uncertainties. This probabilistic simulation

model recognized the fact that 'bone quality', together with bone density, is an important determinant of bone stiffness. Variations in bone tissue properties and the morphology of a trabecular network due to fluctuations in c-axis BAp crystallite orientation and image-based modeling parameters, respectively, could represent the characterization of bone quality. Furthermore, miscellaneous errors or unknown factors that arise from experimental work in the evaluation of trabecular bone stiffness could contribute to the dispersal of the predicted elastic moduli. Inter-individual differences may magnify the scattering of the estimation, however, so predictions based on the apparent elastic moduli of trabecular bone from a stochastic standpoint improve reliability. Good agreement between the mean value of the stochastic elastic moduli and many other experimental facts verified the trustworthiness of the calculated results in the homogenization method. The uncertainty parameter, named β in this thesis, could characterize unknown factors that influence variations in the predicted elastic moduli. Some parts of the scattering of others' experimental results could be explained by the proposed method. In conjunction with the extrapolation method, β is useful for predicting any variation in apparent elastic properties through comparison with the verified model in a case where there are no experimental results. The present probabilistic model may also be able to update the reliability of the experimental plots for a case where there are fewer data results. It is believed that the method developed here could potentially provide relevant and detailed information about reference points for predicting and evaluating the reliable elastic moduli of trabecular bone.

7.2 List of assumptions and limitations

Some specific assumptions, which were made regarding the present study, should be highlighted because they might be not appropriate for other applications. Below is a list of key assumptions in this study.

1. Setup of c-axis for each voxel in trabecular bone tissue.
2. Setup of random variable α to represent the fluctuation in microscopic properties $\hat{\boldsymbol{D}}$.
3. Assignment of probability of image-based models (PrI) to calculate the apparent elastic moduli.
4. Calibration of uncertain parameter β to predict reliable apparent elastic moduli when considering inter-individual differences.

Details of the above assumptions are also described in Appendices A and B. In addition, there are also a number of limitations associated with this study that should be noted when evaluating the present results. First, only three lumbar vertebra bone specimens from three individuals were investigated, and all the ROIs were harvested from these bones. Since this was a first attempt at using the proposed methods, the limited number of bone specimens and a reasonable number of ROIs were chosen. More emphasis was put on the applicability of the algorithm applied to the apparent stiffness of trabecular bone estimation and the study on variations in trabecular morphology. It may be necessary in the future to apply the present methods to various ROIs features or microarchitectures with different bone volume fractions and to more specimens from various anatomical locations and many individuals, in order to draw more general conclusions. Additional data

derived by using this method may help to propose a unique solution to the coefficient factor as presented in this study. It is believed that the coefficient factor corresponding to inter-individual difference should be a function of bone volume fraction in the future.

Second, this study is limited to linear elastic analysis, since the trabecular bone image was captured from dried bone. The existence of mineralization was therefore neglected. Although tissue mineralization is inhomogeneous and the inhomogeneity is higher in trabecular bone with high porosity, the results of previous studies (Jaasma *et al.*, 2002; Gross *et al.*, 2012) suggest that the effects of inhomogeneous mineralization on the strength of vertebrae are likely to be very small. Third, the setup of the *c*-axis orientation of BAp for each voxel element in the deterministic homogenization analysis was only applicable to the fourth lumbar vertebra and not to other anatomic sites such as femurs and mandibles. The setup was simplified in the present stochastic simulation. Next, fluctuations in microscopic properties (α) and image-based models (PrI) were assumed to be in normal distribution, which was chosen to characterize any fluctuations in our stochastic computational scheme, because no probabilistic experimental results are currently available on bone tissue modulus. It will therefore be of future interest to test the method on various types of probabilistic density functions.

The present probabilistic results for the apparent elastic moduli of trabecular bone depend on the value of random parameter α as input data. The fluctuation of α was decided based on recommended values in the literature (Sakata *et al.*, 2008; Kaminski, 2009). If a slight change in α is introduced, β may need to be calibrated again. We cannot at this stage suggest a unique solution to determine the appropriate β, as its selection might be different from case to case. Finally, in morphology analysis under dynamic loading, our linear computational scheme does not allow for the analysis of trabecular

buckling. The buckling mechanism may be inevitable in the analysis of osteoporotic trabecular bone, but that was not the case in this study. Buckling is not likely to play a role for the unit load that was investigated here, but it may be important when a higher load is applied. For this case, we were not able to simulate any geometrically nonlinear buckling processes. Hence, the present dynamic analysis was used only to visualize the percolation of load transfer and cannot represent real dynamic response in the trabecular microstructure.

7.3 Future works

7.3.1 Dynamic analysis

A study on the morphology analysis of vertebral trabecular bone under dynamic loading was performed based on impact load models in a vertical axis. The loading setup in the dynamic analysis was close to actual conditions, and it is well-known that vertebral trabecular bone mainly supports vertical compression (Mosekilde, 1993; Homminga *et al.*, 2004). However, the results may not be the same if the loading is along the horizontal axis, so it would be interesting to explore the influence of different loading directions. In this case, the size of the ROI in the horizontal direction should be large enough to avoid reflecting a stress wave at the boundary over a short time period. The role of secondary bone in load-bearing capability may be able to be visualized from a different point of view. Because of the use of an explicit algorithm, only dynamic behavior over a very short time was analyzed. In the future, an implicit algorithm should be used instead of an explicit algorithm, in order to analyze vibration behavior, especially for secondary trabecular bone

and non-percolated trabecular bone. Moreover, in order to discuss mechanical responses to dynamic loading, the influence of viscous boundary setting to the side walls of an ROI should be analyzed carefully, although it is not a main issue in the visualization of primary bone.

The present study used homogenization theory to calculate microscopic stress. The unit cell is located an infinite distance away from the actual load of the lumbar vertebra that we studied here. The uniform load is the only choice available when homogenization theory is applied. To set up load conditions in a more realistic manner, the existence of cortical bone, bone marrow, and an intervertebral disc is necessary. Hence, in future, a study of the morphology of trabecular networks under dynamic analysis should be conducted with a variety of loading conditions by also considering cortical bone, bone marrow, and intervertebral discs. The role of trabecular structures and their interaction with bone marrow could be investigated by observing load percolation, as proposed in the present method.

Finally, how trabecular architecture and strut sizes are determined is an open problem in the study of mechano-biology. Moreover, establishing how density is determined is still to be resolved. It is believed that dynamic analysis, but not static analysis, can give a new insight into this open problem. Hence, a study on the effect of different trabecular strut sizes with the same bone density on stress wave propagation (as illustrated in Fig. 7.1) would be a good platform for future work. In order to achieve this objective, an investigation into the speed and reflection of a stress wave in the trabecular network might be necessary.

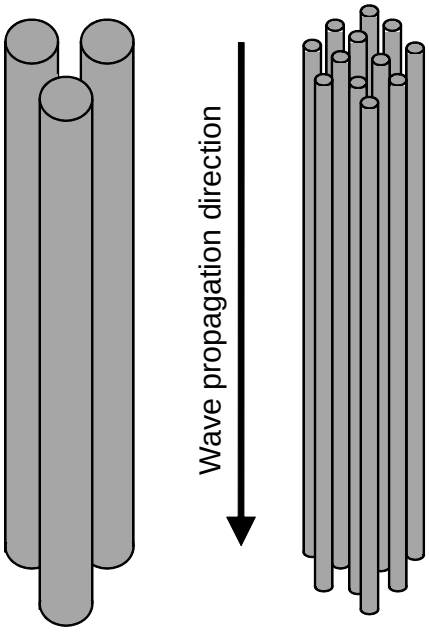

Figure 7.1: Effect of cross-sectional size on wave propagation with the same bone density.

7.3.2 Stochastic homogenization analysis

In the present stochastic homogenization analysis, the c-axis was set in the vertical axis (axis-3) for all voxel elements. Although the results of the mean values of stochastic simulation agree fairly well with the deterministic homogenized properties (as shown in Fig. 4.5), the setup of the c-axis used in the deterministic homogenization method makes the simulation more reliable. Hence, in the future, the c-axis should be set in the same manner as for the deterministic homogenization method, especially when the scattering of properties other than $\hat{E}_3$, such as G, is studied in detail, because the c-axis should be in the longitudinal direction for secondary trabecular bone.

Furthermore, considering fluctuations in microscopic properties other than E, the present stochastic simulation method could potentially be extended for more than one random variable. For instance, in the case of a human mandible, which is subject to

implant surgery, variations in bone tissue properties in G are much more important than in E. Therefore, a stochastic simulation model that can consider more than one random variable and accommodate variations in probabilistic distributions (other than normal distribution) as input data might be useful for other applications in the future.

The stochastic computational method proposed in this thesis and used to predict the apparent elastic moduli of trabecular bone is suitable for human vertebrae. It is easy to extend the method to other anatomical sites such as the femur, tibia and femoral neck, in order to obtain reliable predictions regarding apparent mechanical properties. However, in the case of, for instance, a human mandible, experimental data on apparent mechanical properties is extremely rare. As such, dentists may face difficulty in predicting mandible bone strength especially for implant surgery, if no past experimental data is available. It is even worse if the inter-individual difference factor is taken into account. Hence, such a guideline or reference is necessary to help doctors. The present probabilistic method can be used to obtain β from the verified experimental data. Using the same β, variations in apparent mechanical properties where there are less experimental facts could be obtained by employing an extrapolation method. Therefore, in future, with the merit of the present method, we expect that the reliable apparent mechanical properties of a human mandible can also be predicted.

Furthermore, in the numerical design of a microstructure for the emergence of desired macroscopic properties, the use of stochastic simulation is expected to solve any mismatches between a numerically designed microstructure and a fabricated one. Figure 7.2 presents the hierarchical procedure for the proposed microstructure design. Suppose a manufacturer plans to fabricate a porous microstructure product with desired macroscopic properties $\boldsymbol{D^H}$. Considering variations in geometrical information $\hat{X}$, many possi-

ble microstructure models $\hat{Y}$ could be designed. A macroscopic property of the designed microstructure model is then calculated using the same approach as used in the present study. The process is repeated with variations in volume fraction V and morphology A until j microstructure models with the desired macroscopic properties are obtained. Taking the probability of each model, the effective properties can be computed. Next, some designed microstructure models j are fabricated and measured experimentally, to obtain the macroscopic properties. Based on the scattered experimental results, β is calibrated and characterizes any manufacturing variation. Macroscopic property variations are updated using the calibrated β, following which any variations in the effective value can be updated without solving a large linear algebraic equation. This new design procedure will show the right way to achieve the goal by repeating the improvement of either the microstructure model design or the fabrication process.

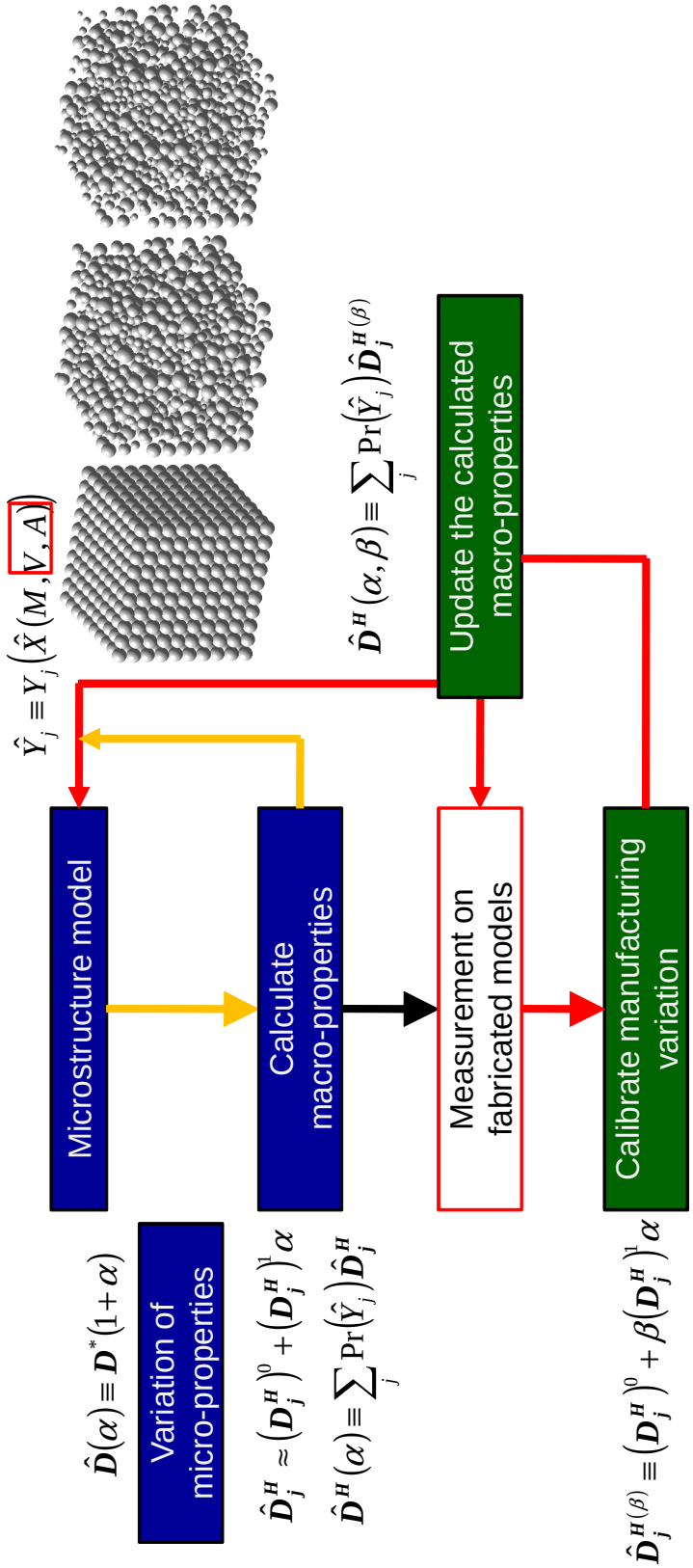

Figure 7.2: Hierarchical process for the proposed microstructure design.

Appendix A

Setup of anisotropy in trabecular bone tissue

A.1 Background and historical review

The mechanical properties in the trabecular bone region were modeled with a homogenized material model using apparent properties. Most researches use the experimentally obtained regression curve offered by Keyak *et al.* (1994). The anisotropy (or orthotropy) of macroscopic properties is not considered in Keyak et al.'s model, which is well-known, but it is still now most frequently used for simplicity. Another approach is to use the fabric tensor predicted through geometrical consideration.

In this thesis, a modeling methodology for considering the effect of biological apatite (BAp) crystallite orientation on microscopic properties is an experimental fact through X-ray diffraction measurement. It is well-known that cortical bone has orthotropic prop-

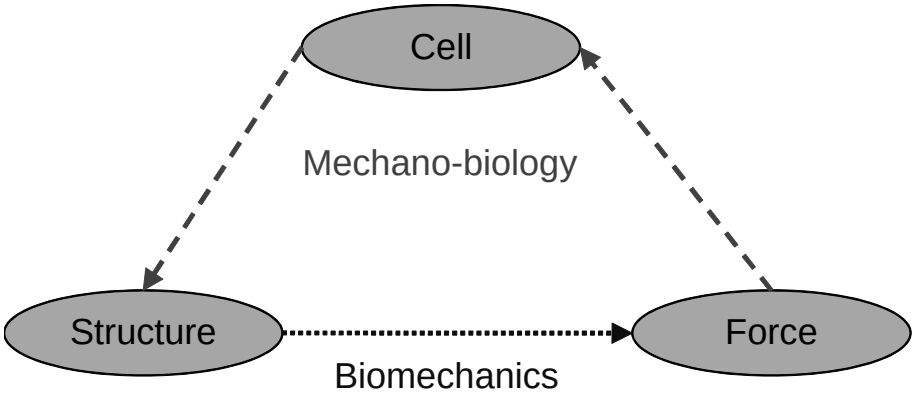

Figure A.1: Biomechanics and mechano-biology.

erties. For long bones, it was found through measurement that the Young's modulus in a longitudinal direction is twice as high as those in lateral directions. In the same way, it was clarified that the same is true for single trabeculae (Miyabe *et al.*, 2007).

Setup of the *c*-axis orientation of BAp for each voxel element was introduced by assuming that vertebral trabecular bone is remodeled to support main loading optimally, namely self-weight. It is believed that morphology changes optimally to produce load-bearing capability. The mechanism of remodeling has not been clarified, which is a matter of great interest within the field of mechano-biology, where it is important to know how cells behave under mechanical loading conditions, as shown in Fig. A.1. In the biomechanics field, mechanical responses are analyzed when morphology is established. In the above experiment on *c*-axis BAp crystallite orientation, the mechano-biological mechanism was unknown.

An unresolved problem is that the above modeling method of *c*-axis orientation is only true for vertebrae. In the mandible, for instance, the main loading mode is not clarified. Hence, the morphology of trabecular bone in mandibles is not clear. In

vertebral trabecular bone, it is well-known that rod-like and plate-like bones exist, and that primary and secondary bones exist, while the mandibular trabecular bone is much more complicated. In all recent research works on mandibles, isotropic properties are simply assumed. The above anisotropy setup is not applicable to the femur, and especially not to the femoral neck.

Hence, based on the results obtained by others' experimental works as mentioned above and in section 2.2, the following summarizes the findings which were used as assumptions for modeling and simulation in the present study:

1. In the vertebral trabecular bone, the c-axis is preferentially aligned in the vertical direction (axis-3), which is the direction of gravity in all ROIs.

2. The probability distribution of c-axis direction is in normal distribution by referring to the X-ray diffraction measurement.

3. The Young's modulus in axis-3 is assumed to be in normal distribution.

4. The bone is orthotropic at the micro-scale. The Young's modulus of trabecular bone in the lateral direction is half that of axis-3 in the same manner with cortical bone.

A.2 Deterministic homogenization

A.2.1 Setup of c-axis

In this thesis, section 4.4 uses modeling method outlined above to calculate apparent properties by employing the deterministic homogenization method, as shown in Fig. A.2.

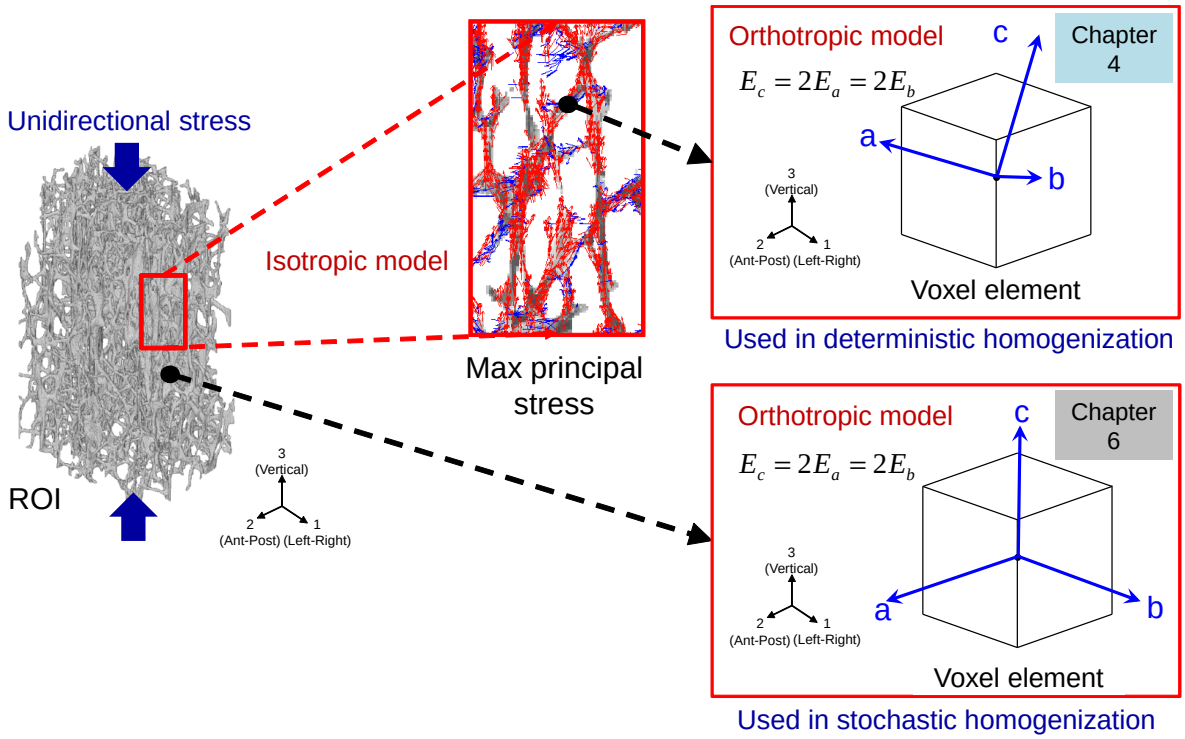

Figure A.2: Setup of a c-axis for each voxel element.

Including BAp crystallite orientation makes the simulation more reliable, because the effect of BAp on apparent properties is an experimental fact, and it confirmed that the Young's modulus in the c-axis was very influential regarding the final result. On the contrary, the a-axis and b-axis were not so important in the discussion on apparent vertical moduli.

To ensure the c-axis of BAp coincided with the gravity force axis, the micro-CT image was taken very carefully. A micro-CT image of trabecular bone was taken by ensuring the L4 bone specimen was in the vertical axis. The vertical axis of the CT scanner was adjusted properly, so that the bone-slicing axis of the captured CT image coincided with the gravity force direction. The vertical axis of L4 is parallel to the gravity force axis in general (as shown in Fig. A.3); however, the orientation of the L4

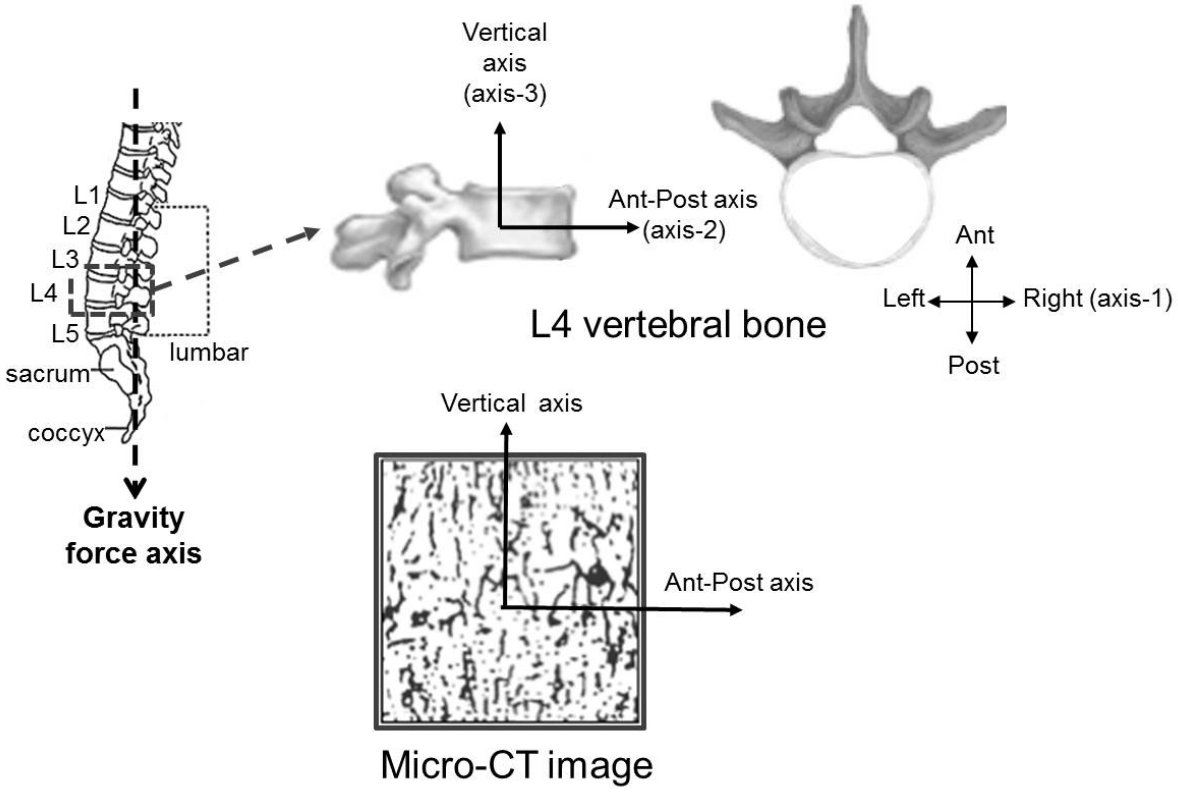

Figure A.3: Correlation between the gravity axis and vertical axis in L4.

body might be slightly different due to inter-individual differences. Hence, the vertical axis of the micro-CT image (axis-3) is assumed to be in the same direction as the gravity force axis, as shown in Figs. 3.1 and 3.2.

A.2.2 Setup of micro-macro scales

In the present study, micro-macro scale setting was defined in a hypothetical situation to hold the theory of homogenization. ROI size coincides with the representative dimension of the macro-scale. Note again, ROI is the term that often used in biomechanics field and is equivalent to RVE or unit cell in the computational mechanics field. Actually,

no macro problem was analyzed—only homogenization was carried out. Fig. A.4(a) illustrates mechanical response in a 1D manner. Here, the trabecular bone region is bounded by cortical bone. The average of an oscillating response, such as stress, can be defined as a constant value, as indicated by the red line. If this region is hypothetically repeated periodically, as shown in Fig. A.4(b), an average value remains. Therefore, the homogenization method is useful and is a scale-free problem, as illustrated in Fig. A.4(c). Hence, the ROI was selected very carefully, in order to hold periodicity with respect to bone density, as illustrated in Fig. 3.4.

Macroscopic properties (in section 4.4) were obtained using the periodic boundary condition. No actual macroscopic loads were applied in the calculation. The orthogonal macroscopic loads that were introduced in section 4.5 are just hypothetical unit loads for the classification method.

A.3 Stochastic homogenization

A.3.1 Setup of *c*-axis

In Chapter 6, a *c*-axis was set in the vertical direction (axis-3) for all voxel elements, as shown in Fig. A.2. It is possible to use the same *c*-axis setup in the future with the deterministic homogenization in section 4.4. In this thesis, however, a simple setup was adopted in order to reduce time and computational cost. Note that the expected values obtained through the stochastic homogenization method agree fairly well with the results in section 4.4. Therefore, the final conclusion does not change as a result of this simplification.

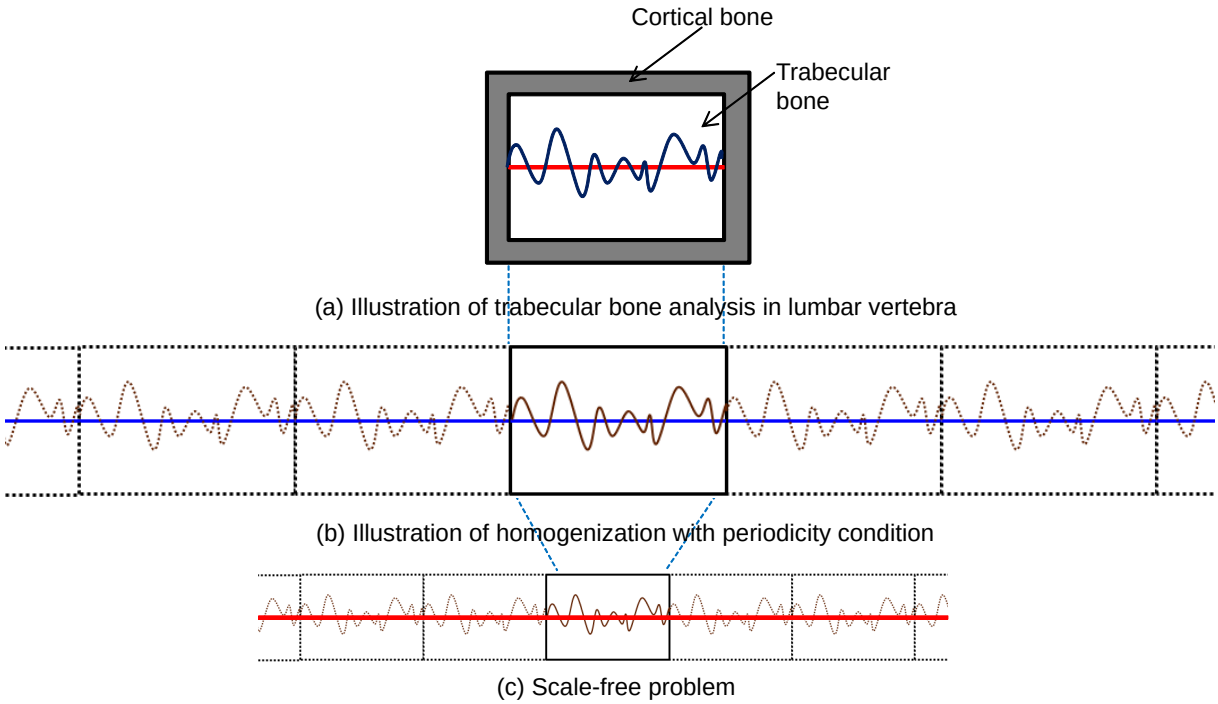

Figure A.4: Illustration of micro-macroscopic settings in a 1D problem.

A.3.2 Setup of random variable α

In the present study, the fluctuation of Young's moduli as a function of random variable α was set up in *Option 1*. The fluctuation of α was set at the same variation (standard deviation, $SD(\alpha)$) for both the vertical (axis-3) and lateral axes (axes-1 and 2), as shown in Fig. A.5(a). The orthotropic material setup in the calculation was assured by the elastic tensor matrix written in Eq. (6.36). Expression of the equation in *Option 1* is different from Fig. A.5(b), and Fig. A.5(a) is preferred in this study, not Fig. A.5(b).

Option 1 (present setting):

$$\begin{aligned} \hat{E}_3 &= E^0(1+\alpha) \\ \hat{E}_1 &= \hat{E}_2 = \frac{E^0}{2}(1+\alpha) \end{aligned} \tag{A.1}$$

The expression of Fig. A.5(b) can actually be written in *Option 2*, where two random variables are needed. For *Option 2*, the covariance between two random variables has to be defined in the covariance matrix. Two random parameters and the covariance (cov) are unknown parameters and are required to be assumed as input data:

Option 2:

$$\begin{aligned} \hat{E}_3 &= E^0(1+\alpha_1) \\ \hat{E}_1 &= \hat{E}_2 = \frac{E^0}{2}(1+\alpha_2) \end{aligned} \tag{A.2}$$

Due to the framework for the first-order perturbation method, the result is largely dependent on input parameters. Hence, the above setting results in an increase in varia-

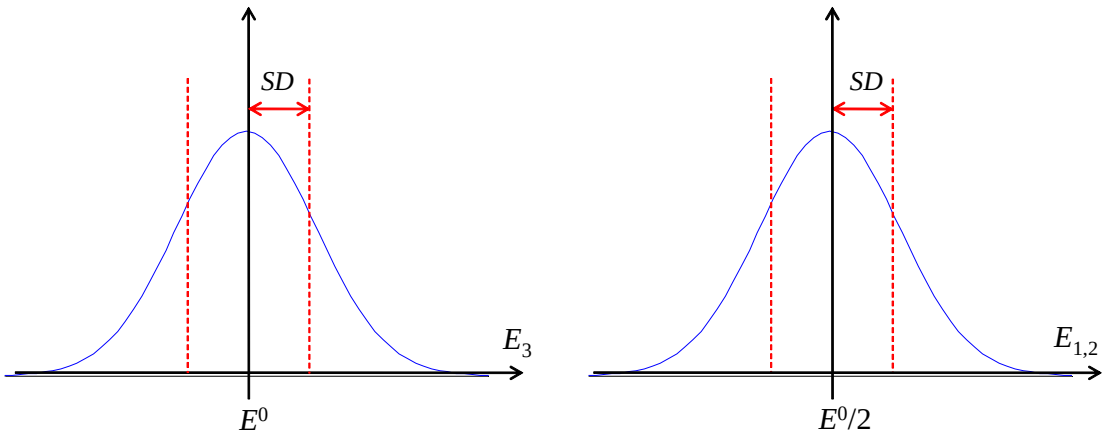

(a) Setup of fluctuation of α in the present study

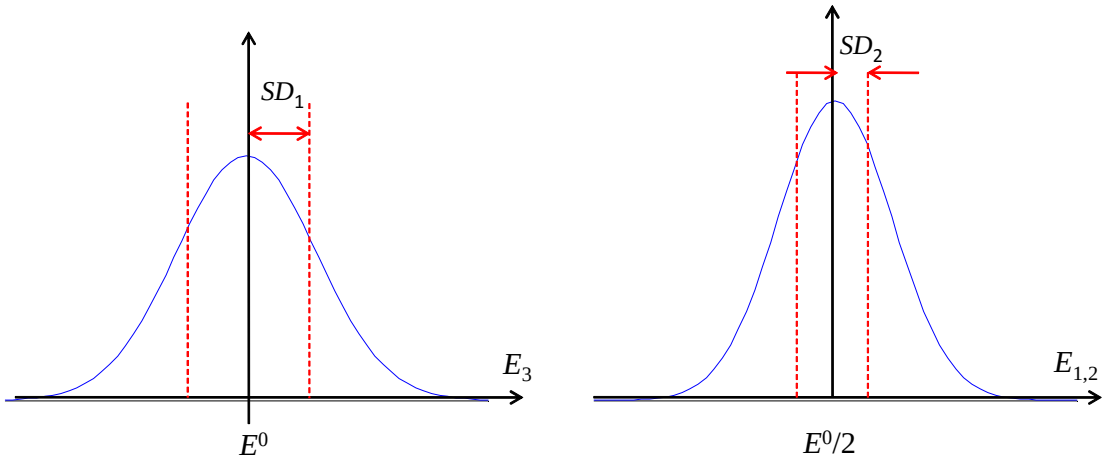

(b) Setup of fluctuation of α for option 2

Figure A.5: Options for setting up of random variable α.

tions in the apparent elastic moduli calculated by the following equations:

$$\mathrm{Var}(\hat{\boldsymbol{D}^{\boldsymbol{H}}}) = \sum_i \sum_j (\boldsymbol{D}^{\boldsymbol{H}})_i^1 (\boldsymbol{D}^{\boldsymbol{H}})_j^1 \,\mathrm{cov}(\alpha_i, \alpha_j) \tag{A.3}$$

and

$$\mathrm{cov}(\alpha_i, \alpha_j) = \begin{bmatrix} \{SD(\alpha_1)\}^2 & \mathrm{cov}(\alpha_1, \alpha_2) \\ \mathrm{cov}(\alpha_2, \alpha_1) & \{SD(\alpha_2)\}^2 \end{bmatrix} \tag{A.4}$$

where $SD(\alpha_1)$ and $SD(\alpha_2)$ are the standard deviation of α_1 and α_2. Since more emphasis is put on the morphology effect, the influence of microscopic bone property was set at the minimum level.

In a general way, random variable α should be in the form of a tensor. However, in this case too many parameters need to be defined and assumed. The probability density of two independent random variables with different variations can be visualized in Fig. A.6(a); nonetheless, let two independent variables be the same value as illustrated in Fig. A.6(b). Here, it is equivalent to the setup with only one random variable if the fluctuation is assumed to be very small. Hence, in this study only one random variable, as written in *Option 1*, was used.

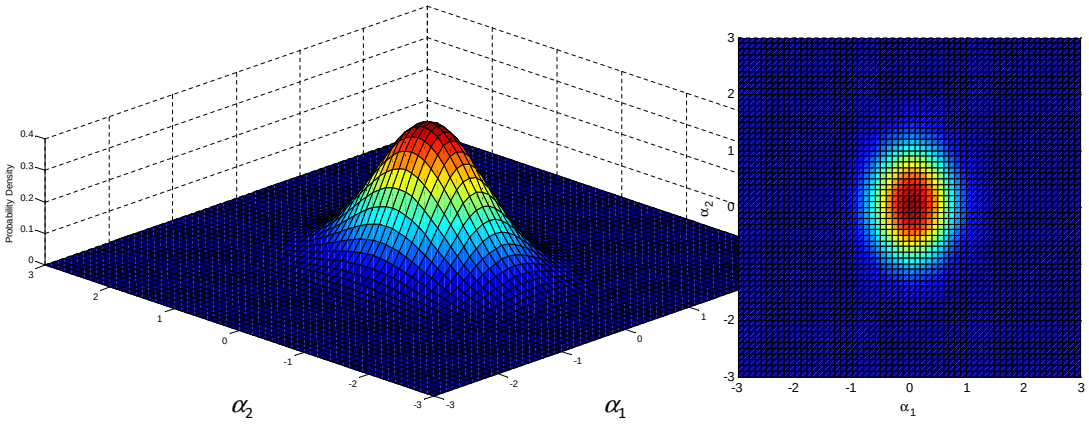

(a) Probability density for two independent random variables with different values

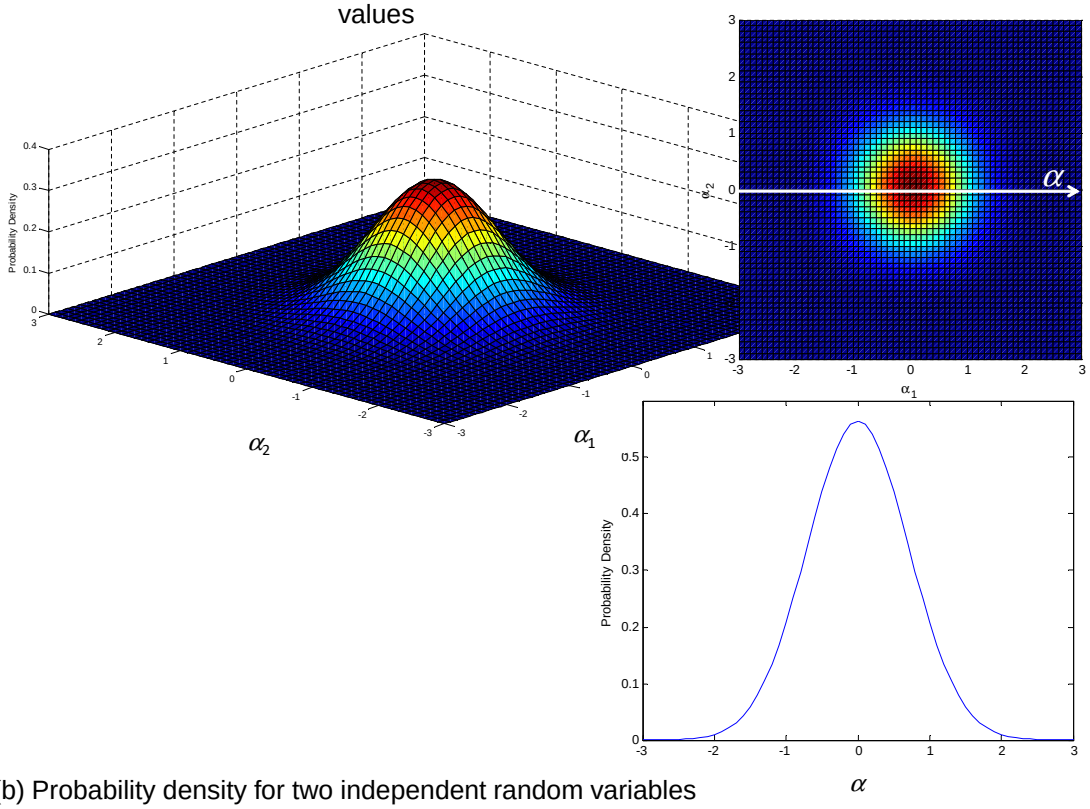

(b) Probability density for two independent random variables with same values

Figure A.6: Illustration of the normal distribution of random variables.

Appendix B

Setup of the probability of image-based modeling (PrI)

B.1 Motivation

One of the goals of this study was to develop a methodology to predict widespread scattering in experimental results provided by, for instance, Keyak *et al.* (1994). Through the analyses shown in Fig. 6.5, the effect of mechanical properties is not so great in the first-order perturbation method framework. It was possible to employ greater variation to Young's microstructure modulus, for instance by providing the two random parameters described in Appendix A, to express the widespread scattering of homogenized properties. Since morphology is considered a main topic in this study, however, network architecture cannot be neglected.

To predict the probability density of the Young's modulus for a certain bone den-

sity when considering inter-individual differences in morphology, the right amount of specimens is usually necessary. This is of course unrealistic, so stochastic image-based modeling was proposed in this thesis whereby eight models were generated through eight image-based modeling procedures. Three popular image processing techniques—labeling, dilation, and erosion—were adopted in this study. The voxel edge was introduced to avoid the rotation of trabecular struts at a certain connected edge. The eight image-based modeling procedures were introduced to create variations in morphology that could possibly be generated from one original specimen or one set of images due to uncertainty regarding image-processing. The motivation of this study lies in the compensation of analyzing many individuals—by the eight types of morphology generated from one specimen—to predict easily the scattering mainly due to inter-individual differences.

B.2 Assumption of PrI

One possible probability was so-called 'flat probability', which is also used in Bayesian statistics for any unknown probabilities. Fig. B.1 shows the result when flat probability is adopted. The result suggests that it can express widespread scattering among seven references very well. However, the normal distribution type was proposed in this thesis, because two image-processing procedures were believed to be more reliable than the other six procedures, as listed in Table 6.2. The assumption shown in Fig. 6.9 is the simplest, which is the reason why it was proposed. In the calibration of β, not much attention was given to the probability around the mean value quantitatively, but to the tail probability. In that sense also, the assumption of Fig. 6.9 was not so significant.

The result in Fig. 6.5 suggests that the influence of voxel edge enrichment was min-

imal, but this depends on the solver. The present computational code used an element-by-element scaled conjugate gradient (EBE-SCG) and was verified by commercial VOXELCON software (Quint Corp.). It was believed to be reasonable that the probability of I_j=3 and I_j=6 was around one-third of that for I_j=4 and I_j=5. Note here that voxel edge treatment was implemented in DoctorBQ software (Cybernet Corp.) and it is a unique procedure specific to voxel meshing. Note also that the set of dilation and erosion times four was not used because it obviously generates an unreasonable model with very high bone density. Introducing the erosion process earlier than the dilation process could not change the morphology of trabecular bone model. Also, it was considered to be unreasonable to use a set of dilation and erosion with different number of times.

The proposed methodology can also help software users to generate different models from one set of images. The results in Fig. 6.5 provide useful information on this subject, although it was not the purpose of this study and the goal lies in the discussion in Fig. 6.14. Note that flexible comprehension of the stochastic image-based modeling methodology led to an idea of microstructure design for engineering materials as shown in Fig. 7.1.

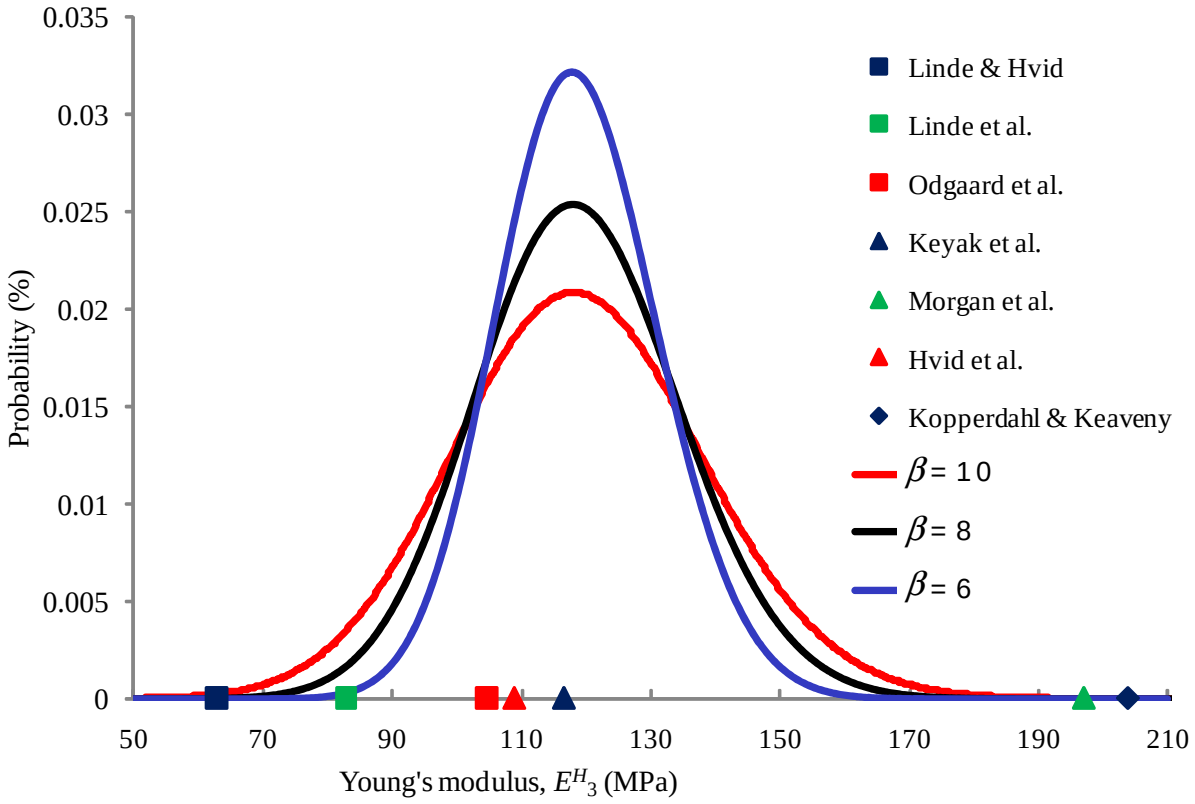

Figure B.1: PDF for O1 if the same PrI is assigned for each **I** model.

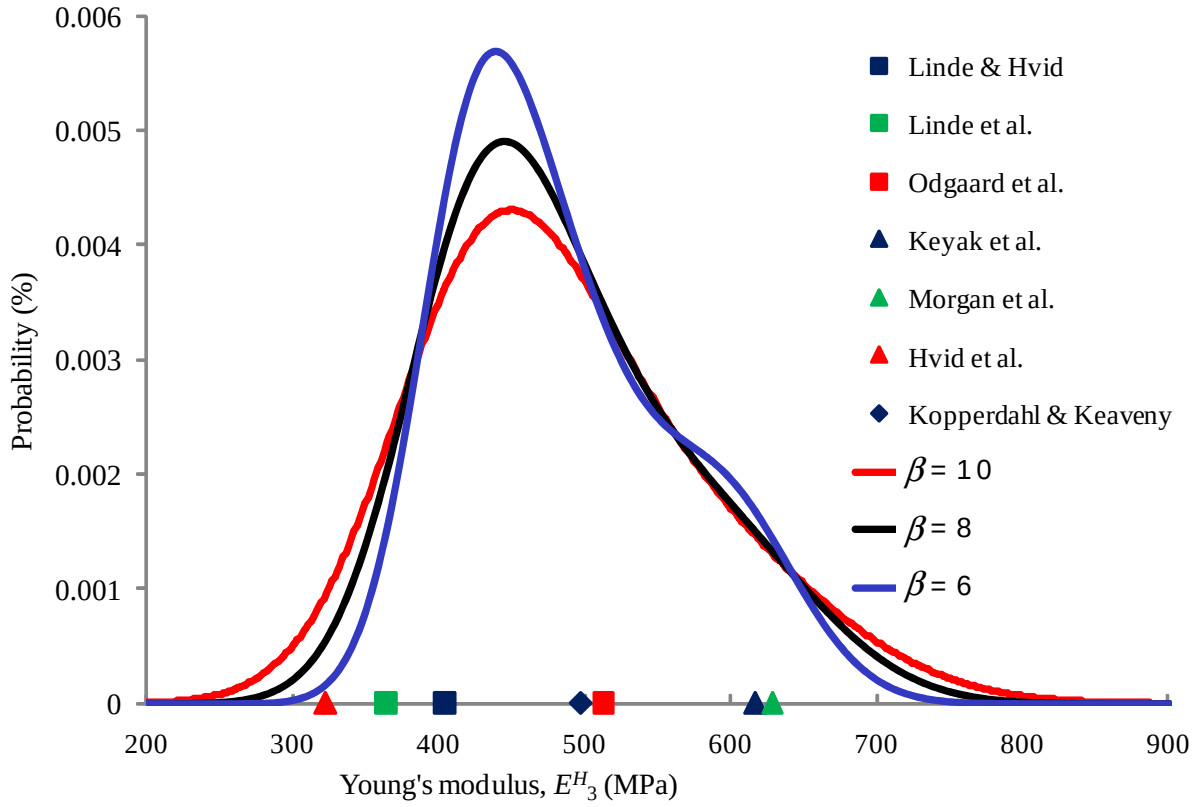

Figure B.2: PDF for H1 if the same PrI is assigned for each **I** model.

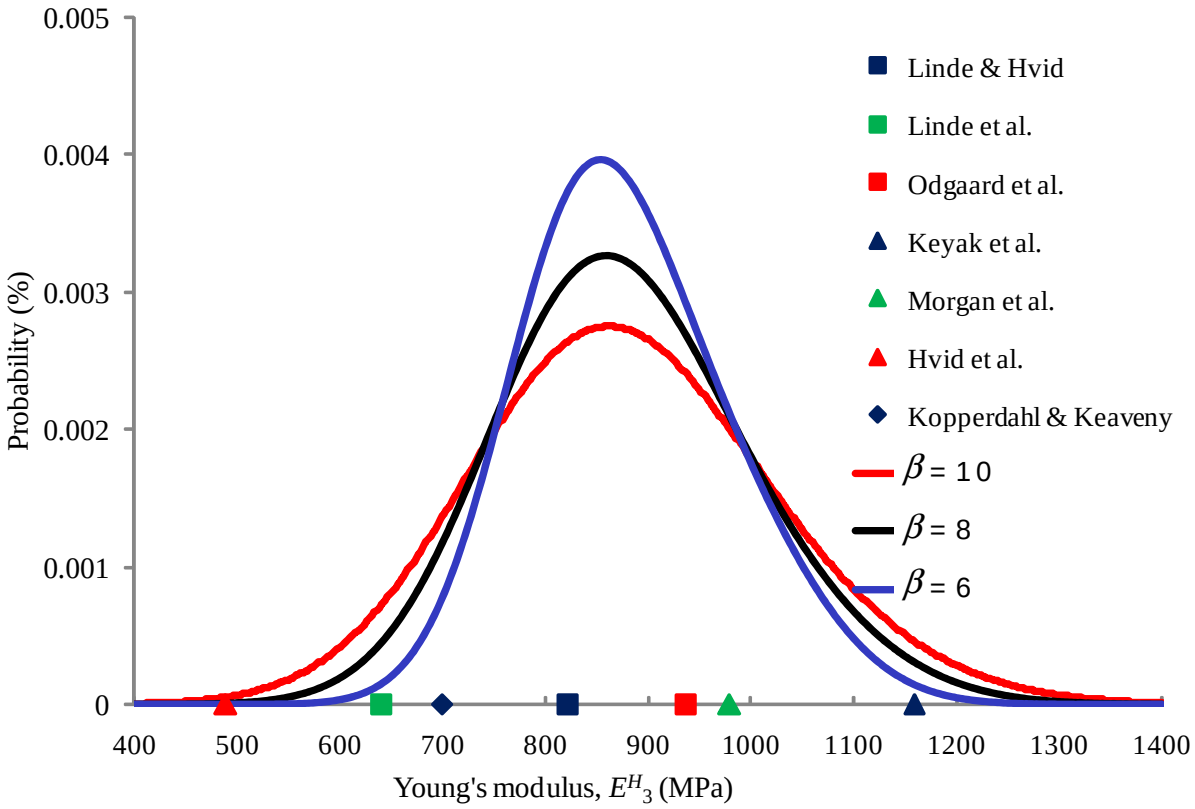

Figure B.3: PDF for H2 if the same PrI is assigned for each **I** model.

Appendix C

List of publications

C.1 Journal articles

1. **K.S. Basaruddin**, N. Takano, T. Nakano, Stochastic multi-scale prediction on the apparent elastic moduli of trabecular bone considering uncertainties of biological apatite (BAp) crystallite orientation and image-based modelling, *Computer Methods in Biomechanics and Biomedical Engineering*, (2013).
   DOI:10.1080/10255842.2013.785537. (in press)

2. **K.S. Basaruddin**, N. Takano, H. Akiyama, T. Nakano, Uncertainty modeling in the prediction of effective mechanical properties using stochastic homogenization method with application to porous trabecular bone, *Materials Transactions*, 54 (2013) pp. 1250-1256.

3. **K.S. Basaruddin**, N. Takano, Y. Yoshiwara, T. Nakano, Morphology analysis of vertebral trabecular bone under dynamic loading based on multi-scale theory,

Medical and Biological Engineering and Computing, 50 (2012) pp. 1091-1103.

C.2 International conferences

1. N. Takano, **K. S. Basaruddin**, Stochastic image-based homogenization analysis of osteoporotic trabecular bone, *CD-ROM Proceedings of the International Computational Mechanics Symposium (ICMS2012)*, October 9-11, 2012, Kobe, Japan.

2. **K. S. Basaruddin**, N. Takano, Stochastic modelling and analysis of porous media using first-order perturbation-based homogenization method, *CD-ROM Proceedings of the 6th European Congress on Computational Methods in Applied Sciences and Engineering (ECCOMAS 2012)*, September 10-14, 2012, Vienna, Austria.

3. N. Takano, **K. S. Basaruddin**, T. Ishimoto, T. Nakano, Morphology analysis of vertebral trabecular bone under dynamic loading by multiscale theory, *CD-ROM Proceedings of the 18th Congress of the European Society of Biomechanics (ESB2012)*, July 1-4, 2012, Lisbon, Portugal.

4. **K.S. Basaruddin**, Y. Yoshiwara, N. Takano, Analysis on the morphology and mechanical role of vertebral trabecular bone, *CD-ROM Proceedings of the 2011 World Congress on Advances in Structural Engineering and Mechanics (ASEM11+)*, September 18-22, 2011, Seoul, South Korea.

C.3 Domestic conferences

1. **K. S. Basaruddin**, N. Takano, Evaluation of bone quality for human vertebral tra-

becular bone by stochastic image-based multi-scale method, *Proceedings of the 18th Computational Engineering Conference (JSCES2013)*, June 19-21, 2013, Tokyo, Japan.

2. **K. S. Basaruddin**, N. Takano, Y. Yoshiwara, T. Nakano, Morphology analysis of vertebral trabecular bone under dynamic loading by multiscale method, *CD-ROM Proceedings of the 17th Computational Engineering Conference (JSCES 2012)*, May 29-31, 2012, Kyoto, Japan.

3. **K. S. Basaruddin**, N. Takano, Y. Yoshiwara, T. Nakano, Stochastic homogenization analysis based on first-order perturbation method applied to porous microstructure, *CD-ROM Proceedings of the 17th Computational Engineering Conference (JSCES 2012)*, May 29-31, 2012, Kyoto, Japan.

4. **K.S. Basaruddin**, Y. Yoshiwara, N. Takano, Prediction of macroscopic properties of vertebral trabecular bone and comparison with Keyak's model, *CD-ROM Proceedings of the 24th Annual Conference on Computational Mechanics JSME (CMD2011)*, October 8-10, 2011, Okayama, Japan.

5. **K.S. Basaruddin**, Y. Yoshiwara, N. Takano, T. Nakano, Numerical study on the morphology and mechanical role of healthy and osteoporotic vertebral trabecular bone, *Proceedings of the 17th Conference of Japan Society of Mechanical Engineering Kanto Branch*, March 18-19, 2011, Yokohama, Japan.

Bibliography

Adachi, T., Tsubota, K., Tomita, Y., and Hollister, S.J., 2001. Trabecular surface remodeling simulation for cancellous bone using microstructural voxel finite element models, *Journal of Biomechanical Engineering*, 123 (5), 403–409.

Anderson, M.J., Keyak, J.H., and Skinner, H.B., 1992. Compressive mechanical properties of human cancellous bone after gamma irradiation, *The Journal of Bone and Joint Surgery*, 74 (5), 747–752.

Ashman, R.B., Rho, J.Y., and Turner, C.H., 1989. Anatomical variation of orthotropic elastic moduli of the proximal human tibia, *Journal of Biomechanics*, 22 (8/9), 895–900.

Beck, J.D., Canfield, B.L., Haddock, S.M., Chen, T.J.H., Kothari, M., and Keaveny, T.M., 1997. Three-dimensional imaging of trabecular bone using the computer numerically controlled milling technique, *Bone*, 21 (3), 281–287.

Bevill, G. and Keaveny, T.M., 2009. Trabecular bone strength predictions using finite element analysis of micro-scale images at limited spatial resolution, *Bone*, 44 (4), 579–584.

Birkenhäger-Frenkel, D.H., Nigg, A.L., Hens, C.J., and Birkenhäger, J.C., 1993. Changes of interstitial bone thickness with age in men and women, *Bone*, 14 (3), 211–216.

Blain, H., Chavassieux, P., Portero-Muzy, N., Bonnel, F., Canovas, F., Chammas, M., Maury, P., and Delmas, P.D., 2008. Cortical and trabecular bone distribution in the femoral neck in osteoporosis and osteoarthritis, *Bone*, 43 (5), 862–868.

Carter, D.R. and Hayes, W.C., 1977. The compressive behavior of bone as a two-phase porous structure, *Journal of Bone and Joint Surgery*, 59 (7), 954–962.

Chen, H.L. and Gundjian, A.A., 1974. Determination of the bone-crystallites distribution function by X ray diffraction, *Medical and Biological Engineering*, 12 (4), 531–536.

Chesnut, C.H. and Rosen, C.J., 2001. Reconsidering the effects of antiresorptive therapies in reducing osteoporotic fracture, *Journal of Bone and Mineral Research*, 16 (12), 2163–2172.

Chevalier, Y., Pahr, D., Allmer, H., Charlebois, M., and Zysset, P., 2007. Validation of a voxel-based FE method for prediction of the uniaxial apparent modulus of human trabecular bone using macroscopic mechanical tests and nanoindentation, *Journal of Biomechanics*, 40 (15), 3333–3340.

Choi, K. and Goldstein, S.A., 1992. A comparison of the fatigue behavior of human trabecular and cortical bone tissue, *Journal of Biomechanics*, 25 (12).

Choi, K., Kuhn, J.L., Ciarelli, M.J., and Goldstein, S.A., 1990. The elastic moduli of human subchondral, trabecular, and cortical bone tissue and the size-dependency of cortical bone modulus, *Journal of Biomechanics*, 23, 1103–1113.

Currey, J.D., 1986. Power law models for the mechanical properties of cancellous bone, *Engineering in Medicine*, 15 (3), 153–154.

Dalle Carbonare, L., Valenti, M.T., Bertoldo, F., Zanatta, M., Zenari, S., Realdi, G., Lo Cascio, V., and Giannini, S., 2005. Bone microarchitecture evaluated by histomorphometry, *Micron*, 36 (7), 609–616.

Dempster, D.W., 2000. The contribution of trabecular architecture to cancellous bone quality, *Journal of Bone and Mineral Research*, 15 (1), 20–23.

Feldkamp, L.A., Goldstein, S.A., Parfitt, A.M., Jesion, G., and Kleerekoper, M., 1989. The direct examination of three-dimensional bone architecture in vitro by computed tomography, *Journal of Bone and Mineral Research*, 4 (1), 3–11.

Fratzl, P. and Weinkamer, R., 2007. Natures hierarchical materials, *Progress in Materials Science*, 52 (8), 1263–1334.

Frost, H.M., 1989. Transient-steady state phenomena in microdamage physiology: a proposed algorithm for lamellar bone, *Calcified Tissue International*, 44 (6), 367–381.

Gefen, A., 2009. Finite element modeling of the microarchitecture of cancellous bone: techniques and applications, *in:* C.T. Leondes, ed., *Biomechanical Systems Technology: Muscular Skeletal Systems*, World Scientific Pub Co Inc, 73–112.

Gibson, L.J., 1985. The mechanical behaviour of cancellous bone, *Journal of Biomechanics*, 18 (5), 317–328.

Gibson, L.J. and Ashby, M.F., 1997. *Cellular Solids: Structure and Properties*, Cambridge Solid State Science Series, Cambridge University Press.

Goldstein, S.A., Goulet, R., and McCubbrey, D., 1993. Measurement and significance of three-dimensional architecture to the mechanical integrity of trabecular bone, *Calcified Tissue International*, 53 (Suppl 1), S127–S133.

Goulet, R.W., Goldstein, S.A., Ciarelli, M.J., Kuhn, J.L., Brown, M.B., and Feldkamp, L.A., 1994. The relationship between the structural and orthogonal compressive properties of trabecular bone, *Journal of Biomechanics*, 27 (4), 375–389.

Gross, T., Pahr, D.H., Peyrin, F., and Zysset, P.K., 2012. Mineral heterogeneity has a minor influence on the apparent elastic properties of human cancellous bone: a SRμCT-based finite element study, *Computer Methods in Biomechanics and Biomedical Engineering*, 15 (11), 1137–1144.

Guedes, J. and Kikuchi, N., 1990. Preprocessing and postprocessing for materials based on the homogenization method with adaptive finite element methods, *Computer Methods in Applied Mechanics and Engineering*, 83 (2), 143–198.

Guldberg, R.E., Hollister, S.J., and Charras, G.T., 1998. The accuracy of digital image-based finite element models, *Journal of Biomechanical Engineering*, 120 (2), 289–295.

Guo, X.E., 2001. Mechanical properties of cortical bone and cancellous bone tissue, *in:* S.C. Cowin, ed., *Bone Mechanics Handbook*, CRC Press, vol. 56, chap. 10.

Haïat, G., Padilla, F., Peyrin, F., and Laugier, P., 2007. Variation of ultrasonic parameters with microstructure and material properties of trabecular bone: a 3D model simulation, *Journal of Bone and Mineral Research*, 22 (5), 665–674.

Hara, T., Tanck, E., Homminga, J., and Huiskes, R., 2002. The influence of microcom-

puted tomography threshold variations on the assessment of structural and mechanical trabecular bone properties, *Bone*, 31 (1), 107–109.

Harrigan, T.P., Jasty, M., Mann, R.W., and Harris, W.H., 1987. Limitation of the continuum assumption in cancellous bone, *Journal of Biomechanics*, 21 (4), 269–275.

Harrison, N.M., McDonnell, P.F., O'Mahoney, D.C., Kennedy, O.D., O'Brien, F.J., and McHugh, P.E., 2008. Heterogeneous linear elastic trabecular bone modelling using micro-CT attenuation data and experimentally measured heterogeneous tissue properties, *Journal of Biomechanics*, 41 (11), 2589–2596.

Helgason, B., Perilli, E., Schileo, E., Taddei, F., Brynjólfsson, S., and Viceconti, M., 2008. Mathematical relationships between bone density and mechanical properties: a literature review, *Clinical Biomechanics*, 23 (2), 135–146.

Hernandez, C.J. and Keaveny, T.M., 2006. A biomechanical perspective on bone quality, *Bone*, 39 (6), 1173–1181.

Hildebrand, T. and Ruegsegger, P., 1997. A new method for the model-independent assessment of thickness in three-dimensional images, *Journal of Microscopy*, 185 (1), 67–75.

Hollister, S.J., Brennan, J.M., and Kikuchi, N., 1994. A homogenization sampling procedure for calculating trabecular bone effective stiffness and tissue level stress, *Journal of Biomechanics*, 27 (4), 433–444.

Hollister, S.J., Fyhrie, D.P., Jepsen, K.J., and Goldstein, S.A., 1991. Application of homogenization theory to the study of trabecular bone mechanics, *Journal of Biomechanics*, 24 (9), 825–839.

Hollister, S.J. and Kikuchi, N., 1994. Homogenization theory and digital imaging: a basis for studying the mechanics and design principles of bone tissue, *Biotechnology and Bioengineering*, 43 (7), 586–596.

Hollister, S.J. and Riemer, B.A., 1993. Digital-image-based finite element analysis for bone microstructure using conjugate gradient and Gaussian filter techniques, *in: SPIE Proceedings: Mathematical Methods in Medical Imaging*, 95–106.

Homminga, J., Van-Rietbergen, B., Lochmüller, E.M., Weinans, H., Eckstein, F., and Huiskes, R., 2004. The osteoporotic vertebral structure is well adapted to the loads of daily life, but not to infrequent "error" loads, *Bone*, 34 (3), 510–516.

Homminga, J., Weinans, H., Gowin, W., Felsenberg, D., and Huiskes, R., 2001. Osteoporosis changes the amount of vertebral trabecular bone at risk of fracture but not the vertebral load distribution, *Spine*, 26 (14), 1555–1561.

Hosokawa, A., 2008. Development of a numerical cancellous bone model for finite-difference time-domain simulations of ultrasound propagation, *IEEE Transactions on Ultrasonics, Ferroelectrics and Frequency Control*, 55 (6), 1219–1233.

Hosokawa, A., 2011. Numerical investigation of ultrasound refraction caused by oblique orientation of trabecular network in cancellous bone, *IEEE Transactions on Ultrasonics, Ferroelectrics and Frequency Control*, 58 (7), 1389–1396.

Hou, F.J., Lang, S.M., Hoshaw, S.J., Reimann, D.a., and Fyhrie, D.P., 1998. Human vertebral body apparent and hard tissue stiffness, *Journal of Biomechanics*, 31 (11), 1009–1015.

Hvid, I., Bentzen, S.M., Linde, F., Mosekilde, L., and Pongsoipetch, B., 1989. X-ray

quantitative computed tomography: the relations to physical properties of proximal tibial trabecular bone specimens, *Journal of Biomechanics*, 22 (8/9), 837–844.

Jaasma, M.J., Bayraktar, H.H., Niebur, G.L., and Keaveny, T.M., 2002. Biomechanical effects of intraspecimen variations in tissue modulus for trabecular bone, *Journal of Biomechanics*, 35 (2), 237–246.

Judex, S., Boyd, S., Qin, Y.X., Miller, L., Müller, R., and Rubin, C., 2003. Combining high-resolution micro-computed tomography with material composition to define the quality of bone tissue, *Current Osteoporosis Reports*, 1 (1), 11–19.

Kabel, J., Odgaard, A., van Rietbergen, B., and Huiskes, R., 1999. Connectivity and the elastic properties of cancellous bone, *Bone*, 24 (2), 115–120.

Kameo, Y., Adachi, T., and Hojo, M., 2011. Effects of loading frequency on the functional adaptation of trabeculae predicted by bone remodeling simulation, *Journal of the Mechanical Behavior of Biomedical Materials*, 4 (6), 900–908.

Kaminski, M., 2009. Sensitivity and randomness in homogenization of periodic fiber-reinforced composites via the response function method, *International Journal of Solids and Structures*, 46 (3), 923–937.

Kaminski, M. and Kleiber, M., 2000. Perturbation based stochastic finite element method for homogenization of two-phase elastic composites, *Computers and Structures*, 78 (6), 811–826.

Karim, L. and Vashishth, D., 2011. Role of trabecular microarchitecture in the formation, accumulation, and morphology of microdamage in human cancellous bone, *Journal of Orthopaedic Research*, 29, 1739–1744.

Keaveny, T.M., Pinilla, S.I., Crawford, P., Kopperdahl, D.L., and Lou, A., 1997. Systematic and random errors in compression testing of trabecular bone, *Journal of Orthopaedic Research*, 15, 101–110.

Keller, T.S., 1994. Predicting the compressive mechanical behavior of bone, *Journal of Biomechanics*, 27 (9), 1159–1168.

Keyak, J.H., Lee, I.Y., and Skinner, H.B., 1994. Correlations between orthogonal mechanical properties and density of trabecular bone: use of different densitometric measures, *Journal of Biomedical Material Research*, 28 (11), 1329–1336.

Kinney, J.H. and Ladd, A.J.C., 1998. The relationship between three-dimensional connectivity and the elastic properties of trabecular bone, *Journal of Bone and Mineral Research*, 13 (5), 839–845.

Koishi, M., Shiratori, M., Miyoshi, T., and Miyano, A., 1996. Stochastic homogenization method for composite materials with uncertain microstructures, *Transactions of Japan Society of Mechanical Engineer Series A*, 62, 2264–2269.

Kopperdahl, D.L. and Keaveny, T.M., 1998. Yield strain behavior of trabecular bone, *Journal of Biomechanics*, 31 (7), 601–608.

Kopperdahl, D.L., Morgan, E.F., and Keaveny, T.M., 2002. Quantitative computed tomography estimates of the mechanical properties of human vertebral trabecular bone, *Journal of Orthopaedic Research*, 20 (4), 801–805.

Kosturski, N. and Margenov, S., 2010. Numerical homogenization of bone microstructure, *in:* I. Lirkov, S. Margenov, and J. Wasniewski, eds., *Large-Scale Scientific Computing*, Springer Berlin / Heidelberg, vol. 5910, 140–147.

Kuhlemeyer, R. and Lysmer, J., 1973. Finite element method accuracy for wave propagation problems, *Journal of the Soil Mechanics and Foundations Division, Proceedings of the American Society of Civil Engineers*, 99 (5), 421–427.

Ladd, A.J. and Kinney, J.H., 1998. Numerical errors and uncertainties in finite-element modeling of trabecular bone, *Journal of Biomechanics*, 31 (10), 941–945.

Landis, W.J., Hodgens, K.J., Arena, J., Song, M.J., and McEwen, B.F., 1996. Structural relations between collagen and mineral in bone as determined by high voltage electron microscopic tomography, *Microscopy Research and Technique*, 33 (2), 192–202.

Lewy, H., Friedrichs, K., and Courant, R., 1967. On the partial difference equations of mathematical physics, *IBM Journal of Research and Development*, 11 (2), 215–234.

Linde, F., Christian, H., and Sorensen, F., 1993. The effect of different storage methods on the mechanical properties of trabecular bone, *Journal of Biomechanics*, 26, 1249–1252.

Linde, F. and Hvid, I., 1989. The effect of constraint on the mechanical behaviour of trabecular bone specimen, *Journal of Biomechanics*, 22 (5), 485–490.

Linde, F., Hvid, I., and Madsen, F., 1992. The effect of specimen geometry on the mechanical behaviour of trabecular bone specimens, *Journal of Biomechanics*, 25 (4), 359–368.

Linde, F., Norgaard, P., Hvid, I., Odgaard, A., and Soballe, K., 1991. Mechanical properties of trabecular bone. Dependency on strain rate, *Journal of Biomechanics*, 24 (9), 803–809.

Liu, X.S., Huang, A.H., Zhang, X.H., Sajda, P., Ji, B., and Guo, X.E., 2008a. Dynamic simulation of three dimensional architectural and mechanical alterations in human trabecular bone during menopause, *Bone*, 43 (2), 292–301.

Liu, X.S., Sajda, P., Saha, P.K., Wehrli, F.W., Bevill, G., Keaveny, T.M., and Guo, X.E., 2008b. Complete volumetric decomposition of individual trabecular plates and rods and its morphological correlations with anisotropic elastic moduli in human trabecular bone, *Journal of Bone and Mineral Research*, 23 (2), 223–235.

Liu, X.S., Sajda, P., Saha, P.K., Wehrli, F.W., and Guo, X.E., 2006. Quantification of the roles of trabecular microarchitecture and trabecular type in determining the elastic modulus of human trabecular bone, *Journal of Bone and Mineral Research*, 21 (10), 1608–1617.

Lysmer, J. and Kuhlemeyer, R.L., 1969. Finite dynamic model for infinite media, *Journal of the Engineering Mechanics Division, Proceedings of the American Society of Civil Engineers*, 95 (4), 859–877.

Majumdar, S., Kothari, M., Augat, P., Newitt, D.C., Link, T.M., Lin, J.C., Lang, T., Lu, Y., and Genant, H.K., 1998. High-resolution magnetic resonance imaging: three-dimensional trabecular bone architecture and biomechanical properties, *Bone*, 22 (5), 445–454.

Martin, R.B. and Burr, D.B., 1989. *Structure, Function, and Adaptation of Compact Bone*, Raven Press.

Mc Donnell, P., Harrison, N., Liebschner, M.A.K., and Mc Hugh, P.E., 2009. Simulation of vertebral trabecular bone loss using voxel finite element analysis, *Journal of Biomechanics*, 42 (16), 2789–2796.

Miyabe, S., Nakano, T., Ishimoto, T., Takano, N., Adachi, T., Iwaki, H., Kobayashi, A., Takaoka, K., and Umakoshi, Y., 2007. Two-dimensional quantitative analysis of preferential alignment of bap c-axis for isolated human trabecular bone using microbeam x-ray diffractometer with a transmission optical system, *Materials Transactions*, 48 (3), 343–347.

Morgan, E.F., Bayraktar, H.H., and Keaveny, T.M., 2003. Trabecular bone modulus-density relationships depend on anatomic site, *Journal of Biomechanics*, 36 (7), 897–904.

Mosekilde, L., 1988. Age-related changes in vertebral trabecular bone architecture-assessed by a new method, *Bone*, 9 (4), 247–250.

Mosekilde, L., 1993. Vertebral structure and strength in vivo and in vitro, *Calcified Tissue International*, 53 (Suppl 1), S121–S126.

Müller, R., Hildebrand, T., and Rüegsegger, P., 1994. Non-invasive bone biopsy: a new method to analyse and display the three-dimensional structure of trabecular bone, *Physics in Medicine and Biology*, 39 (1), 145–164.

Nakano, T., Ishimoto, T., Umakoshi, Y., and Tabata, Y., 2005. Texture of biological apatite crystallites and the related mechanical function in regenerated and pathological hard tissues, *Journal of Hard Tissue Biology*, 14 (4), 363–364.

Nakano, T., Kaibara, K., Tabata, Y., Nagata, N., Enomoto, S., Marukawa, E., and Umakoshi, Y., 2002. Unique alignment and texture of biological apatite crystallites in typical calcified tissues analyzed by microbeam x-ray diffractometer system, *Bone*, 31 (4), 479–487.

Nicholson, P.H., Cheng, X.G., Lowet, G., Boonen, S., Davie, M.W., Dequeker, J., and Van der Perre, G., 1997. Structural and material mechanical properties of human vertebral cancellous bone, *Medical Engineering & Physics*, 19 (8), 729–737.

Niebur, G.L., Yuen, J.C., Hsia, A.C., and Keaveny, T.M., 1999. Convergence behavior of high-resolution finite element models of trabecular bone, *Journal of Biomechanical Engineering*, 121 (6), 629–635.

Odgaard, A., Andersen, K., Melsen, F., and Gundersen, H.J., 1990. A direct method for fast three-dimensional serial reconstruction, *Journal of Microscopy*, 159, 335–342.

Odgaard, A. and Linde, F., 1991. The underestimation of Young's modulus in compressive testing of cancellous bone specimens, *Journal of Biomechanics*, 24 (8), 691–698.

Padilla, F., Bossy, E., Haiat, G., Jenson, F., and Laugier, P., 2006. Numerical simulation of wave propagation in cancellous bone, *Ultrasonics*, 44, e239–e243.

Parnell, W.J., Grimal, Q., Abrahams, I.D., and Laugier, P., 2006. Modelling cortical bone using the method of asymptotic homogenization, *Journal of Biomechanics*, 39 (Suppl 1), S20.

Pothuaud, L., Laib, A., Levitz, P., Benhamou, C.L., and Majumdar, S., 2002. Three-dimensional-line skeleton graph analysis of high-resolution magnetic resonance images: a validation study from 34-microm-resolution microcomputed tomography, *Journal of Bone and Mineral Research*, 17 (10), 1883–1895.

Pothuaud, L., Porion, P., Lespessailles, E., Benhamou, C.L., and Levitz, P., 2000. A new method for three-dimensional skeleton graph analysis of porous media: application to trabecular bone microarchitecture, *Journal of Microscopy*, 199 (Pt 2), 149–161.

Rajapakse, C.S., Magland, J., Zhang, X.H., Liu, X.S., Wehrli, S.L., Guo, X.E., and Wehrli, F.W., 2009a. Implications of noise and resolution on mechanical properties of trabecular bone estimated by image-based finite-element analysis, *Journal Orthopaedic Research*, 27 (10), 1263–1271.

Rajapakse, C.S., Magland, J., Zhang, X.H., Liu, X.S., Wehrli, S.L., Guo, X.E., and Wehrli, F.W., 2009b. Implications of noise and resolution on mechanical properties of trabecular bone estimated by image-based finite-element analysis, *Journal Orthopaedic Research*, 27 (10), 1263–1271.

Rho, J.Y., Ashman, R.B., and Turner, C.H., 1993. Young's modulus of trabecular and cortical bone material: ultrasonic and microtensile measurements, *Journal of Biomechanics*, 26 (2), 111–119.

Rho, J.Y., Kuhn-Spearing, L., and Zioupos, P., 1998. Mechanical properties and the hierarchical structure of bone, *Medical Engineering & Physics*, 20 (2), 92–102.

Rho, J.y., Tsui, T.Y., and Pharr, G.M., 1997. Elastic properties of human cortical and trabecular lamellar bone measured by nanoindentation, *Biomaterials*, 18 (20), 1325–1330.

Robinson, R.A. and Elliott, S.R., 1957. The water content of bone, *The Journal of Bone and Joint Surgery*, 39 (1), 167–188.

Ryan, S.D. and Williamson, J.L., 1989. Tensile testing of rodlike trabeculae from bovine femoral bone, *Journal of Biomechanics*, 22 (4), 351–355.

Saha, P.K., Gomberg, B.R., and Wehrli, F.W., 2000. Three-dimensional digital topological

characterization of cancellous bone architecture, *International Journal of Imaging Systems and Technology*, 11 (1), 81–90.

Sakata, S., Ashida, F., Kojima, T., and Zako, M., 2008. Three-dimensional stochastic analysis using a perturbation-based homogenization method for elastic properties of composite material considering microscopic uncertainty, *International Journal of Solids and Structures*, 45 (3/4), 894–907.

Sanchez-Palencia, E., 1980. *Non-homogenous media and vibration theory*, Lecture notes in physics ; 127, Berlin ; New York: Springer-Verlag.

Sansalone, V., Naili, S., Bousson, V., Bergot, C., Peyrin, F., Zarka, J., Laredo, J.D., and Haïat, G., 2010. Determination of the heterogeneous anisotropic elastic properties of human femoral bone: from nanoscopic to organ scale, *Journal of Biomechanics*, 43 (10), 1857–1863.

Sasaki, N., Matsushima, N., Ikawa, T., Yamamura, H., and Fukuda, A., 1989. Orientation of bone mineral and its role in the anisotropic mechanical properties of bone-transverse anisotropy, *Journal of Biomechanics*, 22 (2), 157–164.

Shi, X., Liu, X.S., Wang, X., Guo, X.E., and Niebur, G.L., 2010. Effects of trabecular type and orientation on microdamage susceptibility in trabecular bone, *Bone*, 46 (5), 1260–1266.

Shi, X., Wang, X., and Niebur, G.L., 2009. Effects of loading orientation on the morphology of the predicted yielded regions in trabecular bone, *Annals of Biomedical Engineering*, 37 (2), 354–362.

Siffert, R.S., Luo, G.M., Cowin, S.C., and Kaufman, J.J., 1996. Dynamic relationships

of trabecular bone density, architecture, and strength in a computational model of osteopenia, *Bone*, 18 (2), 197–206.

Stauber, M. and Müller, R., 2006. Volumetric spatial decomposition of trabecular bone into rods and plates-A new method for local bone morphometry, *Bone*, 38 (4), 475–484.

Syahrom, A., Abdul Kadir, M.R., Abdullah, J., and Ochsner, A., 2011. Mechanical and microarchitectural analyses of cancellous bone through experiment and computer simulation, *Medical and Biological Engineering and Computing*, 49 (12), 1393–1403.

Takano, N., Fukasawa, K., and Nishiyabu, K., 2010. Structural strength prediction for porous titanium based on micro-stress concentration by micro-CT image-based multiscale simulation, *International Journal of Mechanical Sciences*, 52 (2), 229–235.

Takano, N., Uetsuji, Y., and Asai, M., 2008. *Micro-mechanical simulation (in Japanese)*, Corona Publishing.

Takano, N., Zako, M., Kubo, F., and Kimura, K., 2003. Microstructure-based stress analysis and evaluation for porous ceramics by homogenization method with digital image-based modeling, *International Journal of Solids and Structures*, 40 (5), 1225–1242.

The American Society of Mechanical Engineers, 2006. ASME V&V 10-2006: Guide for Verification and Validation in Computational Solid Mechanics.

Thomsen, J.S., Ebbesen, E.N., and Mosekilde, L., 2002. Age-related differences between thinning of horizontal and vertical trabeculae in human lumbar bone as assessed by a new computerized method, *Bone*, 31 (1), 136–142.

Tsubota, K. and Adachi, T., 2004. Changes in the fabric and compliance tensors of cancellous bone due to trabecular surface remodeling, predicted by a digital image-based model, *Computer Methods in Biomechanics and Biomedical Engineering*, 7 (4), 187–192.

Turner, C.H., 1992. On Wolff law of trabecular architecture, *Journal of Biomechanics*, 25 (1), 1–9.

Turner, C.H., 1998. Three rules for bone adaptation to mechanical stimuli, *Bone*, 23 (5), 399–407.

Ulrich, D., van Rietbergen, B., Laib, A., and Rüegsegger, P., 1999. The ability of three-dimensional structural indices to reflect mechanical aspects of trabecular bone, *Bone*, 25 (1), 55–60.

Ulrich, D., van Rietbergen, B., Weinans, H., and Rüegsegger, P., 1998. Finite element analysis of trabecular bone structure: a comparison of image-based meshing techniques, *Journal of Biomechanics*, 31 (12), 1187–1192.

Ün, K., Bevill, G., and Keaveny, T.M., 2006. The effects of side-artifacts on the elastic modulus of trabecular bone, *Journal of Biomechanics*, 39 (11), 1955–1963.

van der Linden, J.C., Birkenhäger-Frenkel, D.H., Verhaar, J.A.N., and Weinans, H., 2001. Trabecular bone's mechanical properties are affected by its non-uniform mineral distribution, *Journal of Biomechanics*, 34 (12), 1573–1580.

van Rietbergen, B., Majumdar, S., Pistoia, W., Newitt, D.C., Kothari, M., Laib, A., and Rugsegger, P., 1998. Assessment of cancellous bone mechanical properties from

micro-FE models based on micro-CT, pQCT and MR images, *Technology and Health Care*, 6, 413–420.

van Rietbergen, B., Weinans, H., Huiskes, R., and Odgaard, A., 1995. A new method to determine trabecular bone elastic properties and loading using micromechanical finite-element models, *Journal of Biomechanics*, 28 (1), 69–81.

van Ruijven, L.J., Mulder, L., and van Eijden, T.M.G.J., 2007. Variations in mineralization affect the stress and strain distributions in cortical and trabecular bone, *Journal of Biomechanics*, 40 (6), 1211–1218.

Watts, N.B., 2002. Bone quality: getting closer to a definition, *Journal of Bone and Mineral Research*, 17 (7), 1148–1150.

Weinans, H., Huiskes, R., and Grootenboer, H.J., 1992. The behavior of adaptive bone-remodeling simulation models, *Journal of Biomechanics*, 25 (12), 1425–1441.

Wolfram, U., Wilke, H.J., and Zysset, P.K., 2010. Transverse isotropic elastic properties of vertebral trabecular bone matrix measured using microindentation under dry conditions (effects of age, gender, and vertebral level), *Journal of Mechanics in Medicine and Biology*, 10 (01), 139–150.

Yan, Y., Qi, W., Tianxia, Q., Teo, E.C., and Lei, W., 2012. The effect of threshold value on the architectural parameters and stiffness of human cancellous bone in micro CT analysis, *Journal of Mechanics in Medicine and Biology*, 12 (5), 1–16.